UNIVERSITA' DEGLI STUDI DI NAPOLI FEDERICO II

Dipartimento di Ingegneria Chimica, dei Materiali e

della Produzione Industriale

DOTTORATO DI RICERCA

IN INGEGNERIA DEI MATERIALI E DELLE STRUTTURE

XXVIII CICLO

Multipurpose Platform Based on $LiNbO_3$ Crystals for Novel Scenarios in Soft Matter Manipulation

COORDINATOR

Prof. Giuseppe Mensitieri

TUTORS

Prof. Giuseppe Mensitieri

Dr. Pietro Ferraro

CANDIDATE

Laura Mecozzi

March, 2016

Abstract

The many-sidedness of *Soft Matter* is the key factor that enables this materials class to generate a strong increasing attention in the international scientific research community, especially in investigating the broad range of available manipulation techniques. In particular, the introduction of multipurpose ferroelectric crystals as innovative handling driving forces represents the starting point for an alternative contact-free and nozzle-free technique for soft matter manipulation. This thesis work focuses on the development of highly efficient pyro-electrohydrodynamic (pyro-EHD) processes able to provide new reliable tools for the manipulation of biodegradable and/or biocompatible polymers to be employed in life science applications. The reliable control of the pyroelectric effect at microscale opens the doors to a wide variety of innovative techniques that include whipping-free electrospinning, versatile inkjet printing of polymer microlenses and even solar energy harvesting. Furthermore, the polar nature of lithium niobate crystals has been exploited here for developing innovative platforms able to control the morphology and the distribution of live cells through surfaces free from time-consuming chemical functionalization.

KEYWORDS: soft matter, electro-hydrodynamics, lithium niobate

Sommario

La cosiddetta “materia soffice” è caratterizzata da proprietà talmente molteplici da attirare l’attenzione crescente della comunità scientifica ormai da diversi decenni. In particolare, la possibilità di manipolare e dosare questa classe di materiali con tecniche che siano versatili ma anche dotate di elevata risoluzione spaziale, è di grande interesse per una vasta gamma di applicazioni. Questo lavoro di tesi si inserisce in questo contesto proponendo una piattaforma di tipo ferroelettrico in cui la polarizzazione spontanea di cristalli quali il niobato di litio ($LiNbO_3$) è sfruttata ad arte per generare forze di tipo elettro-dinamico su scala micrometrica. Tali forze sono in grado di dosare e indirizzare opportunamente piccoli volumi di materiale fluido di tipo polimerico ma anche di tipo biologico. In particolare, i campi elettrici generati tramite effetto piroelettrico integrato su cristallo sono utilizzati qui per diversi tipi di applicazioni. I risultati mostrano come fluidi polimerici possono essere elettro-filati in modo controllato, evitando le instabilità tipiche dell’electrospinning tradizionale. Polimeri con proprietà ottiche opportune possono essere usati per stampare matrici di microlenti plastiche e versatili. L’energia solare può essere accumulata e sfruttata per sorgenti alternative di campi elettrici. La morfologia e le proprietà di adesione di cellule di fibroblasti viventi possono essere pilotate tramite le cariche di superficie espresse da tali supporti. Gli esiti di questo lavoro di tesi possono aprire nuove frontiere nella manipolazione della materia soffice, espandendo così in prospettiva i settori di applicazione di questa classe di materiali.

PARLE CHIAVE: materia soffice, elettro-idrodinamica, niobato di litio

To my sweet Mati,

*« because it's tiresome for children to be always and forever
explaining things to the grown-ups »*

There are some things which cannot be learned quickly, and time,
which is all we have, must be paid heavily for their acquiring.
They are the very simplest things, and because it takes a man's life to
know them the little new that each man gets from life is very costly and
the only heritage he has to leave.

-Ernest Hemingway-

List of publications

Publications included in the thesis

I. L. Battista, **L. Mecozzi**, S. Coppola, V. Vespini, S. Grilli, P. Ferraro
"GRAPHENE AND CARBON BLACK NANO-COMPOSITE POLYMER ABSORBERS FOR A PYRO-ELECTRIC SOLAR ENERGY HARVESTING DEVICE BASED ON $LiNbO_3$ CRYSTALS"
Applied Energy 2014, DOI:*10.1016/j.apenergy.2014.09.035*

II S. Coppola**, L. Mecozzi**, V. Vespini, L. Battista, S. Grilli, G. Nenna, F. Loffredo, F. Villani, C. Minarini, P. Ferraro
"NANOCOMPOSITE POLYMER CARBON-BLACK COATING FOR TRIGGERING PYROELECTROHYDRODYNAMIC INKJET PRINTING"
Applied Physics Letters 06/2015; 106(26). DOI:*10.1063/1.4923469*

III. O. Gennari, V. Marchesano, **L. Mecozzi**, S. Grilli, P. Ferraro
"EFFECTS OF LITHIUM NIOBATE POLARIZATION ON CELL ADHESION AND MORPHOLOGY"
ACS Applied Materials & Interfaces 07/2015; 7:18113−18119, DOI:*10.1021/acsami.5b05340*

IV. R. Rega, O. Gennari, **L. Mecozzi**, S. Grilli, V. Pagliarulo, P. Ferraro
"BIPOLAR PATTERNING OF POLYMER MEMBRANES BY PYRO-ELECTRIFICATION"
Advanced materials 10/2015, DOI: *10.1002/adma.201503711*

V. **L. Mecozzi**, O. Gennari, R. Rega, S. Grilli, S. Bhowmick, M.A. Gioffrè, G. Coppola, P. Ferraro
"SPIRALS FORMATION AT MICROSCALE BY μ-PYROELECTROSPINNING"
Submitted Soft Matter ; January 2016

Publications not included in the thesis

A.1 **L. Mecozzi**, R. Stoico, S. Tassani, F. Particelli, F. Baruffaldi, M. Viceconti "BONE MINERAL DENSITY MEASUREMENTS ON CORTICAL AND TRABECULAR SPECIMENS: VALIDATION OF A DENSITOMETRIC CALIBRATION PROTOCOL FOR IN-VITRO MICRO-CT "
Bone . 01/2011; 48. DOI:*10.1016/j.bone.2011.03.414*

A.2 F. Particelli, **L. Mecozzi**, A. Beraudi, M. Montesi, F. Baruffaldi, M. Viceconti "A COMPARISON BETWEEN MICRO- CT AND HISTOLOGY FOR THE EVALUATION OF CORTICAL POROSITY: A PRELIMINARY STUDY ",
Bone .01/2011; 48. DOI:*10.1016/j.bone.2011.03.406*

A.3 F. Particelli, **L. Mecozzi**, A. Beraudi, M. Montesi, F. Baruffaldi, M.Viceconti "A COMPARISON BETWEEN MICRO-CT AND HISTOLOGY FOR THE EVALUATION OF CORTICAL BONE: EFFECT OF POLYMETHYLMETHACRYLATE EMBEDDING ON STRUCTURAL PARAMETERS"
Journal of Microscopy. 11/2011; 245(3):302-10. DOI*:10.1111/j.1365-2818.2011.03573.x*

A.4 C. Fersini, R. Stoico, S. Tassani, **L. Mecozzi**, S. Falcioni, F. Baruffaldi "VALIDATION OF A BONE MINERAL DENSITY CALIBRATION PROTOCOL FOR MICRO-COMPUTED TOMOGRAPHY"
J. Mechanics in Med & Bio (JMMB)", Jan 2016

A.5 V. Vespini, O. Gennari , S. Coppola , G. Nasti , **L. Mecozzi**, V. Pagliarulo, S. Grilli , C. Carfagna, P. Ferraro
"ELECTROHYDRODYNAMIC ASSEMBLY OF MULTISCALE PDMS MICROLENS ARRAYS"
Journal of Selected Topics in Quantum Electronics , November 2015

A.6 S. Coppola ; V. Vespini ; V. Bianco ; **L. Mecozzi** ; F. Olivieri, M. Todino, M. Paturzo, S. Grilli, P. Ferraro
" Pyro-EHD ink-jet printing for direct functionalization of 3D lab-on-chip devices ", *Proc. SPIE 9705, Microfluidics, BioMEMS, and Medical Microsystems XIV, 97050L , March 2016;* DOI:10.1117/12.2216682

List of figures

configuration (n, NFES; p, PES; m, m-PES). The distance h is in the range of centimetres, while hn, hp, hμ are in the range of millimetres.

3.2: (a) Schematic view of the m-PES set-up; (b,c) large view images of typical PMMA fibre spirals deposited onto a glass coverslip. Scale bars 20 μm. The inset shows a fibre cut by scalpel just after deposition, showing the rapid drying effect.

3.3: (a) Typical thermal camera images of the crystal during m-heating (the temperature increases from left to right); (b) corresponding temporal evolution of the crystal temperature for different operation powers in correspondence of the region evidenced by the red arrow in (a).

3.4: (Top) Optical microscope images of spiral fibres produced by μ-PES using PMMA solutions with different concentrations. The 2 % PMMA solution was obtained with an applied power of 320 mW at WD= 1.04 mm. The 9% PMMA solution with an applied power of 80 mW at WD= 0.11 mm. The 15 % PMMA solution was obtained with an applied power of 180 mW at WD= 0.08 mm (Scale bars 200 μm). These spirals correspond to the frames reported on the Bottom of the panel (extracted from the videos) for the three concentrations (scale bar 500 μm).

3.5: (a) Behaviour of the activation distance as a function of the μH power for different solution concentrations (the horizontal colour bar indicates the ranges corresponding to spiral formation); (b) minimum μH power values required for getting spirals for each concentration range (the values on the columns indicate the corresponding base-collector distance in mm); (c) spiralling distance values for each concentration at a fixed power of 300 mW; (d) rotation length and pattern diameter for each concentration at a fixed power of 350 mW. Mean values were evaluated over ten replicates of the experiments. The volume of the base drop was always fixed at 0.5 μL.

3.6: Optical microscope images of (a,b) thinner fibre spirals by the natural reduction of the volume of the base drop in the last steps of the process and (c,d,e) helical and straight fibres by translating the collector at different speeds: (c) 200 μm/s: (d)(e) 500 μm/s; (f) series of separated spirals from the same base drop, where the time flows from top to bottom. The clusters visible in (c) and (d) correspond to the sites where the stage was stopped. The few fibres laying on top correspond to the final stage of the spiralling that, in this case, was overdriven for getting the widest pattern.

bridge and experiences both normal and tangential components of the stress tensor while by introducing a CB coating (b) the pyro-effect is enhanced so that the polymer drop deforms into a sharp and elongated printing cone under the action of the tangential components.

4.8: (a) Single PMMA microlens and corresponding profile, (b) PDMS microlens (left) and liner array of multiple lenses (right). Tilted interferometric fringe image (c), wavefront error (d) and 3-D image of the PMMA microlenses (e)

4.9: Focal lengths of PDMS microlenses with different diameters

4.10: Schematic diagram of the process: the deposition by means of a carbon black membrane directly on the LN crystal, allows to contemporary deposit and fragment the polymer electro-spun fiber.

4.11: Contact angle values for PLGA onto different coatings

4.12: Extracted frames from the time lapse describing the temporal evolution from the original deposited PLGA fibre (on the left) to the one after the annealing process (on the right)(scale bar 100 mm).

4.13: Thermal breakup for different geometries varying the thickness of the fibre (a-c) and the morphology (d-f). (scale bar 200 µm)

4.14: (a)Behavior of the dots diameters obtained after the de-necking process as a function of the starting filament width. In (b) the de-necking wavelength as a function of the filament diameter is shown.

4.15: NIH 3T3 adhered on the biocompatible hydrophilic patterned polymer avoiding the PFPE layer. (scale bar 20 µm)

5.1: Typical bright field images of the cells seeded on *c*+ and *c*- free of functionalization and at the same time intervals (scale bar 100µm).

5.2: Typical fluorescence images of the cells seeded on (a) c-, (b) c+ and (c) glass, treated by the live/dead assay kit after 24h incubation.

5.3: Cell growth onto the three different substrates. Data are not statistically significant (*t*- test, $p > 0.1$).

5.4: Distribution of the number of live/dead cells over the three substrates (glass, c-, c+) after (a) 24h and (b) 48h incubation. The mean values were evaluated over three replicates of the experiment. Data are not statistically significant (t- test, $p > 0.1$).

5.5: Confocal microscope images of cells seeded on c+ and c- after 1 day of culture, with nuclei and actin stained by DAPI (blue) and TRITC (red)-conjugated phalloidin, respectively.

5.6: Confocal microscope image of confluent cells seeded on c+ after incubation for 24h, with nuclei and actin stained with DAPI and TRITC-conjugated phalloidin. (scale bar 20μm).

5.7: Distribution of the number of cells with more elongated shape and aligned stress fibres. Statistical significance was evaluated by Student's t-test, $p < 0.001$

5.8: Confocal microscope images of cells plated (a) on c- and (b) on c+ face after 24h plating, with nuclei, actin and vinculin stained with DAPI, TRITC-conjugated phalloidin and DyLight488 vinculin, respectively.

5.9: Typical optical microscope images of the scratch evolution over 6h for (a) c-, (b) c+ and (c) glass slide as control (scale bar 100μm)

5.10: Percentage of scratch healing for each substrate. The mean values were calculated over three replicates of the experiments. Statistical significance was evaluated by Student's t-test, $p < 0.01$.

5.11: Schematic view of the interaction between the polarized surface of LN and the environmental species that contribute to cell adhesion. Organic and inorganic ions, aminoacids, and proteins float around the crystal. Cations and positively charged ionic groups are actively adsorbed on the negatively charged surface (c-), thus contributing to the strong adhesion and spreading of the NIH-3T3 cells on this surface. Anions and negatively charged species are actively adsorbed on the positively charged surface (c+), thus reducing significantly the cell spreading. The scheme is not to scale.

6.1. Schematic view of the PE process steps (left column) and of the corresponding distributions of charges (right column).

6.2. (a,b) Camera side view of the liquid dispensing onto a flat or a curved PE membrane, respectively; (c) microscope images of typical dispensed droplets; (d) distribution of the activation distance values for PE membranes made of different polymer solutions. Scale bars 200 μm.

6.3 (a,b): Optical microscope images of two patterned PS membranes decorated by toner powder, where the hexagonal domains exhibit positive and negative polarity, respectively

6.4. Optical microscope images of SH-SY5Y cells after 24h incubation on (a,b) PS membrane pyro-electrified linearly at 400 μm period while incubating into the Petri dish and soon after removal, respectively (scale bars 100 μm and 2 mm, the inset shows a large view of the cell patterning); (c,d) cell patterning on PMMA and PS membranes pyro-electrified by an array of hexagons at 200 μm period, respectively (scale bars 100 μm). The dashed lines correspond to the boundaries between regions with opposite polarities.

A.1: Schematic diagram of the different regions of jet’s development in the ‘upward’ configuration and representation of the forces involved during the process.

List of tables

Contents

Chapter 1

Introduction

> *"Amusons-nous. Sur la terre et sur l'onde*
> *Malheureux, qui se fait un nom!*
> *Richesse, Honneurs, faux éclat de ce monde,*
> *Tout n'est que bulles de savon."*

The term *Soft Matter* arose for the first time in Seventies, in the Paris school of the physicist and Nobel laureate Pierre-Gilles de Gennes [1]. Originally introduced as a joke, it took hold and it is still the generally used term for describing all the attractive and considerably important materials that are neither simply solids or liquids. We can define soft matter (or soft condensed matter) the group of systems that includes liquids, colloids, polymers, foams, gels, granular materials, liquid crystals and a number of biological materials, merging the flexibility and elasticity of fluids with the stronger interactions of solids [1,2]. One of the most smart properties of soft matter is the diverse mechanisms of self-organization behind the formation of these states and their inherent dynamics. With the accurate combination of such different parameters, very complex soft matter structures with peculiar properties can arise all by themselves. Since soft matter length scales are often characterized by interactions that are of the order of thermal energies, relatively small perturbations can cause dramatic structural changes in them, so drastically changing the appearance and/or properties of the system on a macroscopic scale even at a modest deformation. This many-sidedness of *Soft Matter* is the key factor that enables this materials class to generate a strongly increasing attention in the international scientific research community, especially targeting to investigate the broad range of available manipulation techniques [3].

In fact, all these techniques, aimed to print or dispense inorganic, organic and biological inks (soft materials) at high resolution, represent one of the major point of interest in different research area including cell biology, tissue engineering and medical science.

Recently, an innovative platform that exploits the pyroelectric effect activated onto a ferroelectric crystal (e.g. $LiNbO_3$, $LiTaO_3$) for the manipulation of the soft matter, has been proposed [4]. These materials exhibit the highest values of spontaneous polarization available in nature and therefore are able to generate very intense electric fields by appropriate thermal gradients. The versatility of the pyroelectric approach for electrohydrodynamic-jet printing (e-jet) and the simplicity provided by the absence of nozzles, electrodes and high-voltage power supplies, collectively make the method very attractive for applications in printed electronics and related areas [5-7]. Nowadays, soldering iron and CO_2 laser heads have been used largely as thermal sources [4]. However, they present some drawbacks when specific applications are required. The temperature gradient is poorly controlled and the level of integrability of these sources is relatively low.

This thesis work is focused on the development of new strategies for reliable and highly efficient management of the polarization field of ferroelectric crystals, in order to overcome the above-mentioned limitations and, consequently, to extend the range of application fields.

Chapter 1 provides the introduction and the motivations that inspired this work. Chapter 2 gives an overview both of the state of art in soft matter manipulation methods and of the recent developments in the field. Furthermore, the main characteristics of the handled polymers and the key features of $LiNbO_3$ crystal, which are useful for the accurate understanding of the topics treated in the successive chapters, are reported. Chapter 3 describes how the introduction of an integrated micro-heater in the LN crystal (thermal stimulus at microscale), could help in controlling polymer manipulation by means of a “tamed” pyro-electrospinning that, due to regular ΔT intervals, is regulated by a stationary electric field. In Chapter 4 instead, the advantages in terms of efficiency, related to the introduction of a nanocomposite polymer membrane used as coating for the LN crystal, are presented. Furthermore, the enrollment of this configuration in different application areas is analyzed: starting from an alternative solar energy harvesting device to a new platform for triggering pyro-EHD inkjet printing and patterning. Chapter 5 demonstrates the biocompatibility of the LN crystal and its use as original platform for cells seeding and proliferation. Moreover, Chapter 6 describes a novel pyro-electrification (PE) technique able to generate free-standing polymer membranes with permanent bipolar patterns used inter alia, to guide cells adhesion. Finally, Chapter 7 provides a brief summary of this thesis.

In a framework in which the community is always looking for innovative and simplified methods able to manipulate the soft matter, this work of thesis offers unconventional options based on the use of the pyroelectric field produced by ferroelectric crystals. The wide variety of approaches proposed here, can open the route for the development of a revolutionary platform for simple and multi-purpose manipulation of the soft matter.

References

[1] P.G. de Gennes, “Soft matter: More than words” , *Soft Matter*, **1**, 16 (2005) DOI: 10.1039/b419223k

[2] D. Dervichian, “The Control of lyotropic liquid-crystals, biological and medical implications”, *Mol. Cryst. Liq. Cryst.*, **40**, 19-31 (1977)

[3] R. Borsali, R. Pecora (Eds.), Soft-Matter Characterization (2008)
ISBN: 978-1-4020-4464-9

[4] P. Ferraro, S. Coppola, S. Grilli, M. Paturzo, V. Vespini, “Dispensing nano-pico droplets and liquid patterning by pyroelectrodynamic shooting”, *Nature Nanotechnology*, **5**,429–435 (2010) , DOI:10.1038/nnano.2010.82

[5] S. Grilli, S. Coppola, V. Vespini, F. Merola, A. Finizio and P. Ferraro “3D lithography by rapid curing of the liquid instabilities at nanoscale”, *PNAS* **37**, 15106-15111 (2011)

[6] S. Coppola, V. Vespini, S. Grilli, P.Ferraro, “Self-assembling of multi-jets by pyro-electrohydrodynamic effect for high throughput liquid nanodrops transfer”, *Lab on a chip,* **19**, 3294-3298 (2011)

[7] F. Merola, M. Paturzo, S. Coppola, V. Vespini, P. Ferraro, “Self-patterning of a polydimethylsiloxane microlens array on functionalized substrates and characterization by digital holography”, *J. Micromech. Microeng.,* **19,**125006-125011, (2009)

Chapter 2

Basic concepts

2.1 Soft matter manipulation: state of art and recent developments

Progress in basic soft matter research is driven largely by the experimental techniques available for its manipulation. In particular, the increasing interest in soft matter printing technologies originates from the wide range of applications of the produced micro- and nano-patterns. The capability to deposit controlled volumes of inks by patterning polymers as well as biological molecules at different length scales has become a crucial tool in cell biology, tissue engineering and medical sciences encouraging the arising of such applications as targeted drug delivery to single cells or localized delivery of chemical reagents at nanoscale dimensions, giving to soft matter studies a wide overlap with nanotechnology [1]. A variety of printing-based manufacturing methods are currently used in order to overcome the limits related to the manipulation of such functional materials. We can distinguish between two different approaches: the *Top-Down* or *Template –assisted method* refers to the traditional workshop or microfabrication method where tools are used to cut, mill and shape materials into the desired shape and order, the *Bottom-Up* or *Template-free method* instead, refers to methods where devices 'create themselves' by self-assembly. Moreover, top-down procedures can be classified into two different groups: the techniques involving the contact of the stamp or the head with a substrate and the techniques that don't require a direct contact of the 'ink' material with the surface. As summarized in **Table 2.1** and described below, focusing on the most relevant methods, (see **Figure 2.1** for the schematic processes), each of the aforementioned technologies differs in resolution and printable materials.

Top-down and Bottom-up approaches are complementary in nanofabrication and comprise a numerous set of techniques. The use of a particular approach is often related to the specific need for a particular characteristic, shape, or composition of the nanomaterials for the different applications.

Often, methods are used in combination to complement each other. "Bottom-up" approach takes the idea of "Top-down" approach and flips it right over. In this case, instead of starting with large materials and chipping them away to reveal small bits of them, it all begins from atoms and molecules that get rearranged and assembled to larger nanostructures.

	PRINTING/PATTERNING METHODS	RESOLUTION	DISADVANTAGES
BOTTOM-UP	**BLOCK POLYMERS PATTERNING**	tens of nanometers	challenge in achieving large-area defect-free patterns and specific orientation of anisotropic structures
	ELECTROSPINNING	sub-microns	necessity of appropriate electrodes, use of high-voltage circuits, dispensed feature is limited to the nozzle diameter→clogging problems
TOP-DOWN	**PHOTOLITOGRAPHY**	from µm to sub-nm	not suitable for direct patterning of bioactive species with high sensitivity to uv irradiation and for the patterning of curved species. expensive. limited by optical diffraction.
	SOFT LITOGRAPHY - µCP	sub-µm	swelling of the stamp; hydrophobic and elastomeric nature of the stamp could distort the produced patterns
	NIL (UV-NIL / HEL)	< 5nm horizontal [3]	difficulties with high viscous polymers, materials susceptible to oxygen inhibition, prone to shrinkage, difficult to remove from molds
	DIP-PEN NANOLITOGRAPHY	sub -50- nm [1]	resolution of this technique can be affected by the grain size of the substrate, the choice of the ink and the tip-substrate contact time
	INKJET PRINTING (THERMAL / PIEZOELECTRIC/....)	50 µm	external electrods, presence of a nozzle that can induce clogging problems,..
	EHD – PRINTING	from µm to 50 nm	necessity of appropriate electrodes, use of high-voltage circuits, dispensed feature is limited to the nozzle diameter→clogging problems

Table 2.1: Characteristics of the principal printing methods. The upper box refers to bottom-up printing techniques, the lower one to the top-down. For the second group, contact (no contour) and non-contact (red contour) techniques, are highlighted. [2]

Some examples of such a synthesis route starting from atoms and molecules are methods like self-assembly of nanoparticles or block copolymers (BCPs- two polymer chains covalently linked together at one end) [4], chemical or electrochemical reactions for precipitation of nanostructures, sol–gel processing, laser pyrolysis, chemical vapor deposition (CVD), plasma or flame spraying synthesis, and atomic or molecular condensation. However, despite being so promising and inviting, our ability to build things from the bottom up is fairly limited in scope. While we can assemble relatively simple structures, we cannot produce complex, integrated devices using the bottom-up approach. Any kind of overall ordered arrangement aside from repeating regular patterns, cannot be done without some sort of top-down influence.

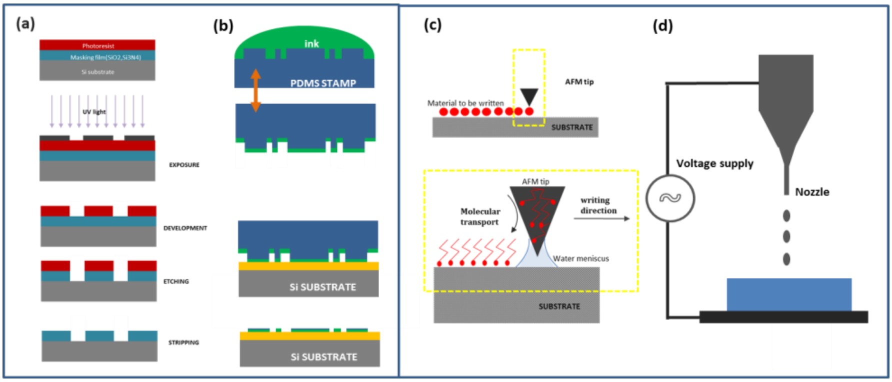

Figure 2.1: Example of the most used *Top-Down* manufacturing methods (a)photolithography, (b)μCP, (c)DPN, (d)EHD-jet printing

Photolithography (also termed optical lithography or UV lithography), has been over the last decades, one of the central methods for the patterning of soft matter/polymer for different applications [5-8]. It is the process of transferring geometric shapes on a rigid mask to the surface of a substrate. Patterns are generated by selectively exposing a monomer-, oligomer- or polymer-coated surface to photo-irradiation and by subsequently removing unexposed areas by a solution bath, such as an acid in wet methods or plasma-like oxygen ions in dry methods. Photolithography is a cost effective high-throughput technique suitable for large area surface patterning, but lacks in some features. It cannot be easily applied for the direct patterning of bioactive species, because of the absence of control over the chemistry of patterned surfaces, especially when complex organic functional groups of the sorts needed in chemistry, biochemistry, and biology are involved, and also doesn't work for nonplanar surfaces patterning. Moreover, the sizes of produced features are limited by optical diffraction and high resolution is achieved only at higher cost, so that other patterning methods are used as a valid alternative. First of all, **soft-lithography** can be viewed as a complementary extension of photolithography that unlike the latter, can process a wide range of elastomeric materials using soft stamps to obtain nanoscale patterns [9-10]. This technique to which we refer to as '*soft*', represents indeed a family of techniques for fabricating or replicating structures using "elastomeric stamps, molds, and conformable photomasks". Pioneering work in soft lithography was performed by G.M. Whitesides and co-workers [11-13], followed by many others [14-15], resulting in both application development and studies of the parameters involved in the process. Although this method provides low resolution compared with others, the stamps are inexpensive and can be used to easily fabricate large-scale submicron-sized patterns.

For this reason, different techniques are produced only changing the way that the molds are used: from replica molding (REM)[16] to micro-transfer molding (μTM)[17] up to micro-contact printing (μCP)[11,18].

In particular, in **micro-contact printing** the micrometer-scale patterned large surface area is obtained by transferring different types of compounds using a soft polymer stamp (PDMS). In μCP, only the ink from the raised surface of the PDMS stamp is transferred to the substrate[19]. Various inks, including small biomolecules, proteins or suspension of cells can be used. For more details on the μCP patterning we refer to different comprehensive reviews[18,20]. This technique, in spite of its merits, presents several drawbacks due mainly to the use of this soft polymer [21]. First of all the swelling of the stamp during the 'inking' as well as the contact time or the pressure applied on it, could generate an extreme variability could increase the size of the deposited pattern; moreover, the hydrophobic nature of PDMS combined with polar inks or again, the elastomeric nature of the stamp and its related deformation could result in distorted patterns[18][22].

To overcome the limitations of the original μCP technique, several alternatives have been developed either by changing the printing procedure itself or by varying the properties of the ink or the stamp. New ink materials have been introduced to control spreading and to enrich the variety of the applicable substrates and immobilized molecules[21].

Parallel to the appearance of these new strategies and methods, also new contact techniques arose. Only to cite one, **nanoimprint nanolithography (NIL)**, since its introduction in 1995, has been demonstrated in many researches as a simple, low-cost, and high-throughput process for replicating micro- and nanoscale patterns. In the NIL process, a prefabricated mould containing an inverse of the desired patterns is pressed onto a resist-coated substrate to replicate the patterns via mechanical deformation by either cooling the moulded material (thermal NIL or hot embossing lithography HEL) or by UV-photocuring the polymer precursor (UV-NIL). Due to its advantages, the nanoimprint lithography method has been rapidly developed over the years as a competitive alternative to conventional nanolithography processes [23]. The real challenges of NIL, despite its easily processability, are related to the difficulty in patterning highly viscous polymers (for thermal_NIL) [24,25], but also to the development of new photochemically sensitive materials that are not susceptible to oxygen inhibition, not prone to shrinkage (for UV-NIL) and are easily removed from moulds with high aspect ratio.

Switching to explore the non-contact patterning techniques, we can here consider the scanning probe microscopy-based methods and the ejecting ones.

Dip-pen nanolitography (DPN) belongs to the conventional scanning probe lithographic methods (such as nanografting and nanoshaving [26,27]) and was first demonstrated by Piner et al. [27]**.** DPN utilizes capillary forces to carry ink on a sharp tip to the substrate by using the AFM tip as a nib. When the 'ink'-coated AFM tip is translated above the surface, a liquid meniscus forms due to the relative humidity between the tip and the substrate, and the ink molecules diffuse as a result of chemical or physical adsorption of the ink to the surface. DPN has often been used to create on nano/submicroscale biological architectures[28], reaching a sub-50nm resolution. However, as reported in Piner et al.[27], the resolution of this technique can be affected by the grain size of the substrate, the choice of the ink and the tip-substrate contact time (the so called 'dwell time')[29].

Among the non-contact methods, the **ink-jet printing** represents one of the most popular material-conserving deposition technique used for liquid phase materials [30]. These materials, or inks, consist of a solute dissolved or otherwise dispersed in a solvent. The process essentially involves the ejection of a fixed quantity of ink in a chamber, from a nozzle through a sudden, quasi-adiabatic reduction of the chamber volume via piezoelectric action. A chamber filled with liquid is contracted in response to application of an external voltage. This sudden reduction sets up a shockwave in the liquid, which causes a liquid drop to eject from the nozzle [31]. Clearly, the necessity of external electrodes and the presence of a nozzle that implies a limitation in the use of viscous materials, make this technique very powerful, but restrictive at the same time leading to a resolution that is usually further degraded by the spreading of droplets as they impact at high speed to the target substrate [32]. Due to its operational features, acceptable for many uses, the adaptability of this technique for applications that require fine resolution is precluded [32].

The **EHD jet printing (e-jet)**[21,32] gives a solution to this limit taking advantage from the easiness to pull a fluid from a nozzle by means of applied electric fields, instead of pushing it, overcoming the capillary forces. Since G.I. Taylor [33] first studied in 1964 the behavior of liquids under electric fields, many researchers have tried to adapt the technique of controlling and manipulating the drop formation process by applying electric fields. In this way, the EHD-inkjet system has evolved as a prospective technology for micro/nano patterning, generating drops of very small size as compared to the other inkjet techniques. As shown in **Figure 2.1**, the e-jetting [34] involves a tube with a meniscus bearing a Taylor cone profile spraying a fine jet: the voltage between the nozzle and an opposing conducting support initiate the ink's flow from the nozzle via electro-hydrodynamics. On-demand droplets with sizes much smaller than that of the delivery nozzle (sometimes also the capillary nozzles are used for high resolution dispensing), have been obtained by pulsed EHD liquid jetting [35,36] or through the application of electrostatic fields [37], The potentialities of this new approach have been exploited in many areas of technology and manufacturing, e.g. electronics, optoelectronics or biotechnology, mainly since it is possible to manipulate fragile organic or biological materials.

Among the representative template-free patterning methods [38] also the **Electrospinning** technique has to be mentioned, as a tool to create surface textures in a simple and cost-effective manner. The electro-hydrodynamical phenomena called electrospinning launched polymer nanofibers into the broader realms of nanotechnology and materials science during the decades starting in 1990 and 2000 [39].

As detailed in Chapter 3, electrospinning is a process in which a charged polymer jet is collected on a grounded collector; a rapidly rotating collector results in aligned nanofibers while stationary collectors result in randomly oriented fiber mats. The polymer jet is formed when an applied electrostatic charge overcomes the surface tension of the solution. There is a minimum concentration for a given polymer, termed the critical entanglement concentration, below which a stable jet cannot be achieved and no nanofibers will form - although nanoparticles may be achieved (electrospray). The convenience of making fibers by electrospinning many kinds of polymers, on a laboratory bench, with inexpensive machinery makes nanofibers of many polymers available for a wide variety of possible applications [39].

Nevertheless these last methods require both the arrangement of appropriate electrodes and the use of high-voltage circuits between the liquid reservoir and the receiver substrate. Furthermore, also in these non-contact case, acting the nozzle as printing element, the dispensed feature is limited to the nozzle diameter and the clogging problem represents a further extremely restricting factor.

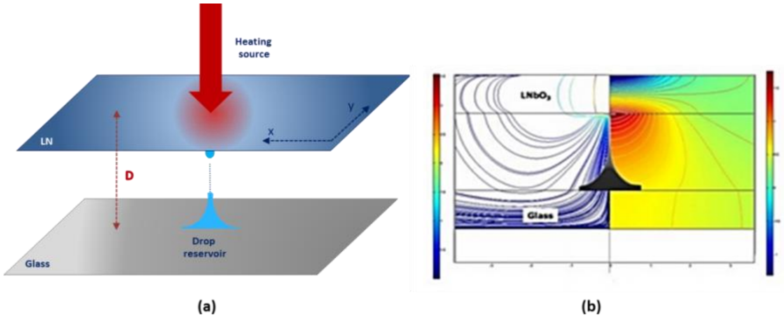

Figure 2.2: (a) Schematic diagram of the dispensing microfluidic system. A sessile drop is deposited onto the bottom substrate, a glass coverslip. **(b)** 3D-axis symmetric plot of the electric field lines(left) and electric potential (right) obtained by a finite element method simulation.

To overcome this lack of versatility, an alternative technique arose, in which attolitre liquid droplets from one drop or liquid film reservoirs were drawn via pyroelectric effect [40][41]. In this system, electrodes or nozzles are not required. The **pyro-EHD setup**, as shown in **Figure 2.2**, consists of two plates and a heat source, namely an infrared laser beam or a hot tip, in its original version. In the pyro-EHD process, when the thermal stimulus is applied to the surface of the ferroelectric crystal (LN), a redistribution of surface charges takes place allowing the reservoir drop to deform in a Taylor cone. When the so produced pyroelectric field exceeds a critical value, pulsating jets begin similarly to E-jet printing. Due to its skills, this method allows one to use many materials to be printed, breaking up parent drops that are standing on a surface into daughter droplets to be delivered directly to the desired substrate, open the way to attractive application fields.

In particular, modifying the setup in an adequately way, one can be able to handle materials otherwise not easily manageable without specific technical arrangements in a non-contact mode, as in the aforementioned case in which only lipophilic dielectric inks (commercial oils) were tested. In this work of thesis, we introduce in each of the following chapters, a modified pyro-EHD platform that, preserving its main characteristics, represents the starting point for a wide range of applications.

The key aspect of this technique must be found in the introduction of the new pyroelectric driving source, whose peculiar characteristics are described in the following paragraph. Starting from the description of the ferroelectric family, we will point out the structure and features of the Lithium Niobate crystal ($LiNbO_3$ or LN), the primary player in this new soft matter manipulation technique.

2.2 General properties of $LiNbO_3$: the new driving force

The response of a material to the application of an external electric field is strictly regulated by its electrical properties. In the presence of available free carriers (unbounded charges, either electrons or ions) the material will exhibit an electric current proportional to the applied voltage, hence performing as a *conductor*. Metals and electrolytes are examples of conductive materials. If the activation of charge transport necessitates a minimum energy to be provided to the system, the material is classified as a *semiconductor*. Silicon, germanium and alloys of the III-V groups of the periodic table belong of the semiconductor material family, and well known platforms for electronics. Finally, if no free carriers are available for conduction, the material is defined as a *dielectric*, or simply an *insulator*. Dielectrics represent a broad family of materials, which can be polarized by external electric fields. In general, such a property arises from their atomic structure, which upon the application of external electric fields shows spatially-separated complexes of charges of opposite sign, called dipoles. However, some dielectrics are made of polar molecules; hence already possess intrinsic electric dipoles. Dielectrics which possess dipoles are called **pyroelectrics** and show a polarization, called spontaneous polarization P_s**,** even in absence of external electric field.

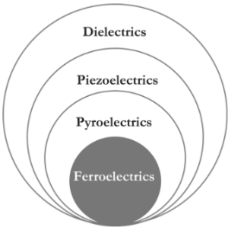

Figure 2.3 : Classification of ferroelectrics.

In particular, as shown in **Figure 2.3**, **ferroelectrics** represent a subgroup of pyroelectric materials in which such polarization can be reoriented by the application of external electric fields [42]. As a consequence of their intrinsic nature, we can define, for these ferroelectric crystals, the electric displacement vector D as a superimposition of different contributes:

$$D = \varepsilon_0 E + P_i + P_s$$

where ε_0 is the dielectric permittivity of vacuum, E the electric field, Pi the induced polarization and Ps the spontaneous polarization.

Among the others, the **lithium niobate** has gained a prominent role in research and applications of ferroelectric crystals and is one of the most used electro-optic (EO) materials. $LiNbO_3$ is characterized by large pyroelectric, piezoelectric (PZ), nonlinear and EO coefficients and has useful acoustic and acousto-optic properties. This richness of large-magnitude physical effects has caused LN to become widely used in applications such as acoustic wave transducers, optical amplitude modulators, second-harmonic generators, beam deflectors, dielectric waveguides, memory elements, holographic data processing devices, and others [43]. LN is a human-made dielectric material (Czochralski growth technique [44]) that doesn't exist in nature and it was first discovered to be ferroelectric in 1949 [45]. It is a rhombohedral crystal that consists of planar sheets of oxygen atoms in a distorted hexagonal close-packed configuration.[46].

Octahedral interstices are formed, one third of which is occupied by niobium (Nb) atoms, one third by lithium (Li) atoms, while the rest is vacant. **Figure 2.4** shows the schematic view of the Li and Nb atoms position respect to the oxygen planes. Above the Curie temperature Tc (around 1210°C) the phase is para-electric (no spontaneous polarization), while in the ferroelectric phase, below Tc, LN exhibits spontaneous polarization Ps along the c axis, resulting in a c+ and a c- face.

$LiNbO_3$	T_c (°C)	P_s(C/m^2)	E_c (kV/mm)	Refractive index	E_{pyro} (kV/mm)
	1210	0.71	21	$n_o = 2.29$ $n_e = 2.20$	10

Table 2.2: Values of the basic parameters related to the ferroelectric and optical properties of LN: Curie temperature, spontaneous polarization, coercive field [47-49], refractive index values(for ordinary and extraordinary polarized light)[50] of congruent LN, pyroelectric field at 100°C.

The c+ face corresponds to the positive end of the dipole and, vice versa, the c- face corresponds to the negative end of the dipole. In the para-electric phase the Li atoms lie in an oxygen layer that away from the Nb atom while the Nb atoms are centered between oxygen layers. Conversely, in the ferroelectric phase the elastic forces of the crystal become dominant and force the lithium and niobium ions into new positions.

The spontaneous polarization P_s changes according to $\Delta Pi = \xi i \cdot \Delta T$, where ξi is the pyroelectric coefficient and ΔT is the temperature variation. At equilibrium ($\Delta T = 0$) all Pi_s in the crystal are fully screened by the external screening charges and no electric field exists. The polarization change perturbs such equilibrium causing a lack or excess of surface change, thus generating a high electric field, the pyroelectric field.

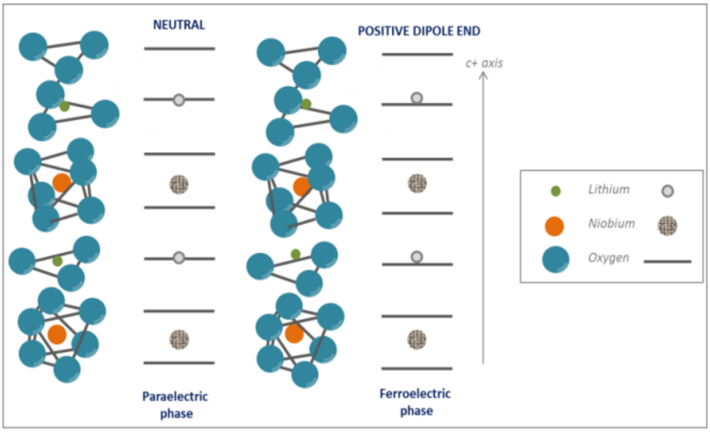

Figure 2.4: Schematic 3D structure of lithium niobate describing Li^+ and Nb^{5+} ion arrangement with respect to the O_2- planes (indicated by the solid lines). The paraelectric (ferroelectric) phase exhibits a zero (non-zero) net spontaneous polarization arising from the niobium and lithium ion displacement with respect to the oxygen planes.

2.2.1 Periodic Electric Field Poling

Lithium Niobate is an example of ferroelectric crystal which exhibits two possible orientations of the spontaneous polarization, +Ps and -Ps (forming an angle of 180° each other). The type of orientation is determined by the displacement of the Li^+ and Nb^{5+} ions along the z-axis with respect to the oxygen layers. As shown in **Figure 2.5**, the transition from an orientation to the other is obtained applying an electric field along the z axis, antiparallel to the polarization and exceeding the coercive value E_c (minimum value necessary to displace the ions).
Practically, starting from a single domain crystal, in order to obtain a periodic square array of hexagonal reversed domains, the spontaneous polarization of LN is periodically inverted by photolithography and electric field poling [51].
The periodically poled LN (PPLN) is achieved at room temperature by an electric field poling process[52].

A positive voltage pulse, slightly exceeding the coercive field of LN (~21kV/mm), is applied on the z+ patterned crystal face by using a liquid electrolyte consisting of LiCl in deionized water. The liquid electrode configuration has two electrolyte containing chambers which squeeze the sample between two O-ring gaskets, as shown schematically in **Figure 2.6(a)**.

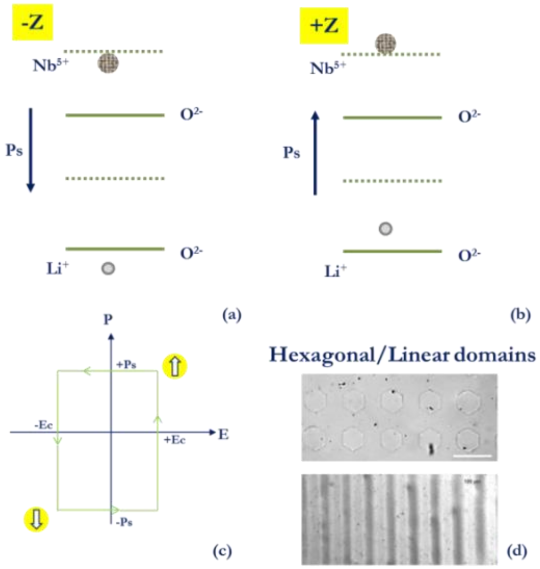

Figure 2.5: Orientations of the spontaneous polarization Ps due to the displacement of the ions along the Z axis in LN. Ions disposition with respect to the oxygen planes for (a) -Z and (b) +Z. Poling the crystal allows switching from one configuration to another through a series of poling events following a P-E hysteresis loop (c). To obtain a periodic hexagonal or linear pattern (d) a specific lithographic mask is used.(The period of the structure was around 200 µm along both x and y crystal axis direction for the hexagonal and linear domains)

Figure 2.6(b) illustrates the external electrical circuit. A conventional Signal Generator (SG) drives an High Voltage Amplifier (HVA - 2000x), provided by Trek, Inc., with a series current limiting resistor, $R_S = 50M\Omega$, in order to get a 12kV positive voltage. A diode rectifier *D* is connected to the output of the *HVA* to prevent flowing of back-switch current in the circuit.

It is well known [53] that, in LN, the reversed domains typically grow beyond the width of the electrodes as the result of the remaining fringing fields along the edges of the lithographic grating strips. The strategy for optimal domain patterning, with conventional electric field poling, is to stop the voltage pulse before poling progresses under the photoresist layer. An in situ method which can be used as a stopping criterion consists in watching for a drop in the poling current I_{pol} and a corresponding rise in the poling voltage V_{pol}, both effects indicating that the sample has completely poled under the electrodes and the domains are now laterally spreading under the insulating layer [53,54]. In fact, the conductivity of LN at room temperature is low enough that the poling current can be monitored readily by measuring the voltage drop across the resistance $R_m = 10k\Omega$ while a conventional

High Voltage Probe (*HVP*) is used to measure the poling voltage V_{pol} across the sample. Both current and voltage waveforms are visualized on the oscilloscope *Osc* during the poling process.

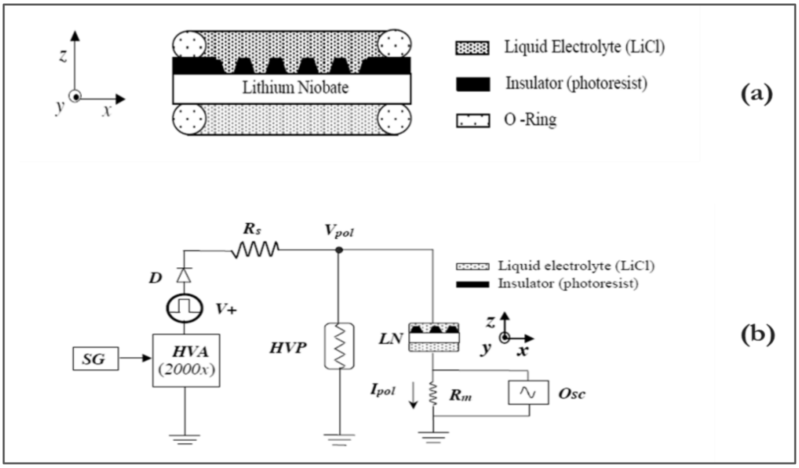

Figure 2.6: (a)Cross-sectional view of the electrode configuration for electric field poling. The photoresist grating acts as an insulating barrier that lowers the electric field applied through the liquid electrolyte below the coercive field needed to reverse the spontaneous polarization. (b) Electrical circuit used to pole LN samples. An High Voltage Amplifier (HVA - 2000x) with a series resistor RS = 50MΩ produces +12kV voltage by using a conventional Signal Generator (SG). A diode rectifier D was connected to the output of the HVA to prevent flowing of backswitch current.

For the experiments described in the following chapters, when PPLN was used, both sides polished and 500 μm thick LN crystals (from Crystal Technology, Inc.) were subject to standard electric field poling [52] in order to achieve a square array of hexagonal reversed domains. The samples were first resist patterned (photoresist Shipley S1813-J2, around 1.3 μm thick) by conventional mask lithography in order to achieve a square array of circular or linear (in case of linear patterns) resist openings. The subsequent application of high voltage pulses, exceeding the coercive field of the material, allowed to fabricate the periodic domain reversed sample.

2.3 Principal characteristics of the polymers handled in this thesis

In this section, the synthetic polymers used in this work of thesis are briefly described. **Table 2.3** reports their classification in term of printable-resolution and their principal characteristics [38]. Exception made for PDMS (a thermo-curable polymer), the other polymers described are thermoplastics. A thermoplastic polymer becomes liquefied or molten above the melting temperature (T_m). The material also becomes plastic above the glass transition temperature (T_g), allowing for further modification such as drawing, bending and molding at elevated temperature [55]. Since these materials are solids at room temperature, heat or solvent treatment can be used to make fine structures.

CATEGORY	MATERIAL	ELASTIC MODULUS	T_g (°C)	T_m (°C)
THERMO-CURABLE	PDMS	0.6 – 3.5 MPa	-125	-40
THERMOPLASTIC	PMMA	2 – 3.5 GPa	114	160
	PS	3 – 3.5 GPa	100	240
THERMOPLASTIC (BIODEGRADABLE)	PLGA	2 GPa	40-60	n/a

Table 2.3. Summary of material properties for various polymeric biomaterials.

2.3.1 Polydimethylsiloxane (PDMS)

Polydimethylsiloxane (PDMS), a thermo-curable polymer, belongs to a group of polymeric organosilicon compounds that are commonly referred to as silicones.

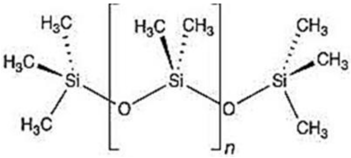

Specifically, PDMS is a silicone elastomer.

PDMS was first introduced by Whitesides's group in the early 1990s in the form of soft lithography in order to massively produce micro- and submicron-scale structures. Microstructures of PDMS are made by mixing the pre-polymer and cross-linker with an appropriate ratio (usually 10:1) following by backfilling into a pre-patterned master and curing at 60-70°C in an oven for an hour or two. The polymer is manufactured in multiple viscosities, ranging from a thin pourable liquid (when n is very low), to a thick rubbery semi-solid (when n is very high).

Several properties of PDMS are instrumental in the formation of high-quality patterns and structures in soft lithography:

- PDMS is an elastomer and conforms to the surface of the substrate over a relatively large area.
- PDMS is deformable enough such that conformable contact can even be achieved on surfaces that are non-planar on a micrometer scale.
- Elastic characteristics of PDMS allows it to be released easily from complex and fragile structures.
- PDMS provides a surface that is low in interfacial free energy (21.6 x 10 -3 Jm-2) and chemically inert.
- PDMS is homogeneous, isotropic and optically transparent down to 300 nm.
- PDMS is durable and the stamps can be used up to about 100 times over a period of several months without noticeable degradation.
- Surface properties of PDMS can be modified by plasma treatment followed by the formation of SAMs (self-assembled monolayers) to give appropriate interfacial interactions with materials that themselves have a wide range of interfacial free energies.
- The low elastic modulus for Sylgard 184 PDMS makes it difficult to replicate nanoscale features with high aspect ratios using soft lithography.

2.3.2 Poly (methyl methacrylate) (PMMA)

Poly(methyl methacrylate) is a linear thermoplastic polymer . It is produced by free-radical polymerization of methyl-methacrylate in mass (when it is in sheet form) or suspension polymerization according to the following chart:

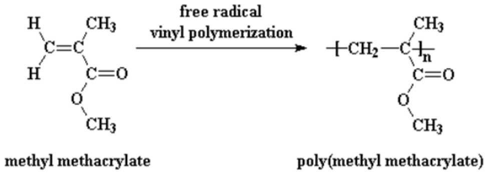

PMMA is among the polymers that have high resistance to sunshine exposure, because it has a small variation under the effect of UV-radiation. It has very good thermal stability, and is known to withstand temperatures as high as 100°C and as low as 70°C. It also possesses very good optical properties, with a refractive index of 1.490, and a good degree of compatibility with human tissue. In the field of mechanical strength, PMMA has a high Young’s Modulus and a low elongation at breakage. Therefore, it does not shatter upon rupture, and happens to be one of the hardest thermoplastics with high scratch resistance. This polymer has a reasonable resistance to chemicals, being unaffected by the aqueous solution of most laboratory chemicals. However, it has a low resistance to chlorinated and aromatic hydrocarbons, esters, or ketones. Polymer tacticity is the relative stereochemistry of adjacent chiral centers within a polymer, especially vinyl polymers. The physical properties of a polymer, such as glass transition temperature (T_g), solubility, crystallinity, and hydrolysis, depend not only on the type of monomer comprising it, but also on the secondary and tertiary structures, that is, the stereochemistry of the linkage. Based on this fundamental chemistry, PMMA could be isotactic, syndiotactic, or atactic. Isotactic is when the adjacent monomer groups were added in the meso diad mode, and the ester groups on the successive asymmetric carbons are projected on the same side of the polymer chain. Syndiotactic is when the monomer groups were added in the racemic diad mode, and the ester groups on the successive asymmetric carbons are projected in a regular alternation on both sides of the plane in the polymer chain. Atactic is another racemic diad mode, but the ester groups on the successive asymmetric carbons are projected randomly on both sides of the plane in the polymer chain.

2.3.4 Polystyrene (PS)

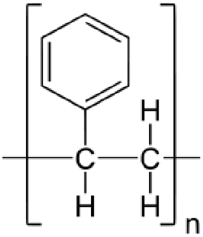

Polystyrene (PS) is a synthetic aromatic polymer made from the monomer styrene. Polystyrene can be solid or foamed. General-purpose polystyrene is clear, hard, and rather brittle. It is an inexpensive resin per unit weight. It is a rather poor barrier to oxygen and water vapor and has a relatively low melting point. As a thermoplastic polymer, polystyrene is in a solid (glassy) state at room temperature but flows if heated above about 100 °C, its glass transition temperature. It becomes rigid again when cooled. In chemical terms, polystyrene is a long chain hydrocarbon wherein alternating carbon centers are attached to phenyl groups (the name given to the aromatic ring benzene). Polystyrene's chemical formula is $(C_8H_8)_n$; it contains the chemical elements carbon and hydrogen. The material's properties are determined by short-range van der Waals attractions between polymers chains. Since the molecules are long hydrocarbon chains that consist of thousands of atoms, the total attractive force between the molecules is large. When heated (or deformed at a rapid rate, due to a combination of viscoelastic and thermal insulation properties), the chains are able to take on a higher degree of conformation and slide past each other. This intermolecular weakness (versus the high intramolecular strength due to the hydrocarbon backbone) confers flexibility and elasticity. The ability of the system to be readily deformed above its glass transition temperature allows polystyrene (and thermoplastic polymers in general) to be readily softened and molded upon heating.

2.3.3 Poly(lactic-co-glycolic acid) (PLGA)

Poly(lactic-co-glycolic) acid (PLGA) has attracted considerable interest as a base material for biomedical applications due to its:

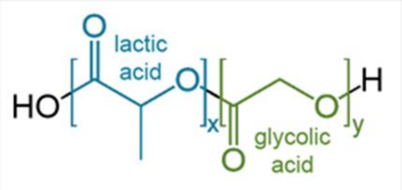

- biocompatibility;

- tailored biodegradation rate (depending on the molecular weight and copolymer ratio);
- approval for clinical use in humans by the U.S. Food and Drug Administration (FDA);
- potential to modify surface properties to provide better interaction with biological materials;
- suitability for export to countries and cultures where implantation of animal-derived products is unpopular.

PLGA is a linear copolymer that can be prepared at different ratios between its constituent monomers, lactic (LA) and glycolic acid (GA). Depending on the ratio of lactide to glycolide used for the polymerization, different forms of PLGA can be obtained: these are usually identified in regard to the monomers' ratio used (i.e., PLGA 75:25 identifies a copolymer consisted of 75% lactic acid and 25% glycolic acid). Different synthesis mechanisms are used to obtain PLGA and the process parameters influence strongly the physical-chemical characteristics of the end product.

References

[1] C.D. O'Connell, M.J. Higgings, D. Marusic, S.E. Moulton, G.G. Wallace, "Liquid ink deposition from atomic force microscope tip: deposition monitoring and control of feature size", *Langmuir* , **30,** 2712-2721, (2014)

[2] Y.Xia, G.M. Whitesides, "Soft lithography", *Annu. Rev. Mater. Sci.*, **28**:153–84, (1998)

[3] Z. Nie, E. Kumacheva, "Patterning surfaces with functional polymers", *Nature Materials*, **7,** 277-290, (2008)

[4] C. J. Hawker, T.P. Russell, "Block Copolymer Lithography: Merging "Bottom-Up" with "Top-Down" Processes", *MRS Bulletin,* **30,** 952-966**,** (2005)

[5] M. Park, C. Harrison, P.M. Chaikin, R.A. Register, D.H. Adamson, "Block copolymer lithography: Periodic arrays of ~ 10^{11}holes in 1 square centimeter", *Science,* **276**, 1401-1404, (1997)

[6] H.K. Wu, T.W. Odom, G.M. Whitesides, "Reduction photolithography using microlens arrays: Applications in gray scale photolithography. *Anal. Chem.*, **74**, 3267-3273, (2002)

[7] W.G. Koh, A. Revzin, M.V. Pishko, "Poly(ethylene glycol) hydrogel microstructures encapsulating living cells", *Langmuir*, **18**, 2459-2462, (2002)

[8] J. Hoffmann, M. Plotner, D. Kuckling, W.J. Fischer, "Photopatterning of thermally sensitive hydrogels useful for microactuators", *Sens. Actuat.A*, **77**, 139-144, (1999)

[9] Y. Xia, G.M. Whiteside," Soft lithography" *Angew. Chem. Int. Ed.*, **37**, 550-575,(1998)

[10] D. Qin, Y. Xia, G.M. Whitesides, "Soft lithography for micro- and nanoscale patterning", *Nature Protocols*, **5**, 491-502, (2010) doi:10.1038/nprot.2009.234

[11] A. Kumar, G.M. Whitesides, "Features of gold having micrometer to centimeter dimensions can be formed through a combination of stamping with an elastomeric stamp and a alkanethiol ink followed by chemical etching", *Appl.Phys.Lett.*, **63,** 2002-2004, (1993)

[12] A. Kumar, H.A. Biebuyck, G.M. Whitesides, “Patterning Self-Assembled Monolayers: Applications in Materials Science”, *Langmuir*, **10**, 1498-1511, (1994), DOI:10.1021/la00017a030

[13] L. Yan, X.M. Zhao, G.M. Whitesides, “Patterning a Preformed, Reactive SAM Using Microcontact Printing”, *J.Am.Chem.Soc.*, **120**, 6179-6180, (1998)

[14] N.L. Jeon, P.G. Clem, D.A. Payne, R.G. Nuzzo, “A Monolayer-Based Lift-Off Process for Patterning Chemical Vapor Deposition Copper Thin Films”, *Langmuir*, **12**, 5350-5355, (1996)

[15] L.G. Zhang, J.F. Liu, Z.H. Lu, “Microfabrication on polymer with a contact procedure”, *Supramol. Sci.*, **5**, 713-715, (1998)

[16] Y.N. Xia, G.M. Whitesides, “Extending Microcontact Printing as a Microlithographic Technique”, *Langmuir*, **13**, 2059-2067, (1997)

[17] X.M. Zhao, Y. Xia, G.M. Whitesides, “Fabrication of three-dimensional micro-structures: Microtransfer molding”, *Adv. Mater.*, **8**, 837-840, (1996)

[18] A.P. Quist, E. Pavlovic, S. Oscarsson, “Recent advances in microcontact printing”, *Anal.Bioanal.Chem.*, **381**, 591-600, (2005)

[19] S.A. Ruizab, C.S. Chen, “Microcontact printing: A tool to pattern”, *Soft Matter*, **3**, 1–11 (2007)

[20] B.D. Gates et al., “New approaches to nanofabrication: Molding, printing, and other techniques.”, , *Chem.Rev.,* **105**, 1171-1196, (2005)

[21] A. Perl, D.N. Reinhoudt, J. Huskens, “Microcontact printing: limitations and achievements”, **21**, 2257–2268, (2009)

[22] J.A. Rogers, K.E. Paul, G.M. Whitesides, “Quantifying distortions in soft lithography”, *J. Vac. Sci. Technol. B*, **16**, 88-97

[23] N. Kooy, K. Mohamed, L.T. Pin, O.S. Guan, “A review of roll-to-roll nanoimprint lithography”, *Nanoscale Research Letters*, **9**, 320-333, (2014)

[24] M. Colburn, S. Johnson, M. Stewart, S. Damle, T. Bayle, B. Choi, M. Wedlake, T. Michaelson, S.V. Sreenivasan, J. Ekerdt, C.G. Willson, “Step and flash

imprint lithography: a new approach to high resolution patterning", *Proc SPIE Int SocOpt Eng*, **3676**, 379-389, (1999)

[25] S. Gilles, M.Meier, M. Prompers, A.V.D. Hart, C. Kugeler, A. Offenhausser, D. Mayer, "UV nanoimprint lithography with rigid polymer molds", *Microelectron Eng,* **86**, 661-664, (2009)

[26] R. M. Nyffenegger, R.M. Penner, " Nanometer-scale surface modification using the scanning probe microscope: Progress since 1991", *Chem. Rev.*, **97**, 1195–1230 (1997).

[27]. R.D. Piner, J. Zhu,F. Xu, S.H. Hong, C.A. Mirkin, "Dip-pen nanolithography", *Science*, **283**, 661–663 (1999).

[28] D.G.Thompson, E.O. McKenna , A. Pitt, D. Graham, "Microscale mesoarrays created by dip-pen nanolithography for screening of protein-protein interactions", *Biosens. Bioelectron*. **26** 4667–73 (2011)

[29] D.J. Eichelsdoerfer, K.A. Brown, C.A.Mirkin, "Capillary bridge rupture in dip-pen nanolithography", *Soft Matter*, **10**, 5603-5608, (2014)

[30] E.A Roth, T Xu, M Das, C Gregory, J.J Hickman, T Boland,"Inkjet printing for high-throughput cell patterning", *Biomaterials,* **25**, 3707–3715, (2004)

[31] M.Singh, H.M. Haverinen, P.Dhagat, G.E. Jabbour, "Inkjet Printing—Process and Its Applications", *Adv. Mater.*, **22**, 673-685, (2010)

[32] M.S. Onses, E. Sutanto, P.M. Ferreira, A.G. Alleyne, J.A. Rogers, "Mechanism, capabilities, and applications of high-resolution electrohydrodynamic jet printing", *Small*, **11**, 4237-4266, (2015)

[33] G. I. Taylor, "Disintegration of Water Drops in an Electric Field", *Proc. R. Soc. Lond. A*, **280**, 383–397 (1964).

[34] L.T. Cherney, "Structure of Taylor cone-jets: limit of low flow rates", *J. Fluid Mech.*, **378**, 167–196 (1999)

[35] C.H Chen, , D.A. Saville, I.A. Aksay, "Scaling laws for pulsed electrohydrodynamic drop formation", *Appl. Phys. Lett*. **89**, 124103 (2006).

[36] A.U. Chen, O.A. Basaran, “A new method for significantly reducing drop radius without reducing nozzle radius in drop-on-demand drop production”, *Phys. Fluids*, **14**, L1–L4 (2002).

[37] L. Miccio, M. Paturzo, S. Grilli, V. Vespini, P.Ferraro, “Hemicylindrical and toroidal liquid microlens formed by pyro-electro-wetting“, *Opt. Lett.*, **34**,1075–1077 (2009).

[38] H.N. Kim, D.-H. Kang, M.S. Kim, A. Jiao, D.-H. Kim, K.-Y. Suh, “Patterning Methods for Polymers in Cell and Tissue Engineering”, *Annals of Biomedical Engineering*, **40**, 1339–1355(2012) DOI: 10.1007/s10439-012-0510-y

[39] D.H. Reneker, A.L. Yarin, “Electrospinning jets and polymer nanofibers”, *Polymer*, **49**, 2387–2425, (2008)

[40] P. Ferraro, S. Coppola, S. Grilli, M. Paturzo, V. Vespini,“Dispensing nano–pico droplets and liquid patterning by pyroelectrodynamic shooting”, *Nature Nanotechnology*, **5**, 429–435 (2010) , DOI:10.1038/nnano.2010.82

[41] C. Ru, J. Luo, S. Xie, Y. Sun, “A review of non-contact micro- and nano-printing technologies”, *J.Micromech.Microeng.*, **24**, (2014)

[42] Lines M. E. and G.A. M., “Principles and Applications of Ferroelectrics and Related Materials “ 1977: Oxford

[43] A. Yariv , “Quantum electronics”, John Wiley&Sons (1989)

[44] J. Czochralski, “Ein neues verfahren zur messung der kristallisationsgeschwindigheit der metalle.”, *Phys. Chem.*, **92**, 219–221, (1918)

[45] B.T. Matthias, J.P. Remeika , “Ferroelectricity in the Ilmenite Structure.”, *Physical Review*, **76**, 1886-1887, (1949)

[46] R.S. Weis, T.K. Gaylord,” Lithium niobate: Summary of physical properties and crystal structure”, *Appl. Phys. A* , **37**, 191 (1985).

[47] K. Nassau, H.J. Levinstein, G.M. Loiacono,” Ferroelectric lithium niobate. 1. Growth, domain structure, dislocations and etching”, *J. Phys. Chem. Solids* , **27**, 989 (1966).

[48] I. Camlibel,”Spontaneous polarization measurement in several ferroelectric oxides using a pulsed field method”, *J. Appl. Phys.*, **40**, 1690 (1969).

[49] H. Karlsson, PhD thesis, Department of Laser Physics and Quantum Optics, The Royal Institute of Technology, Stockholm

[50] D.S. Smith, H.D. Riccius, R.P. Edwin, *Opt. Comm*. **17**, 332 (1976).

[51] R.L. Byer, *IEEE J. Select. Topics Quantum Electron*., **6**, 911 (2000).

[52] S. Grilli, M. Paturzo, L. Miccio and P. Ferraro, *Meas. Science and Tech*. **19**, 074008 (2008).

[53] M. Yamada, N. Nada, M. Saitoh, and K. Watanabe, *Appl. Phys. Lett*. **62**, 435-436 (1993).

[54] L.E. Myers, R.C. Eckardt, M.M. Fejer, R.L. Byer, W.R. Bosenberg, J.W. Pierce, *J. Opt. Soc. Am. B* , **12**, 2102-2116 (1995)

[55] M.P. Stevens,” Polymer Chemistry: An Introduction.” New York: Oxford University Press, 1999

Chapter 3

Micro-Pyro-Electrospinning (μ-PES) for whipping-free spinning of polymer fibres

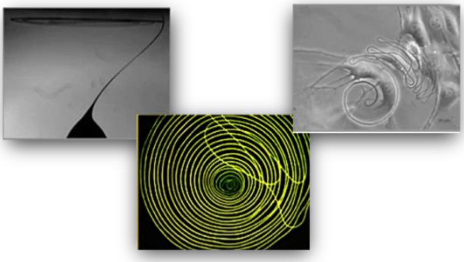

The characterization reported in the following chapter, refers to an innovative approach belonging to the electro-spinning (ES) family driven by a microscale integrated thermal stimulus, that is mask-free and single step. The pyro-electrohydrodynamic process activated in this way can be used to manipulate soft matter and is able to generate true spiral patterns at microscale by a direct process.

Spiral patterns are found extensively in nature as well as in art. Even some technological devices are inspired to and take advantage of this kind of shape. The assembly of microarrays with spiral channels have been proposed as successful solutions for multi-sample analyses and for high hybridization rates [1]. Spiral moulds have been used for characterizing the rheological behavior of polymers injected over fabrics [2]. Very recently, microscale soft-robots have been developed with spiral bending capabilities [3], spiral-like electrodes have been proposed for energy harvesting applications [4], and three-dimensional spirals have been suggested for developing new ways of manipulating the polarization state of the THz electromagnetic waves [5]. The growing awareness of fundamental rules underlying the apparent universal repetition of spirals in nature has led researchers to try to identify and evaluate these patterns through precise scientific models [6,7]. However, poor attention has been devoted to the establishment of techniques able to replicate the formation of such fascinating shapes by direct printing. Li et al. proposed specific micro-manipulation techniques able to deform the surface of Ag-core/SiO2-shell microstructures into spiral arrangements [8,9]. However, those structures consist actually of triangular patterns that self-organize according to Fibonacci-based spirals. Other works propose the well-known electro-spinning (ES) method for generating coils of polymer fibres that, however, are arranged according to helical geometries instead of real spirals [10-12]. Conversely, Godinho et al. proposed alternative configurations of ES for generating cellulose-based fibres arranged into both helices and spirals [13,14]. Those structures mimic the shapes of plant tendrils but lack the regularity of ordered spirals at microscale. Recently, Chang et al. described an easy way to form micro spiral fibres by a modified ES process, but those structures still exhibit the spiral shape as a bundle, lacking regularity at microscale [15,16].

In this chapter we present **the μ-pyro-electrospinning (μ-PES)**, an innovative approach where polymer fibres are electrospun by pyroelectric fields controlled at microscale and assemble directly into spiral patterns with true regularity at microscale. A mask-free and single step process allows one to fabricate spiral templates for different applications, including cell patterning.

3.1 The μ-PES "backbone"

The experimental results show how the fibre spiralling is obtained by controlling appropriately polymer properties and electro-hydrodynamic (EHD) forces [17-22].

It is well-known that fibres spun by **ES** [23-27] undergo random whipping and bending, that researchers use for fabricating polymer mats for a wide variety of applications including protective clothing [23,28-30], filtration [31], biotechnology [32,33], photonics [34], just to cite some. Others try to control these bending regimes by different techniques. For example, modified configurations, such as near-field ES (**NFES**), where reservoir and collectors are designed appropriately, have been presented in literature for avoiding the bending zone and for depositing straight ordered fibres onto the collector [35-38]. Here, instead, we found out the operation conditions able to stabilize the bending effects, leading to spiralling. Recently, the same authors have shown the advantages of pyro-electrospinning (**PES**) for depositing well-aligned fibres from poly(lactic-co-glycolic acid) (PLGA) solutions [39]. Analogously to NFES, we demonstrated there how the surface pyroelectric charges are able to draw fine fibres from sessile drops of PLGA that the translating collector drags gently, obtaining precise linear patterns.

Figure 3.1 shows the schematic views of the main ES techniques available in literature, compared with the μ-PES proposed in this work for generating true spirals at microscale. Every scheme is coupled to microscope images of the typical fibre patterns produced by each technique. Concerning the ES fibre formation we refer the readers to valuable papers and reviews on the subject [23,45-48] (see **Appendix A**). Here we focus our attention on the possibility of using the well-known ES phenomenon for generating true spirals for the first time. The traditional ES uses nozzles, external voltages around 20 kV and working distances *h*, between the nozzle and the collector, relatively large (around 15 cm). The thickness of the fibre depends significantly on the nozzle diameter that, however, cannot be reduced due to clogging limitations. Therefore the traditional ES needs large *h* for thinning and drying the fibre before reaching the collector and consequently has to operate at large voltages.

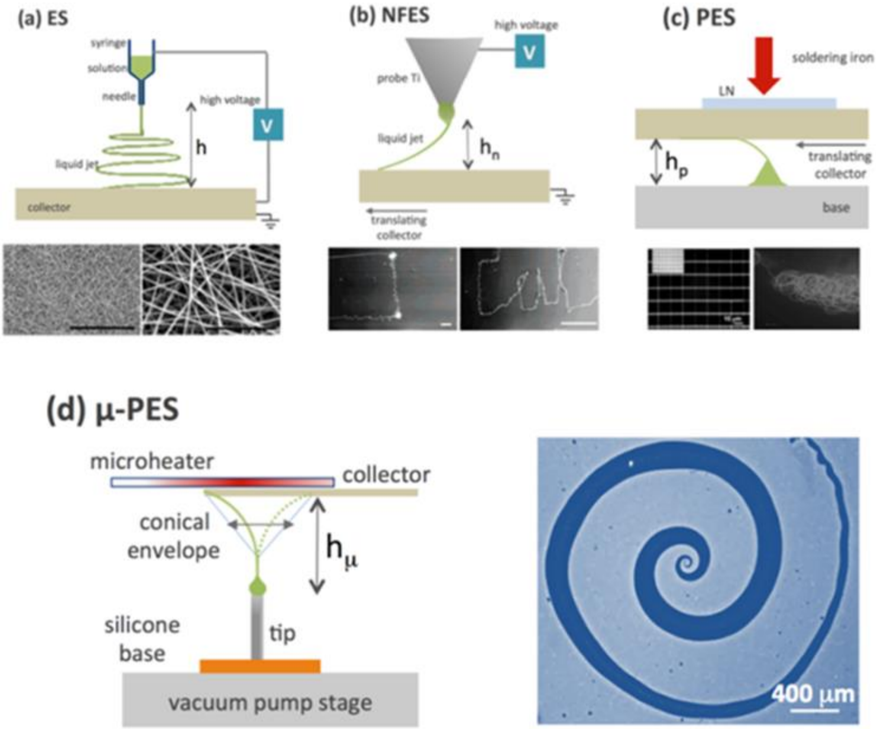

Figure 3.1: Schematic view and corresponding outcome for (a) traditional ES; (b) NFES; (c) PES; (d) m-PES with visualization of the superposition of the m-PES spiral (grey) over a golden spiral produced geometrically. The symbol h indicates the typical working distance for each setup and the subscript indicates the corresponding configuration (n, NFES; p, PES; m, m-PES). The distance h is in the range of centimetres, while hn, hp, hμ are in the range of millimetres.

These conditions, however, make the traditional ES be affected by the well-known whipping and chaotic bending of the fibre that produce the typical mats shown in **Figure 3.1(a)**. Aligned fibres are obtained by different approaches, as mentioned previously. The NFES introduces the tip in place of the nozzle in order to draw thinner fibres at shorter distances (up to 3 mm) and, consequently, at lower voltages (600 V ÷ 1000 V), thus reducing significantly the fibre whipping, as shown in **Figure 3.1(b)**. The PES is also nozzle-free and works at short distances as NFES, but, in addition, it is electrode-free, thus avoiding cumbersome external circuits by using the spontaneous pyroelectric charges. The translation or stationary state of the collector produces easily aligned or accumulated fibres as shown in **Figure 1(c)**. The μ-PES, instead, is an innovative configuration where the operation conditions enable to keep the bending behaviour regular for producing true spirals at microscale. In particular, as a new modified version of ES, it is able to sustain the intrinsic tendency of ES at producing spiral envelops avoiding the noise coming from the chaotic whipping, as shown in **Figure 1(d)**.

In summary, the μ-PES is able to condition the driving electric field into a distribution able to favour the tendency of the fibre in spinning spirally. Spiral structures are obtained by an easy and versatile approach based on a single step process, thus avoiding repetitive, time consuming and expensive lithographic procedures, or direct printing by mechanical scanning.

3.2 The μ-PES set-up

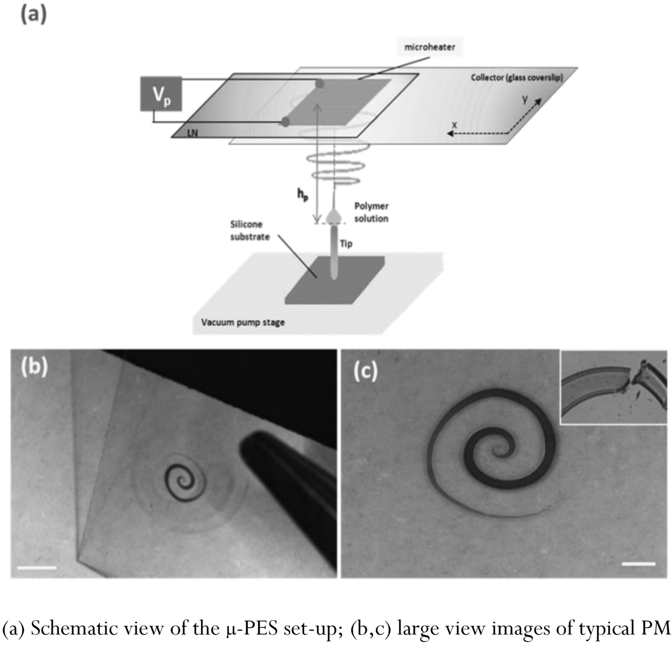

Figure 3.2: (a) Schematic view of the μ-PES set-up; (b,c) large view images of typical PMMA fibre spirals deposited onto a glass coverslip. Scale bars 20 μm. The inset shows a fibre cut by scalpel just after deposition, showing the rapid drying effect.

The μ-PES set up configuration presents two key differences compared to the first developed PES reported in [39]. Here the polymer drop (0.5μL) is deposited onto a metal tip positioned vertically and the pyroelectric effect is regulated by a µH integrated directly onto the surface of the $LiNbO_3$ crystal (LN-Crystal Technology Inc. in the form of c-cut wafers 500 µm thick and both sides polished with a surface quality of 40/20). A standard optical path with a high-speed CMOS camera (Motion Pro Y3-S1, pixel size 10.85 × 10.85 µm), allowed us to have a side view of the spinning process (see details in [39],[40])[1], while a traditional voltage generator drove the µH in order to have constant power dissipation. The collector was a glass coverslip mounted onto a conventional x-y translation stage (PI, Mercury C-863DC motor controller) that was stationary during the deposition of a single spiral and was moved when printing serial spirals. The collector was positioned between the base tip and the driving crystal at a typical distance ranging between around 80 µm and 1.4 mm, depending on the operation conditions.

The **µH** is made of a 300 nm Titanium (Ti) thin film. This material was chosen because a thin layer of oxide on its surface prevents the corrosion in various conditions. Three main process steps were performed for fabricating the µH: photolithography, thin film deposition, lift off. The LN surface was first spin coated with OIR-906 12i positive photoresist (~1.3 µm) and patterned photo lithographically. The photoresist was hard baked for 2 min at 95°C and the geometric pattern was developed using OPD-4624 developer for 1 min. In the second step, *e*-beam deposition technique was used for depositing 300 nm of titanium thin film on the pattern. Thereafter lift-off was performed for 20 min in acetone using a sonication bath. The µH area was around (3.5 × 3.5) mm^2 and its electrical resistance was about 460 Ohms. This µH was supplied by an external power supply (THURLBY THANDAR INSTRUMENTS, 32 V; 2 A). The power limit was 350 mW and the µH can be used indefinitely when respecting these limits, thus avoiding detrimental thermal shocks for the crystal.

PMMA is used here for demonstrating the reliability of the technique for different reasons, including its widespread use and the wide range of available solvents and concentrations. Poly(methyl methacrylate) (PMMA) (9011-14-7, Average molecular weight Mw ≈ 996,000 - Sigma Aldrich) was dissolved in anisole ($\eta = 1$ cP, $\varepsilon r = 3.6$, Microchem Corp., Newton, MA) at different concentrations (2-15 wt %) and stirred at 50°C for 1 hour.

---

[1] The camera provides a frame rate up to around 25 000 fps with a spatial resolution of 1280 × 1280 pixels.

3.3 Experimental results and characterization

Figure 3.2(a) shows the schematic view of the μ-PES set-up and **Figure 3.2(b,c)** show large view images of typical fibre spirals made of poly(methyl methacrylate) (PMMA) in anisole (9% wt/wt). The fibres appear to dry up just after deposition, as illustrated in the inset of **Figure 3.2(c)**, due to the μH that, simultaneously, drives the μPES and induces rapid evaporation of the solvent.

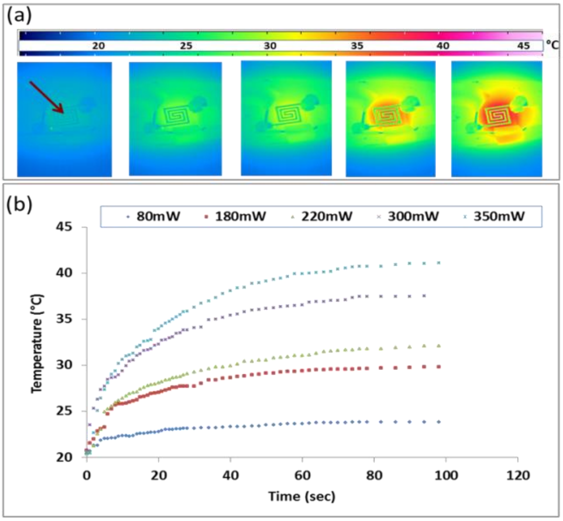

Figure 3.3: (a) Typical thermal camera images of the crystal during m-heating (the temperature increases from left to right); (b) corresponding temporal evolution of the crystal temperature for different operation powers in correspondence of the region evidenced by the red arrow in (a).

Figure 3.3(a) shows the typical thermal camera images of the crystal surface recorded during micro-heating[2], while **Figure 3.3(b)** presents the temporal evolution of the temperature values since the μH switches on and for different operation powers, measured across the region indicated by the arrow in **(a)**. The experimental results show clearly that the crystal temperature rose gradually till a sort of plateau for each power value, in correspondence of which the temperature variation is negligible. The maximum power used here was 350 mW, according to the μH operation limits, while the corresponding maximum temperature measured on the crystal surface was around 40°C. The polymer drop was pipetted manually onto the base tip and positioned in line with the μH, as shown schematically in

---

[2] The VarioCAM hr head (InfraTec Gmbh) was used for recording the thermal images. It had 640 × 480 microbolometres and the images were recorded by the thermographic software IRBIS 3.0.

Figure 3.2(a). The tip was fixed on a silicone substrate and attached to a vacuum pump, in order to dampen its vibrations. As well described in [35] the tip allows one to shrink rapidly the diameter of the Taylor cone, due to drop consuming during the process, leading to thinner fibres. The power supply of the μH was switched on and the base tip was translated upward vertically and slowly in order to feel the electric field generated by the LN crystal. The camera allowed us to have a side view of the base drop, and the vertical translation was stopped when the drop started to deform into a rotating fibre. The resulting tip-collector distance is called here 'working distance' (WD). Since the viscosity of the polymer is well known to influence the dynamics of ES [23,41], solutions of PMMA were prepared in anisole with different concentrations for characterizing the operation conditions.

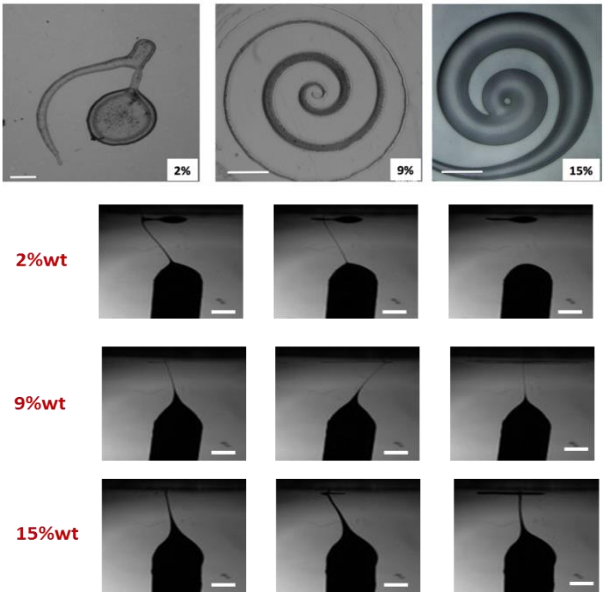

Figure 3.4: (Top) Optical microscope images of spiral fibres produced by μ-PES using PMMA solutions with different concentrations. The 2 % PMMA solution was obtained with an applied power of 320 mW at WD= 1.04 mm. The 9% PMMA solution with an applied power of 80 mW at WD= 0.11 mm. The 15 % PMMA solution was obtained with an applied power of 180 mW at WD= 0.08 mm (Scale bars 200 μm). These spirals correspond to the frames reported on the Bottom of the panel (extracted from the videos) for the three concentrations (scale bar 500 μm).

Figure 3.4 shows the optical microscope images of typical spiral fibres obtained by using three representative concentrations (2 wt%, 9 wt%, 15 wt%), while the frames show the corresponding camera view of the spiralling. The viscosity influences clearly both the thickness of the fibre and the morphology of the spiral pattern. The spiral revolution is relatively short for PMMA @ 2 % as well as for

PMMA @ 15% solution, but for different reasons. The PMMA @ 2 % has relatively abundant solvent that prevents the formation of an entangled network of polymer chains, thus generating an unstable fibre that breaks easily before completing the revolution (see the corresponding frames in **Figure 3.4**).

This is in full agreement with the analysis performed by Shenoy et al.[42] where they evaluated a threshold value of ~3.5 for the solution entanglement number, $(n_e)_{\text{sol}}$, in order to achieve continuous fibres. In fact, according to Shenoy et al.[42], the entanglement number in solution can be determined from **Eq. (1)** below.

$$(n_e)_{sol} = \frac{M_w}{(M_e)_{sol}} = \frac{M_w \phi_p}{M_e}$$

(1)

Here, M_w is the molecular weight of the polymer, ϕ_p is the polymer volume fraction, M_e is the entanglement molecular weight and $(M_e)_{sol}$ is the entanglement molecular weight in solution that is expressed by the **Eq.(2)**.

$$(M_e)_{sol} = \frac{M_e}{\phi_p}$$

(2)

In our case, considering $M_w = 996{,}000$ and $M_e = 12{,}500$ [43], the PMMA @ 2 % gives $(n_e)_{sol} \sim 1.6$, while the PMMA @ 9 % and the PMMA @ 15 % give $(n_e)_{sol} \sim 7.2$ and $(n_e)_{sol} \sim 12$, respectively.

Conversely, the lower solvent content in the PMMA @ 15 % induces a faster solvent removal during successive rounds, so that the contribution of the viscoelastic forces is higher, the fibre rotates slowly and stops earlier due to the hardening instead of the fibre breakup. The PMMA @ 9 % instead, exhibits the viscosity properties that favour the formation of a fibre revolution with the best stability and reliability, able to generate regular and relatively long spirals. In this case, the revolution is stopped typically by translating the base downward, away from the collector, essentially with the effect of switching off the EHD force on the base drop. The role of polymer concentration on the µ-PES was investigated deeper and the overall results are presented in **Figure 3.5** where a base drop of 0.5 µL was used in all experiments. **Figure 3.5(a)** shows the behaviour of the "activation distance" (AD) for different values of the µH power and for five indicative concentration values. In other words, for each power value and for each solution, the base was far away from the collector and was translated upward in order to find the longer base-collector distance at which the base drop deformed into a Taylor cone and started to eject liquid, but not necessarily formed spiralling fibres, namely the AD. In particular, the horizontal colour bars highlight the power ranges corresponding to the spiral formation for each solution. These results show clearly that the PMMA @ 9 % exhibits the best reactivity and reliability. In fact, neglecting the edge values of the µH power, its AD is always higher than in case of the other samples and always corresponds to spiralling fibres. **Figure 3.5(b)** gives information about the spiralling conditions, namely the minimum power required for getting a rotating fibre and the corresponding SD, for five concentration ranges. Negligible differences where observed within each range of concentrations. These results show that, in order to get spiralling fibres, PMMA @ 9 % requires the lowest µH power, equal to ~¼ of that required by the [2-7] % range and ~ ½ of that required by the [11-15] % range. **Figure 3.5(c)** shows the values of the SD for each sample solution, at a fixed power of 300 mW, namely the minimum value for getting spirals for all of the sample solutions (see **Figure 3.5(a)**). The PMMA @ 9 % gives fibres at a distance that is ~ 45 % longer than in case of the other samples. **Figure 3.5(d)** gives information about the "rotation length" and the "pattern diameter" for each sample, namely the average value of the duration of the fibre revolution and of the diameter of the spiral pattern, respectively. The power and the distance were fixed at 350 mW and 900 µm, respectively, in order to get a rotating fibre for each concentration value. These results show that, again, PMMA @ 9 % holds the record also in terms of longer spirals and wider resulting pattern, thus confirming its best attitude to generate long and regular spirals(see **Figure 3.5(d)**).

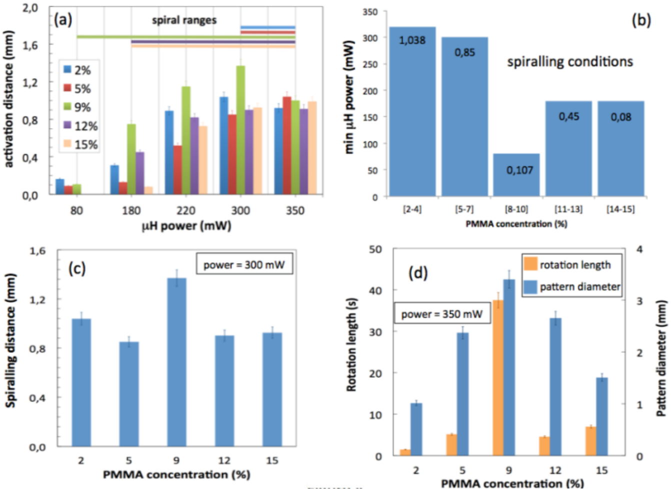

Figure 3.5: (a) Behaviour of the activation distance as a function of the µH power for different solution concentrations (the horizontal colour bar indicates the ranges corresponding to spiral formation); (b) minimum µH power values required for getting spirals for each concentration range (the values on the columns indicate the corresponding base-collector distance in mm); (c) spiralling distance values for each concentration at a fixed power of 300 mW; (d) rotation length and pattern diameter for each concentration at a fixed power of 350 mW. Mean values were evaluated over ten replicates of the experiments. The volume of the base drop was always fixed at 0.5 µL.

The overall results in **Figure 3.5** show clearly that the PMMA @ 9 % provides the viscoelastic properties able to generate the longest spirals with the best reliability. In other words, the 9 % value marks a region where the bending effects are best controlled, leading to spirals with high regularity and high rotation lengths, and with the less critical operation conditions. In fact, first of all, this sample is the only one that gives spirals for all of the power values and, as a direct consequence, it requires the lowest µH power for getting spirals and at even largest base-collector distance (see **Figure 3.5(a-c)**). The high content of solvent in the lower concentration range (2-7) % makes the drop to dispense liquid droplets and therefore longer distances and higher electric filds are required to enhance evaporation and favour spinning. Conversely, the behaviour of the samples with higher concentration range (11-15) % is dominated by the inertia of the high viscous solution that therefore requires higher electric field for spinning.

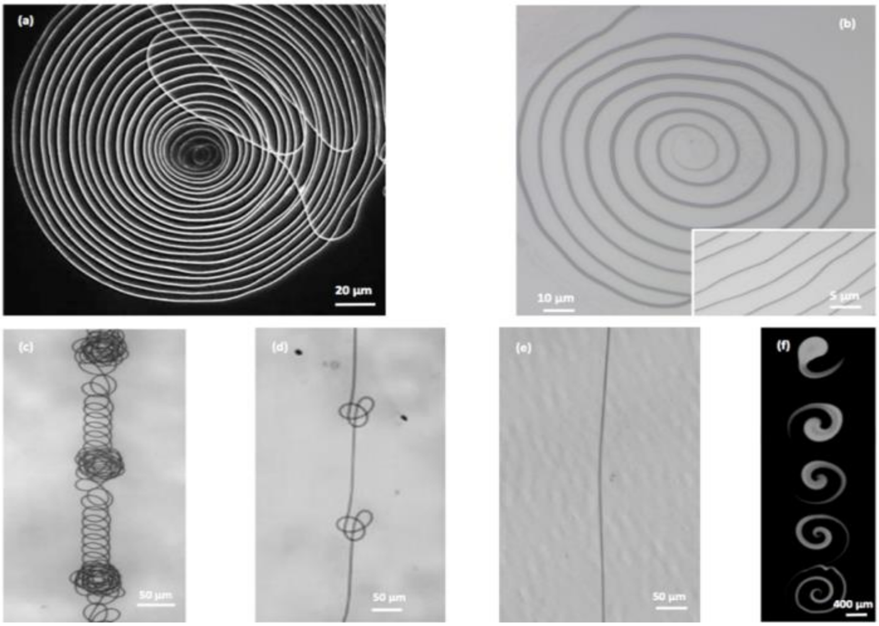

Figure 3.6: Optical microscope images of (a,b) thinner fibre spirals by the natural reduction of the volume of the base drop in the last steps of the process and (c,d,e) helical and straight fibres by translating the collector at different speeds: (c) 200 µm/s: (d)(e) 500 µm/s; (f) series of separated spirals from the same base drop, where the time flows from top to bottom. The clusters visible in (c) and (d) correspond to the sites where the stage was stopped. The few fibres laying on top correspond to the final stage of the spiralling that, in this case, was overdriven for getting the widest pattern.

Thinner spiral fibres were obtained easily by reducing the volume of the base drop, due to drop consuming, and **Figure 3.6 (a,b)** show two typical examples in case of 0.2 μL (base drop volume), according to previous findings on the subject [43]. The translation of the collector by a motorized stage during spinning allowed us to pattern helical or straight fibres as shown in **Figure 3.6(c,d,e)**, depending on the translation speed. The clusters visible in **Figure 3.6(c,d)** correspond to the stationary sites where the stage was stopped for accumulating the fibre, with about 2 s and 0.5 s in case of thicker and thinner clusters, respectively.

The identical geometry of the knot-like structures in **Figure 3.6(d)** demonstrates clearly the repeatability of the fibre revolution. **Figure 3.6(f)** shows a typical series of separated spirals obtained starting by the same base drop and by switching off the EHD force after each spiral completion. The time flows from top to bottom and, correspondingly, the spiral fibre thinned due to the volume decrease of the base drop.

3.4 Discussion and conclusion

As clarified above, the peculiarity of μ-PES configuration is its ability to keep under control those fibre bending effects that, instead, occurs chaotically in traditional ES. This results from the successful combination of the following key features: (1) tip support; (2) controlled electric field; (3) heating.

(1) The **tip support** for the reservoir, analogously to NFES, allows the electric field to draw smaller amounts of volumes and therefore thinner fibres at shorter distances, thus reducing the instabilities arising from longer flight distances. Moreover, compared to PES, the tip allows the jet to be more stable under the electric field especially in case of inks with lower viscosities and higher surface tensions, that is the case of PMMA solutions versus PLGA solutions.

(2) The **electric field** is generated here by the pyroelectric effect, as in case of PES[39], but with the key difference that the thermal stimulus is induced by the Joule effect at microscale, thanks to the μH operating at constant power dissipation. This ensures a controlled increase of temperature by regular intervals ΔT (see the rising curves in **Figure 3.3(b)**), avoiding the transient events typical of PES. Therefore, since the pyroelectric field is proportional to ΔT (see [39] and Refs therein), here the fibre spinning is regulated by a stationary electric field, analogously to ES. In fact, the μ-heating induces a slight temperature variation that makes crystal dipole molecules to misalign, leading to a corresponding change in polarization magnitude. As soon as the surface charges reorganize for compensating

the resulting nonzero field, the temperature increases again by almost the same gradient and, consequently, a similar charge mismatch occurs, with the final effect of providing the stationary electric field mentioned above. In other words, the uncompensated charge is continuously refilled by the same amount, thanks to the regular temperature variation. This is demonstrated experimentally by comparing the temporal behaviour of the μH in **Figure 3.3(b)** with the rotation length of the 9 % PMMA solution fibre in **Figure 3.5(d)**, both corresponding to about 40 s. This means that the stationary field exists and draws the fibre as long as the temperature rises, according to the pyroelectric effect. After rapid cooling down the crystal, the process can re-start.

(3) The **μH** contributes to the fibre spiralling by inducing simultaneously a gentle evaporation of the polymer solvent in the reservoir as well as upon deposition. The jet is liquid initially and becomes solid by the time it impinges on the target substrate, as evidenced in the inset of **Figure 3.2(c)**. The evaporation of the solvent in the reservoir enhances progressively the viscosity of the jet and, as a consequence, the viscoelastic force of the incoming fibre increases and balances the whipping effects related to the solvent charging. Therefore, at first approximation, the jet may be modelled as a thin elastic filament with an elastic modulus *K* that increases during jetting, thus leading to the spiralling effect as described below. Analogously to the studies performed by Kim et al [16], we consider here the inertial and the gravitational forces negligible compared with the electrostatic force. In order to evaluate the role of *K* in the formation of spirals, we balance the electrostatic torque $F_e R^2$ with the elastic torque KI/R [42](F_e is the electrostatic force, *R* is the radius of the spiralling fibre, *I* the area moment of inertia ~ r^4, *r* is the fibre's radius) and we obtain [42]:

$$R \approx \left(\frac{K}{\varepsilon_0 E^2} \right)^{1/3} r \tag{3}$$

Here the electric field is considered constant (~10^7 V/m [39]), ε_0 is the permittivity of free space (8.854×10^{-12} F/m) and *r* is the fibre thickness. As mentioned above, *K* increases during jetting and, as a consequence, *R* increases as well, thus leading to the spiral envelopes. Considering that the longer spirals may have fibre diameters of 0.8 μm and *R* values in the range of (3 ÷ 100) μm (see **Figure 3.6(a)**), a *K* value of about 1.8 GPa is obtained from (3) for the final jet, when the solvent evaporates almost totally. These results are in good agreement with values reported in literature for PMMA [49]. It is noteworthy that the spiralling effect is also favoured by the electrostatic repulsion between the charged fibre collected by the slide and the incoming threads.

It is important to note that in case of PES the solvent evaporation occurs as well, but there the transient nature of the electric field compromises the continuous and regular drawing of the fibre into a spiral. Moreover, it is noteworthy that the μ-heating process provides a more efficient thermal stimulus with pyroelectric fields similar to those obtained through PES but at temperatures around four times lower, with great advantages for all of those applications where the high temperatures can be detrimental, as in case of biological applications. The use of the tip expands the PES to polymers with lower viscosities and higher surface tension where the sessile drop configuration would be affected by significant instabilities (see ref [40]). Compared to other ES techniques, μ-PES provides the advantage of operating at lower voltages (10 V against tens of kV in ES and hundreds of V in NFES).

In conclusion, the results show how longer spirals can be obtained by controlling operation parameters that belong to polymer concentration and to EHD forces. In the following section, these self-sustained structures are demonstrated to be useful for investigating the response of live cells to intriguing multiscale spiral shapes, thus opening the route to a potential new platform for cell morphogenesis studies and for cochlea regeneration scaffolds.

3.5 Spiral templates for cell patterning applications

The cell adhesion on the selected spiral patterned substrates, was evaluated in vitro using mouse embryonic fibroblast cells (NIH-3T3). The cells were cultured in Dulbecco's modified Eagle's medium (DMEM) containing 4.5 g/L D-glucose and supplemented with 10 % FBS (fetal bovine serum), 100 units/mL penicillin, and 100 μg/mL streptomycin. The cells were harvested from the tissue culture flasks by incubation with a 0.05 % trypsin–EDTA solution for 5 min. The cells were then centrifuged and re-suspended in complete media. The cells were seeded on the patterned substrates at a density of 1105 cells/mL and were incubated into conventional 35 × 10 mm diameter Petri dishes at 37 °C and in humidified 5 % CO_2 atmosphere. The cell adhesion and spreading was observed over 24 h under a standard inverted optical microscope (AxioVert, Carl Zeiss, Germany).

It is well known that polymers like PMMA behave as cytophobic coatings [44], and **Figure 3.7(a)** shows the microscope image of a typical PMMA dot pipetted manually onto a conventional glass slide after 24 h plating with NIH-3T3 cells.

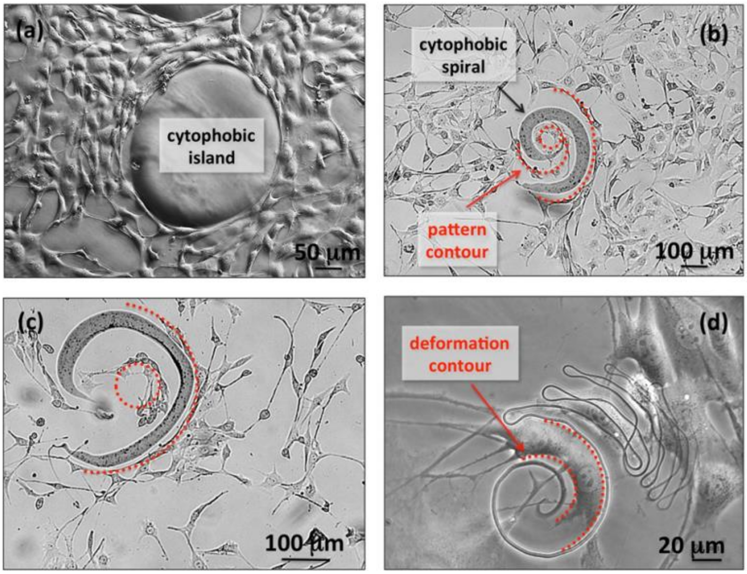

Figure 3.7: Optical microscope images of different PMMA patterns deposited onto a conventional glass slide and plated with the NIH-3T3 cells: (a) spot deposited by a pipette showing the cytophobic nature of PMMA; (b,c,d) spiral patterns with decreasing thickness of the fibre.

The cells clearly colonize the whole area around the dot, even across the edge of the dot, where the cells deform according to the curvature of the dot border. PMMA spirals, with different thicknesses, were deposited onto a conventional glass coverslip and incubated into Petri dishes with the NIH-3T3 cells. **Figure 3.7(b,c)** show the cell patterning obtained typically in correspondence of two thick spirals (15% PMMA solution), under large and magnified view, respectively. The cells clearly colonize the glass substrate surrounding the spiral assuming random shapes and orientations. Conversely, the cells adhering near the edge of the spiral elongate and orient significantly according to the curvature of the spiral, as highlighted by the red dashed lines. **Figure 3.7(d)** shows a typical result obtained in case of a thinner spiral (9% PMMA solution), after 24 h plating with NIH-3T3 cells. The peripheral envelope of the fibre is due to the receiving slide that was translated after deposition in order to enlarge the fibre interspace up to dimensions compatible with cell spreading. In fact, in this case, the spiral template has dimensions on the scale of the cell size, and clearly forces the cells adhering the interspace to deform according to the curvature of the spiral, as evidenced by the red contour.

Figure 3.7 shows the potential use of these patterns for controlling the morphology of live cells at microscale along regular spiral shapes. It is well known that cell orientation and shape can be predictive of cell fate, and great efforts are being conducted in the wide field of tissue engineering for developing new platforms able to control the cell morphology. The results shown in **Figure 3.7** demonstrate the possibility of using these spiral templates for addressing the cell adhesion via a versatile and multiscale technique, avoiding expensive and time-consuming lithographic methods.

In fact, large-scale spirals are able to orient a population of cells along these well-defined geometries (see **Figure 3.7(b,c)**), while small-scale spirals can drive the spiral deformation down to single cell (see **Figure 3.7(d)**). The possibility to modulate both the cell orientation and the cell shape onto well-defined and multiscale geometries is of great interest for investigating the cell functions and morphogenesis induced by cell micropatterning. The possibility to dispose of these multiscale spiral templates by a relatively easy to accomplish technique, that avoids expensive and time-consuming lithographic processes, may open the route to the investigation of cell response to spiral cues as well as to the development of a new versatile platform for cochlea regeneration scaffolds.

References

[1] D. Bodas, C. Khan-Malek, “Direct patterning of quantum dots on structured PDMS surface”, *Sensors Actuators B Chem.* **128,** 168–172, (2007)

[2] A. Martinez, J. Castany, D. Mercado, “ Characterization of viscous response of a polymer during fabric IMD injection process by means a spiral mold.”, *Measurement* **44,** 1806–1818, (2011)

[3] J. Paek, I. Cho, J. Kim, “Microrobotic tentacles with spiral bending capability based on shape-engineered elastomeric microtubes.”, *Sci. Rep.* **5,** 10768-10, (2015)

[4] L. Chen, H. Guo, X. Xia, G. Liu, H. Shi, M. Wamg, Y. Xi, C. Hu, “Novel Spiral-Like Electrode Structure Design for Realization of Two Modes of Energy Harvesting”, *ACS Appl. Mater. Interf.* , **7**, 16450-7, (2015)

[5] T. Kan, A. Isozaki, N. Kanda, N. Nemoto, K. Konishi, H. Takahashi, M. Kuwata-Gonokami, K. Matsumoto, I. Shimoyama, “Enantiometric switching of chiral metamaterial for terahertz polarization modulation empolying vertically deformable MEMS spirals.” *Nat. Comm.* , **6**, 8422-7, (2015)

[6] C.A. Pickover, “ Mathematics and Beauty: A Sampling of Spirals and ‘Strange’ Spirals in Science”, Nature and Art. *Leonardo,* **21,** 173–181, (1988)

[7] B.B. Mandelbrot,” The fractal geometry of nature.” *New York, W.H. Freeman and Co.* (1983)

[8] C.-R. Li, A.-L. Ji, L. Gao, Z.-X. Cao, “ Stressed Triangular Tessellations and Fibonacci Parastichous Spirals on Ag Core/SiO_2 Shell Microstructures.”, *Adv. Mater.* **21,** 4652–4657, (2009)

[9] C. Li, A. Ji, Z. Cao, “ Stressed Fibonacci spiral patterns of definite chirality.”, *Appl. Phys. Lett.* , **90,** 164102-3,(2007)

[10] M.-K. Shin, S.-I. Kim, S.-J.Kim, ”Controlled assembly of polymer nanofibers: From helical springs to fully extended.”, *Appl. Phys. Lett.* ,**88,** 223109-3, (2006)

[11] R. Kessick, G. Tepper, “ Microscale polymeric helical structures produced by electrospinning”, *Appl. Phys. Lett.* **84,** 4807-3, (2004)

[12] S.P. Shariatpanahi, A. Iraji zad, I. Abdollahzadeh, R. Shirsavar, D. Bonn, R. Ejtehadi, “Micro helical polymeric structures produced by variable voltage direct electrospinning.” *Soft Matter* **, 7,** 10548-10551,(2011)

[13] M.H. Godinho, J.P. Canejo, L.F.V. Pinto, J.P. Borges, P.I.C. Teixeira, “ How to mimic the shapes of plant tendrils on the nano and microscale: spirals and helices of electrospun liquid crystalline cellulose derivatives.”, *Soft Matter* , **5,** 2772-2776,(2009)

[14] M.H. Godinho, J.P. Canejo, G. Feio, E.M. Terentjev, “ Self-winding of helices in plant tendrils and cellulose liquid crystal fibers.”, *Soft Matter* **, 6,** 5965-5970, (2010)

[15] G. Chang, X. Zhu,R.Warren, X. Wang, T. He, L. Lin, J. Shen,” Electrospinning of micro spiral fibers.”, *Mater. Res. Express* **1,** 1–7, (2014)

[16] H.-Y. Kim, M. Lee, K.-J. Park, S. Kim, L. Mahadevan, “ Nanopottery: coiling of electrospun polymer nanofibers.” *Nano Letters* **10**, 2138–40, (2010)

[17] P.P. Bhat, S. Appathurai, M.T. Harris, M. Pasquali, G.H. McKinley, O.A. Basaran, “ Formation of beads-on-a-string structures during break-up of viscoelastic filaments.”, *Nat. Phys.* **6,** 625–631, (2010)

[18] R.T. Collins, J.J. Jones, M.T. Harris, O.A. Basaran, “Electrohydrodynamic tip streaming and emission of charged drops from liquid cones.” *Nat. Phys.* **4,** 149–154, (2007)

[19] J.-U.Park, S. Lee, S. Unarunotai, Y. Sun, S. Dunham, T. Song, P.M. Ferreira, A.G. Alleyene, U. Paik, J.A. Rogers, “Nanoscale, electrified

liquid jets for high-resolution printing of charge.", *Nano Lett.* **10,** 584–591, (2010)

[20] J.U. Park, M. Hardy, S.J. Kang, K. Barton, K. Adair, D. Mukhopadhyay, C.Y. Lee, M.S. Strano, A.G. Alleyne, J.G. Georgiadis, P.M. Ferreira, J.A. Rogers, "High-resolution electrohydrodynamic jet printing.", *Nat. Mater.* **6,** 782–789, (2007)

[21] J. Schneider, P. Rohner, P. Galliker, S.N. Raja, Y. Pan, M.K. Tiwari, D. Poulikakos, "Site-specific deposition of single gold nanoparticles by individual growth in electrohydrodynamically-printed attoliter droplet reactors.", *Nanoscale* **7**, 9510–9, (2015)

[22] P. Galliker, J. Schneider, H. Eghlidi, S. Kress, V. Sandoghdar, D. Poulikakos, "Direct printing of nanostructures by electrostatic autofocussing of ink nanodroplets.", *Nat. Commun.,* **3,** 890-9, (2012)

[23] N. Bhardwaj, S.C. Kundu, " Electrospinning: a fascinating fiber fabrication technique.", *Biotechnol. Adv.* **28,** 325–47, (2010)

[24] I.C. Um, D. Fang, B.S. Hsiao, A. Okamoto, B.Chu,"Electro-spinning and electro-blowing of hyaluronic acid.", *Biomacromolecules* **5,** 1428–1436, (2004)

[25] E.-R. Kenawy, J.M. Layman, J.R. Watkins, G.L. Bowlin, J.A. Matthews, D.G. Simpson, G.E. Wnek, "Electrospinning of poly(ethylene-co-vinyl alcohol) fibers.", *Biomaterials* **24,** 907–913, (2003)

[26] W. Yang, H. Duan, C. Li, W. Deng, " Crossover of Varicose and Whipping Instabilities in Electrified Microjets.", *Phys. Rev. Lett.* **112**, 054501-5, (2014)

[27] Y. Dzenis, "Material science. Spinning continuous fibers for nanotechnology.", *Science* **304,** 1917–9, (2004)

[28] T. Subbiah, G.S. Bhat, R.W. Tock, S. Parameswaran, S.S. Ramkumar, " Electrospinning of nanofibers",. *J. Appl. Polym. Sci.,* **96**, 557–569, (2005)

[29] A. Welle, M. Kröger, M. Döring, K. Niederer, E. Pindel, I.S. Chronakis, " Electrospun aliphatic polycarbonates as tailored tissue scaffold materials.", *Biomaterials* ,**28,** 2211–9, (2007)

[30] S. Ramakrishna, K. Fujihara, W.-E. Teo, T. Yong, Z. Ma, R. Ramaseshan, "Electrospun nanofibers: solving global issues.", *Mater. Today* **9**, 40–50 (2006)

[31] A.A.S. Bhagat, S.S. Kuntaegowdanahalli, D.D. Dionysiou, I. Papautsky," Spiral microfluidic nanoparticle separators.", *Proc. SPIE* , 6886**,** 68860M–11, (2008)

[32] H.W. Hou, M.E. Warkiani, B.L. Khoo, Z.R. Li, R.A. Soo, D.S.-W. Tan, W.-T. Lim, J.Han, A.A.S. Bhagat, C.T. Lim, " Isolation and retrieval of circulating tumor cells using centrifugal forces.", *Sci. Rep.* **3,** 1259-8, (2013)

[33] X. Wang, B. Ding, B.Li, " Biomimetic electrospun nanofibrous structures for tissue engineering. ", *Mater. Today* ,**16,** 229–241, (2013)

[34] L. Persano, A. Camposeo, D. Pisignano, "Active polymer nanofibers for photonics, electronics, energy generation and micromechanics.", *Prog. Polym. Sci.*,**43,** 48–95, (2014)

[35] D. Sun, C. Chang, S. Li, L. Lin, " Near-field electrospinning.", *Nano Lett.,* **6,** 839–42, (2006)

[36] C. Chang, K. Limkrailassiri, L. Lin, " Continuous near-field electrospinning for large area deposition of orderly nanofiber patterns.", *Appl. Phys. Lett.*, **93**, 123111, (2008)

[37] H. Yuan ,S. Zhao , H. Tu, B. Li , Q. Li, B. Feng , H. , Y. Zhang , " Stable jet electrospinning for easy fabrication of aligned ultrafine fibres.", *J. Mater. Chem.* **, 22**, 19634-19638, (2012)

[38] Q. Zhou, M. Bao, H. Yuan ., S. Zhao, W. Dong , Y. Zhang, " Implication of stable jet length in electrospinning for collecting well-aligned ultrafine PLLA fibers.", *Polymer* **, 54**, 6867–6876, (2013)

[39] S. Coppola, V. Vespini, G. Nasti, O. Gennari, S. Grilli, M. Ventre, M. Iannone, P.A. Netti, P. Ferraro, "Tethered Pyro-Electrohydrodynamic Spinning for Patterning Well-Ordered Structures at Micro- and Nanoscale", *Chem. Mater.* **, 26,** 3357–3360, (2014)

[40] O. Gennari, L. Battista, B. Silva, S. Grilli, L. Miccio, V. Vespini, S. Coppola, P. Orlando, L. Aprin, P. Slangen, P., Ferraro, " Investigation on cone jetting regimes of liquid droplets subjected to pyroelectric fields induced by laser blasts.", *Appl. Phys. Lett.* ,**106,** 054103-3, (2015)

[41] S.L. Shenoy, W.D. Bates, H.L. Frisch, G.E. Wnek, "Role of chain entanglements on fiber formation during electrospinning of polymer solutions: good solvent, non-specific polymer–polymer interaction limit.", *Polymer* **, 46,** 3372–3384, (2005)

[42] L.D. Landau E.M. Lifshitz *Theory of Elasticity*, 3rd ed. Butterworth-Heinemann: London , (1986)

[43] S. Grilli, L. Miccio, O. Gennari, S. Coppola, V. Vespini, L. Battista, P. Orlando, P. Ferraro, " Active accumulation of very diluted biomolecules by nano-dispensing for easy detection below the femtomolar range.", *Nat. Commun.* ,**5,** 5314-6, (2014)

[44] M. Buttiglione, F. Vitiello, E. Sardella, E. Petrone, M. Nardulli, P. Favia, R. d'Agostino, R. Gristina, " Behaviour of SH-SY5Y neuroblastoma cell line grown in different media and on different chemically modified substrates.", *Biomaterials* , **28**, 2932-2945, (2007)

[45] D.H. Reneker, A.L. Yarin, H. Fong, S. Koombhongse, " Bending instability of electrically charged liquid jets of polymer solutions in electrospinning",. *J. Appl. Phys.* , **87,** 4531-4547, (2000)

[46] D.H. Reneker, A.L. Yarin, " Electrospinning jets and polymer nanofibers.", *Polymer* **, 49**, 2387–2425, (2008)

[47] Y.M. Shin, M.M. Hohman, M.P. Brenner, G.C. Rutledge, "Electrospinning: A whipping fluid jet generates submicron polymer fibers.", *Appl. Phys. Lett.,* **78,** 1149-1151, (2001)

[48] K. Garg, G.L. Bowlin, “ Electrospinning jets and nanofibrous structures.”, *Biomicrofluidics* , **5,** 013403-19, (2011)

[49] C. Ishiyama, Y. Higo, “Effects of humidity on Young’s modulus in poly(methyl methacrylate)”, *Journal of Polymer Science Part B - Polymer Physics,* **40**, 460-465, (2002)

[50] S.C. Chen, M. Mrksich, S. Huang, M. Whitesides, D. Ingber, “Geometric control of cell life and death.”, *Science* , **276**, 1425-1428, (1997)

[51] M. Ventre, F. Causa, P.A. Netti,”Determinants of cell-material crosstalk at the interface: towards engineering of cell instructive materials.”, *J. R. Soc. Interface* , **9**, 2017-20132, (2012)

[52] M. Théry, “Micropatterning as a tool to decipher cell morphogenesis and functions”, *J. Cell Sci.* , **123**, 4201-13, (2010)

Chapter 4

Nanocomposite polymer membranes as macroscale thermal sources

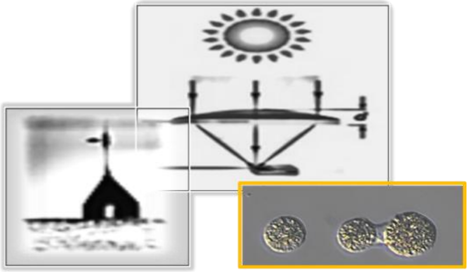

The experimental trials reported in this chapter arose with the aim, as for Chapter 3, to find alternative forms of pyroelectric crystal heating in order to overcome the limitations deriving from the use of the classical ones. The enhancement of the thermal gradient needed for the process activation and the improvement of the pyroelectric field selectivity and intensity, allow to obtain a better flexibility in the application fields tested. In fact, after evaluating different nanocomposite materials exhibiting efficient radiation absorption as coatings for the pyroelectric crystal, we explored three different solutions based on this so generated 'enhanced pyroelectric field'. In particular, in the first part, a solar energy harvesting based on a coated LN crystal is developed; in the second part, the nanocomposite coating for the ferroelectric crystal is used to trigger pyro-EHD ink-jet printing and finally, polymer fibres obtained by means of a carbon black-based pyro-electrospinning are demonstrated to self-assembly in ordered arrays of micro beads designing a 'dotted way' useful for cell patterning applications.

The key feature for all the applications proposed below, is represented by the nanocomposite membrane (a dispersion of carbon black (CB) in Polydimethylsiloxane (PDMS)) used as coating. The membrane production method consists in the preparation of a PDMS/CB film on Polyvinyl Alcohol (PVA) coated glass substrate followed by its peeling from the substrate and by the subsequent application, at a later stage, of the resulting PDMS/CB membrane directly onto the crystal.

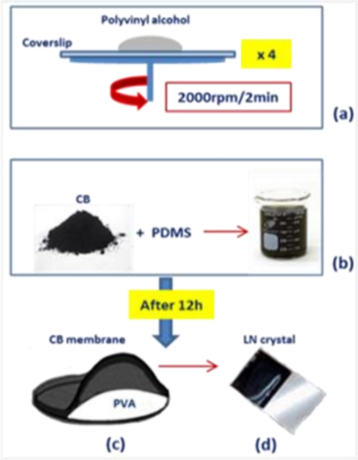

Figure 4.1: Schematic diagram of the CB deposition process

In detail, the glass substrate, a microscope coverslip, was functionalized by spin-coating a PVA solution (2.8% in water) at 2000 rpm for 2 minutes. This step was repeated four times to produce a film thick enough to allow the easy peeling of the membrane (**Figure 4.1(a)**). Then, a CB suspension was prepared in PDMS (**Figure 4.1(b)**) by adding 0.02 g of CB (graphitized CB-carbon nanopowder, size < 200nm, > 99.95%) in 0.5 g of PDMS curing agent (Dow Corning Sylgard 184; 10:1 pre-polymer to curing agent), and sonicating it for 2h. A drop of the suspension obtained after adding the elastomeric base to the solution, was finally deposited on the top of the PVA-coated coverslip and cured at room temperature for 12 hours. Once the CB membrane was peeled off from the coverslip (**Figure 4.1(c)**), it was set down on the crystal (**Figure 4.1(d)**). In the following sections, this coated LN crystal is used as pyroelectric element by means of a halogen Osram lamp (focal length:32.0 mm, 12V, 75 W) acting as heating source operating on the CB coated crystal.

4.1 Pyroelectric solar energy harvesting

Due to the growing interest in renewable energy sources, much research is being directed toward harvesting energy from natural resources. Power harvesting is the process by which useful electrical energy is extracted from external energy sources, above all from otherwise wasted energy, and stored for performing sensing and actuation and other applications, using smart materials as transducers. These materials have the ability to convert one form of energy into another. In the literature, several energy harvesting strategies for extracting useful amount of energy from ambient sources, as well as the power densities achievable using various methods, have been discussed [1–7]. In particular, the use of pyro-electricity for energy harvesting has been widely investigated over the past years, but probably it has not received the same attention dedicated to the other processes. Recently, modeling and experimental measurements have shown that pyro-electricity is a feasible way to generate electrical current from a time-dependent temperature fluctuation and pyro-electric crystals show interesting possibilities to be used in self-powered micro and nano-generator or sensors that require only μW-mW power [8–15]. As an example, Cuadras et al. tested PZT (Lead Zirconate Titanate) and PVDF (Polyvinylidene fluoride) as potential pyro-electric materials thus demonstrating that using pyro-electric materials to harvest energy can be cost competitive with thermo-electrics. Moreover, it was shown that pyro-based devices have the potentialities to be several times as efficient as thermo-electrics under comparable operating conditions [8]. Most of the proposed pyro-electric energy harvesting system are based on the use of an heat-sink and heat-source at given temperatures and a resonant mechanical system allowing to a pyro-electric crystal to experience temporal variation of temperature by means of its contact (or proximity) with the hot and the cold side of the device, alternatively [1, 16–17]. Nevertheless, for all these harvesters the time temperature fluctuations are always generated by external means. Focusing on pyro-electric generators driven by solar radiation (as the only medium to provide temperature variation), we were able to find just a couple of prototype systems proposed in recent years. A method to increase the efficiency of a solar cell, by depositing a coating of pyroelectric film on a surface of a solar cell has been proposed [18]. However, in this case pyro-electric effect is exploited just to support the efficiency of photovoltaic cell. Another technique to harvest solar thermal energy using a pyro-electric material (i.e. PZT) and exploiting wind fluctuations has been demonstrated; however, direct solar exposition of pyro-electric harvester not always allow to reach wide amplitude of the temperature variation [19].

In this chapter, we describe a new system for **solar energy harvesting based on the pyro-electric effect**, enhanced by an optical system focusing the solar radiation and a nanocomposite material exhibiting efficient radiation absorption as a coating for the pyro-electric crystal (i.e. functionalized coatings based on carbon-black (CB)). Our aim is to develop a pyro-electric energy harvester able to improve the amplitude of the temperature variation due to solar exposition/thermal stimulus and, as a consequence, the efficiency of energy harvesting process. A first demonstrator device (i.e. an electric generator) has been built with the aim to proof the principle and its performances have been analyzed through experiments and acquisitions in an indoor and outdoor environment. Finally, changes in efficiency related to different optical systems have been reported and discussed.

4.1.1 Principle of Operation

The pyro-electric effect has been used recently for wettability patterning, particle trapping, liquid microlenses, pyro-EHD (Electro-Hydro-Dynamics) liquid dispensing and manipulating liquid crystal droplets on the substrate surface [20–24]. In all the above applications a z-cut Lithium Niobate ($LiNbO_3$) ferroelectric crystal was employed because of its high Curie temperature (i.e. 1210°C), as described in Chapter 2.

Energy harvesting based on pyro-electricity typically relies on the use of materials exhibiting a so-called pyro-electric effect [21], i.e. emerging of free electric charges on the surface of a pyro-electric crystal experiencing a temporal variation of temperature. The relationship between the temporal variation of electrical charges (i.e. pyro-electric current) I_P and the temporal variation of temperature is:

$$I_P = \frac{dQ_P}{dt} = p_A \cdot A \cdot \frac{dT}{dt} \tag{1}$$

where p is the pyro-electric coefficient vector and p_A is its orthogonal component to the surface A covered by the electrode, T is the temperature of the crystal (supposed to be uniform over the whole material), t is the time and Q_P is the electrical charge due to pyro-electric effect which can be caught and managed by an external circuit. As a consequence, the emerging of pyro-electric charges is associated with a differential voltage V_P across the crystal. The electric charges may be stored in a capacitor C_E and, in the case of a fluctuating voltage $V_{CE}(t)$ across the condenser, the stored energy $E_{CE}(t)$ also fluctuates and, as a consequence, the electrical power $P_{CE}(t)$ flows into or out of the capacitor and can be found as:

(2)
$$P_{CE} = \frac{dE_{CE}}{dt} = \frac{d}{dt}\left(\frac{1}{2} C_E \cdot V_{CE}^2\right) = C_E \cdot V_{CE}(t) \cdot \frac{dV_{CE}}{dt}$$

The proposed harvester is based on an optical system focusing solar radiation onto a pyro-electric crystal, whose face exposed to the heat source is coated with a radiation absorbing material. The focusing of solar energy on the crystal, by means of an optical system, allows one to reach a temperature onto the crystal that is greatly higher compared to the case of a crystal plainly exposed to solar radiation without any radiation concentration systems. Moreover, the radiation absorbing polymer nano-composite material used as a coating of the pyro-electric crystal is able to significantly improve the solar radiation absorption and, as a consequence, to increase the amplitude of temperature variation. Indeed, coatings with high absorptivity and low thermal mass applied on pyro-electric crystals (e.g. lithium niobate) allow the conversion of a large fraction of the incident radiation into heat so that the resulting rise in temperature per unit of incident radiant power is maximized, as discussed in previous studies on IR detectors [25–26]; moreover, as reported above, the $LiNbO_3$ is transparent from 320 to 5000 nm [27–28] and its absorption in the visible range is quite scarce, so the use of an absorbing coating with an higher absorbing coefficient and a wider spectral absorbance, allows the improvement of the efficiency of the proposed device, so that also the whole UV, visible and IR wavelengths of solar radiation are involved in the energy harvesting (**Figure 4.2(a)**).

Lens	Focal length, *f* [mm]	Surface *S* [cm^2]
Plano-convex lens	200.0	20.2
Fresnel lens (A)	70.0	122.7
Fresnel lens (B)	178.0	615.4

Table 4.1: Characteristics of refractive focusing systems.

In this work, as shown in **Table 4.1**, three different refractive focusing systems have been used. The optical refractive systems used are characterized by a wavelength range from 195 to 2100 nm for the plano-convex lens (Newport SPX049) and from 200 to 2100 nm for the aspheric Fresnel lenses and, as a consequence, they are suitable to be used to involve most of solar spectrum (from 200 to 2500 nm).

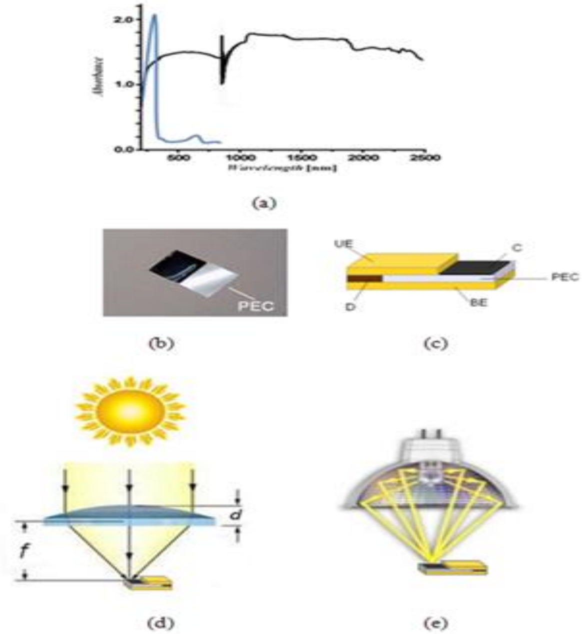

Figure 4.2: (a) Absorbance spectrum of CB powder (in black) [29] and of pure $LiNbO_3$ (in blue) [27]. The presence of CB based coating allows to involve the whole UV, visible and IR spectrum in the solar energy harvesting. (b) Pyro-electric element with absorbing coating. (c) Scheme of pyro-electric sample attached to metal electrodes. (d) Scheme of optical focusing system used outdoor (d = 6.584 mm and f = 200 mm for the plano-convex lens). The pyro-electric element is placed in front of the lamp and at a distance equal to its focal length (e) Scheme of experimental setup used in laboratory. UE: upper electrode; BE: bottom electrode; D: dielectric slab; PEC: pyro-electric crystal; C: absorbing coating.

4.1.2 Results

With reference to the setup shown in **Figure 4.2,** various experiments were carried out in order to evaluate the performances of the proposed solar pyro-electric energy harvester. The pyro-electric crystal (PEC) was a $LiNbO_3$ wafer (z-cut, 0.5 mm thickness, surface quality 40/20) with a surface of 14 mm × 28 mm, placed on the metal electrode BE. A half of the upper surface of the crystal has been covered by means of the absorbing polymer composite coating C and the second half is attached to the upper electrode UE (**Figure 4.2(c)**). With reference to the setup shown in **Figure 4.2(d)**, the optical refractive system has been placed with the convex surface in front of the sun in order to focus the solar radiation in the middle of the coated surface of the crystal. The temporal variation of temperature experienced by the $LiNbO_3$, due to focused solar radiation and to wind fluctuations, causes the emerging of electric charges on the pyro-electric crystal. The charges are collected by means of the metal electrodes and then are sent to an external circuit (implementing the so called “pyro-electric voltage method” [15–18]). The electric circuit comprises a full wave-rectifier (made with four rectifier diodes 1N4007), an electrical condenser CE for storing energy harvested and a resistive load R_L. During the experimental trials, an orange high efficiency LED Kingbright L934ED (forward voltage: 2.00 V; DC forward current: 25 mA; capacitance: 15 pF at 1 MHz) has been powered by our pyro-generator(**Figure 4.4(b)**). In order to quantify the energy harvested, the voltage V_{CE} across the electrical condenser CE has been recorded by means of a data acquisition system (with a sampling frequency of 100 Hz) connected to a laptop. The voltage follower B (STMicroelectronics TL084) has been used in order to isolate the experimental setup from the measurement system. The circuit for the measurement of pyro-electric voltage V_{PE} and for energy harvesting is reported in **Figure 4.3**, where the pyro-electric crystal is schematized as a current generator I_P and a condenser in parallel with electrical capacitance C_P.

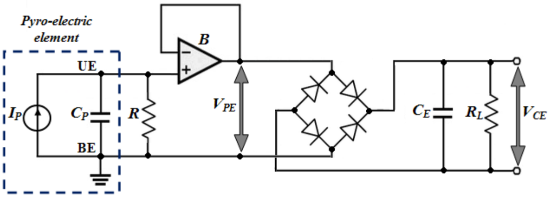

Figure 4.3: Scheme of the measurement circuit. R=1 MΩ. UE: upper electrode; BE: bottom electrode; B: voltage follower.

Experiments have been performed both in laboratory with artificial radiation (**Figure 4.2(e)**) and outdoor with solar radiation (**Figure 4.2(d)** and **Figure 4.4**). A halogen lamp with a reflector has been used in order to simulate solar radiation and the pyro-electric element has been placed in front of the lamp and at a distance equal to its focal length (**Figure 4.2(e)**). The surface power density of solar radiation [33] typically ranges from 10 mW/cm^2 to 100 mW/cm^2, contrary to the ones of halogen lamps [34] typically from 300 mW/cm^2 to 3000 mW/cm^2; moreover, wavelength range of sunlight is from 200 to 2500 nm [29–30] and spectrum of the used tungsten-halogen lamp with reflector used is from 200 to 2500 nm.

In order to evaluate the performances of the pyro-electric harvester, the experimental setup shown in **Figure 4.2(e)** has been used to carry out preliminary tests in the laboratory. The results of the considered experimental trials allow to find a preferred value of the electrical capacitance CE (i.e. 2.2 μF).

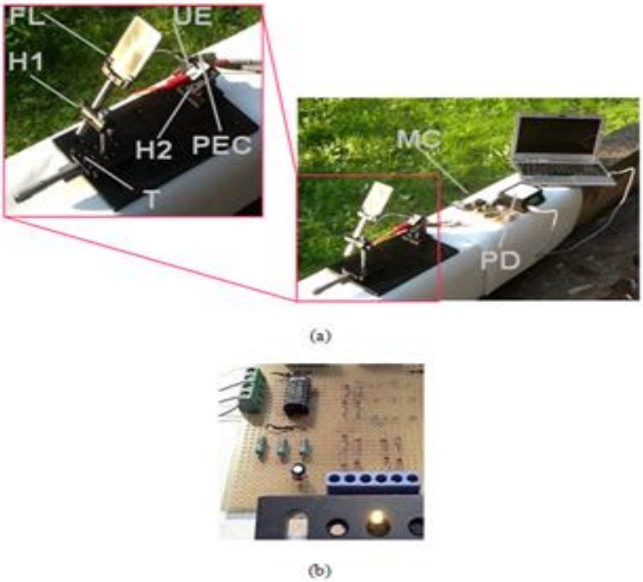

Figure 4.4. (a) Experimental setup used outdoor. FL: Fresnel lens; PEC: pyro- electric crystal with CB based coating; MC: measurement circuit; PD: portable data acquisition card USB powered; T: micrometric translator; UE: upper electrode; H1: holder for lens; H2: holder for the pyro-electric element. (b) LED powered by the pyro-electric harvester.

After the aforementioned experiments carried out in the laboratory, the experimental setup shown in **Figure 4.2 (e)** has been used in order to evaluate the performances of the pyro-electric harvester during solar exposition performed outdoor. In this experimental session, the three different refractive optical systems and the CB coating have been used; moreover, the value of the electrical capacitance of the condenser CE has been set to 2.2 μF, according to the results of the previous trials performed in the laboratory. The experiments were carried out in Pozzuoli, Naples, Italy, on 17 December 2013 at about 12:30 p.m., with an air temperature of 13 °C and wind speed of 9 km/h. According to the setup shown in **Figure 4.2(e)** , the plano-convex lens has been used to focus solar radiation on the pyro-electric crystal with CB based coating; the differential voltage V_{CE} measured across the electrical experiences several sudden increasing but they are followed by likewise reductions bringing the voltage around a null value, meaning that at the steady state no energy can be stored in the condenser CE. Conversely, by using the Fresnel lens A, sixfold over the previous one, the frequency of the voltage step boosts increases and the condenser CE is able to store energy while supplying of the load RL (**Figure 4.4(b)**); indeed, the differential voltage across the condenser CE can be kept to a mean value greater than 2 V for more than several tens of seconds, meaning that the LED can be turned on because the voltage is greater than its forward voltage. However, after this temporal window, the differential voltage can reach the null value and after some seconds, it starts again to increase with a temporal pattern similar to the previous one. This behavior has been observed also with a Fresnel lens with a larger surface (Fresnel lens B), but in this case a larger frequency of the voltage step boosts has been observed during some temporal windows of experiment. However, a solar exposition performed with this lens for more than about 60 s, can cause the combustion of CB based coating and, as a consequence, this arrangement has not been tested deeply. Anyway, the efficiency of energy harvesting grows with the diameter of the lens, as expected and as confirmed by means of the results obtained from the measurements of temperature of the coated pyro-electric element performed with the thermal camera; the local maximum temperature experienced on the pyro-electric element with CB based coating is equal to about 159 °C for plano convex-lens and is greater than 250 °C for the two Fresnel lenses (more information on the temperature reached by the crystal are not available because the full scale range of our thermal camera is 250 °C).

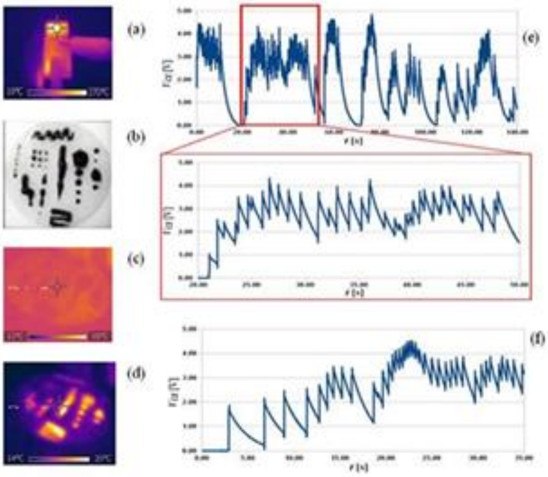

Figure 4.5:(a) Thermal map of pyro-electric element with CB coating. (b) Different shape of CB based coating deposited on the surface of $LiNbO_3$. (c, d) Thermal map of pyro-electric element with distributed CB coating before radiation exposition to halogen lamp (c) and after the beginning of radiation exposition to halogen lamp (d). (e, f) The measurements of differential voltage VCE across the electrical condenser CE during experimental trials carried out with lithium niobate crystal with (e) the carbon black coating and the Fresnel lens A and (f) the GP coating and the Fresnel lens B.

4.1.3 Discussion and conclusion

The experimental results shown in **Figure 4.5** confirm that the proposed device can be successfully used for solar energy harvesting. However, the experiments reported here are only a preliminary step of this study and other harvester configurations should be developed and tested also during summer or different season, allowing a surface power density of solar radiation greater than the one occurred during the days in which experiments were carried out. By the way, experimental results show that the improvement in solar energy harvesting based on pyro-electric effect can be obtained by means of optical focusing systems and absorbing coatings, as expected. Indeed, the surface power density on the pyro-electric crystal can be about 20 times, 120 times and 600 times greater than the one achievable by means of direct solar exposition if the plano-convex lens and the Fresnel lenses A and B are used, respectively. Moreover, the surface power density achievable by some of the above quoted optical systems focusing solar radiation is also greater than the one typically produced by halogen lamps, confirming that the performances of the proposed harvester are typically better during solar exposition than during halogen lamps exposition. By the way, the above quoted optical focusing lenses could require for full optimization tracking systems in order to be correctly aligned to the direct solar radiation (as occurs in many solar based energy generators), to concentrate it on the pyro-electric element. The random increases of voltage V_{CE} with respect to time, shown in **Figure 4.5(e)** and **Figure 4.5(f)**, can be probably due to two main reasons. The first one is related to the wind speed fluctuations experienced by the pyro-electric crystal. The second one is related to the fact that the temporal temperature variation is not spatially uniform on the pyro-electric crystal, contrary to other works in literature where the temperature can be assumed uniform on the material; indeed, the almost instantaneous voltage increases are most likely due to spatial gradient of the derivative of temperature with respect to time dT/dt, meaning that the voltage boosts can be due to the emerging electrical charges in different local spatial regions of the surface of the pyro-electric crystal covered by electrodes. Therefore, further configurations of the proposed harvester could be oriented to develop a control system able to move optical lens in order to focus solar radiation in different regions of pyro-electric element, so that a controlled spatial gradient of the derivative of temperature with respect to time dT/dt could be obtained and used to improve the efficiency of energy harvester.

In conclusion, in order to evaluate the performances of the proposed pyro-electric harvester, experimental trials have been carried out indoor and outdoor.

Experimental results show that the improvement in solar energy harvesting can be obtained by means of optical focusing systems allowing an enhancement of the surface power density on the pyro-electric crystal up to 600 times than the one achievable by means of direct solar exposition. Moreover, results confirm that the radiation absorbing material used as a coating of the pyro-electric crystal is able to improve the solar radiation absorption and, as a consequence, to increase the amplitude of temperature variation. Further configurations based on micro-lenses array are under development in our laboratory for integrating array of small micro-generators. The proposed energy harvester structures can be fabricated in 2D arrays allowing the devices to generate sizable amounts of electrical power for many applications. As example, in **Figure 4.4(b)**, an electrical circuit with three measurement channels for three different pyro-electric elements is shown.

4.2 Pyroelectric Inkjet printing and patterning

In the following section, the dispensing of separate polymer drops is achieved through a smart simplification of the nozzle-less pyro-EHD dispenser set-up (see Chapter 2), where a commercial halogen lamp illuminates the nanocomposite polymer CB layer described before, onto the LN crystals surface in order to induce the pyro-electric effect. Remarkably, high resolution is achieved in dispensing very high viscous liquids. Practical demonstrations in polymer **optical microlenses direct printing** using polydimethylsiloxane (PDMS) and poly(methyl methacrylate) (PMMA) are reported to validate the approach in handling high-viscous polymers for practical applications. Furthermore, the direct patterning of poly(lactic-co-glycolic acid) (PLGA) fibres onto hydrophobic substrates is demonstrated to represent a new way to a controllable thermal guided **self-sustaining micro - fabrication patterning** of polymer dots for cells studies.

Actually the manipulation of liquids and nano-objects is very attractive with important applications in biotechnology, photonics and micro-opto-electro-mechanical systems [35-38]. Even today, in micro and nanoscience, one of the most common difficulties consists in handling little droplets and controlling their movement for high resolution patterning and on demand printing [39,40]. Different nano-fluidic capabilities have been promoted for manipulating and dispensing polymers droplets but all of them are based on the use of multiple components such as channels, syringes or nozzles where the liquid of interest is transported and then released [41,42]. More recently electro-hydrodynamic (EHD) jetting [43] has been used for drawing thin jets of liquids from fine apertures [44]. A number of techniques have been proposed for the actuation of microfluidic droplets based on thermo-capillary effects [45], electrochemical gradients [46], photochemical effects [47] or optoelectronic-induced electro-kinetics [48]. In comparison with the conventional ones, actually the EHD ink-jet printing technique could guarantee high-resolution and on-demand patterning of functional materials in liquid form [39]. Regarding polymers handling, e.g. for the fabrication of optical components, EHD provides advantages in capabilities over conventional ink-jet approaches, but at the same time complex set-up including high-voltage generators, external electrodes and additional micro components are needed [49-51]. Recently an alternative technology, named pyro-EHD printing [21-23,55,56], has been discovered. The pyro-EHD allows to manipulate liquids in a no-contact mode and avoids the use of nozzles and external electrodes, thus overcoming some severe limitations of ink-jet printing, like for example nozzle-clogging [54]. Even if the pyro-EHD approach adds important advantages in processing functional materials by simply applying a temperature gradient onto a pyro-electric crystal, some limitations are still encountered in printing small volumes of polymers at high resolution [56]. In fact, some polymers like PDMS and PMMA that are commonly employed in different fields of technology from electronic to bio-microfluidics, are very difficult to dispense even by pyro-EHD. Here we propose an innovative method for the activation of the pyro-EHD inkjet system that allows the handling of very high viscous polymers and their direct printing. In the proposed configuration the pyro-electric effect is enhanced using the carbon black-based nanocomposite coating directly applied on the substrate (Lithium Niobate, LN). The pyro-EHD process is triggered efficiently by a halogen lamp, allowing high extraction force for PDMS and PMMA micro-lenses direct printing. The proposed apparatus introduces a further significant simplification when compared to the standard configuration of the 'pyro-EHD dispenser'[21] or the pyro-Thetered-Electrospinning [55,56], thus making the system versatile, more compact and low cost in order to produce integrated systems.

4.2.1 Description of the approaches and set up

The pyro-jetting effect is simply activated by a temperature gradient directly applied onto ferroelectric crystals [21]. The introduction of a coating based on carbon structures (carbon black , CB, multiwall carbon nanotubes, MWCNTs, graphene nanoparticles) on the top of LN or LT crystals can improve their radiation absorption [57-59] maximizing the resulting rise in temperature per unit of incident radiant power. In particular, the use of radiation absorbing coatings is determinant in the visible range (crystal are transparent from 320 to 5000 nm [60,61]) improving the efficiency and involving the whole visible and IR wavelengths, as demonstrated for energy harvesting in the previous section [62].

Despite of the various methods presented in literature [63-65], we focused on a pyro-EHD dispensing method [52] particularly attractive for the direct writing of materials from liquid drop and on the pyro-tethered-electrospinning [55] for the direct writing of ordered polymer fibres.

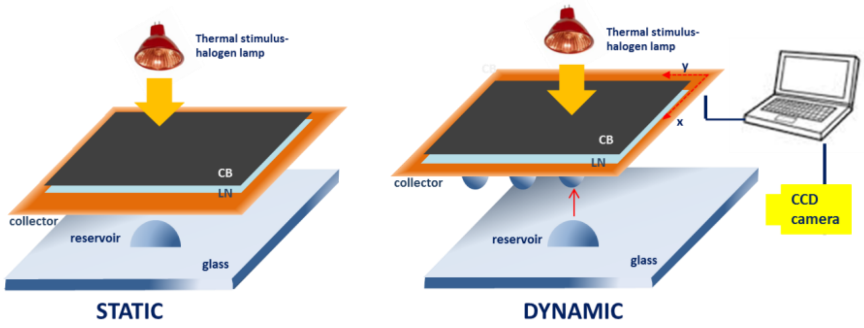

Figure 4.6: Pyro-EHD set-up in static and dynamic configuration, using the halogen lamp as the heating source.

In both cases, the system is simplified respect to the conventional ink-jet apparatus and consists of just two plates and a halogen Osram lamp used as heating source (focal length 32.0 mm; 12 V; 75 W) and operating on the CB coated crystals (**Figure 4.1(e)**). The set-up could be mounted in a static or dynamic configuration (**Figure 4.6**). The upper plate is constituted of a microscope coverslip, used as receiving substrate, placed on a three-axes translation stage, while the CB coated LN crystal drives the process. In the static configuration the collector is fixed in space, so that the reservoir drop can dispense multiple jetting in the same position increasing the dimension, in terms of volume and geometric characteristics, of the deposited droplet. On the other hand, one more interesting configuration is related to the continuous printing of separate droplets and this is possible just controlling the movement of the target substrate with high precision motorized positioners, as happens for the dynamic configuration as well as for the tethered one. The distance between the two plates was set on the scale of the hundreds of microns depending on the investigated base drop. The experienced thermal gradient using the configuration including a uniform CB membrane (2x2 cm^2) was enhanced (see [62]). Indeed it can be possible to realize patterned coating membrane so allowing the selective activation of the pyro-electric field. This configuration could increase the possibility of using the presented nozzle-less approach, especially in case of multiple starting drop, for the direct writing of arrays or matrices.

We start focusing on the activation of a single drop, as depicted in **Figure 4.6**. A video camera was used to monitor the printing process; the light coming from a collimated LED light source (Thorlabs M470L2) illuminates the cross section of the dispensing system, then it is collected by a 10X microscope objective and finally projected onto a CMOS camera (Motion Pro Y3-S1). Depending on the material of the reservoir drop, the dynamic and the jetting evolution could be different. In order to prove the use of the pyro-jetting method for direct printing of polymer materials and overcoming the viscosity limit of conventional ink-jet apparatus [54], in our experiments we used as base drops, Poly(methyl methacrylate) (PMMA) and Polydimethylsiloxane (PDMS) with different viscosities (PDMS: 3500 cps, PMMA: 560 cps). The manipulation of PDMS with the 'pyro-dispenser'[21] still suffer of some limitations. In fact, as shown in **Figure 4.7(a)**, the starting polymer drop assumes the shape of a liquid bridge that comes in contact with the target substrate and in this condition the dispensing of polymer drops is impracticable. On the contrary, by introducing a CB coating, the pyro-effect is enhanced so that the polymer drop deforms into a sharp and elongated Taylor cone from which tiny amount of polymer could be dispensed. Indeed, the use of a CB-layer reduces the recombination of the temporary surface charges and decreases the heat transfer from the crystal to the air, thus increasing the temperature gradient and improving the pyro-electric efficiency [21,55]. Furthermore, also the geometry of electric field lines plays a role in the process: they appear different in case of a confined heating area with respect to an extended one. The plots of electric field lines for localized heating and for uniform heating with a CB-layer are shown in **Figure 4.7(a)** and **Figure 4.7(b)**, respectively. It can be noted that when a CB-layer is used, the electric field is very uniform over a large area, thus affecting the geometry of the dispensing process. The thickness of the CB-layer is about 200 μm, this value is the result of an easy method of preparation and peeling for a uniform CB membrane, balanced with the radiation absorption valuable for the activation of the pyro-electric effect. The EHD force generated at the interface air-polymer can be represented by a stress tensor, with normal and tangential components. In **Figure 4.7(a)** under the influence of the pyro-electric field, the air-polymer interface moves dynamically while in case of **Figure 4.7(b)** it appears uniform and experiences a stress tensor with a single component. In this case, once the pyro-electric field is applied, the top polymer surface moves progressively upward with a spatially non uniform geometry; the elongated cone experiences a greater EHD force under a small distance, thus leading to the activation of the upper surface and to the formation of a thin polymer tip[41].

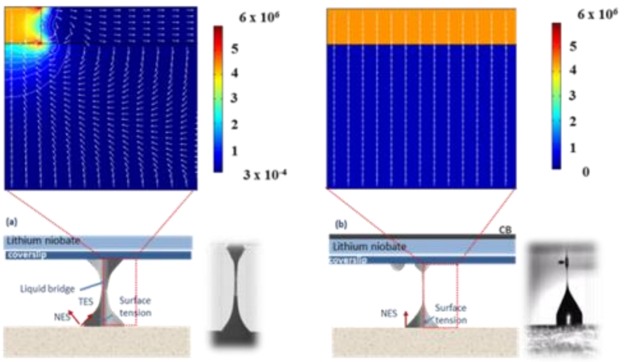

(a) **(b)**

Figure 4.7: Images of the PDMS-based reservoir drop deformation obtained by standard pyro-effect configuration (a) and innovative pyro-effect configuration employing a CB coating. In the case (a) the starting polymer drop assumes the shape of liquid bridge and experiences both normal and tangential components of the stress tensor while by introducing a CB coating (b) the pyro-effect is enhanced so that the polymer drop deforms into a sharp and elongated printing cone under the action of the tangential components.

4.2.2. Application in the direct printing of PMMA- and PDMS-based polymer microlenses

The pyro-electric effect was exploited through the CB-coated system for the fabrication on demand of single droplets characterized as lenses and micro-lenses arrays. PDMS and PMMA were chosen because of their good optical and mechanical properties. PDMS was used without any dilution, while the PMMA ink was prepared by dissolving 200 mg/mL of PMMA (Mw=120000 a.m.u) in pure NMethyl-2-pyrrolidone (NMP). We prepared the PDMS and PMMA inks in the same conditions tested for the pyro-EHD printing systems in order to better compare the results obtained [22,23]. In particular, referring to the PMMA ink, we chose the better condition of use found in our previous work [53] where various solutions at different mixing ratio of polymer and solvent have been tested. The receiving substrate was previously functionalized by means of a hydrophobic tetra-ethylorthosilicate/1H,1H,2H,2H-perfluorodecyl-triethoxysilane (TEOS/PFTEOS) film, spin-coated from a sol-gel solution in order to minimize the spreading of the dispensed droplets.

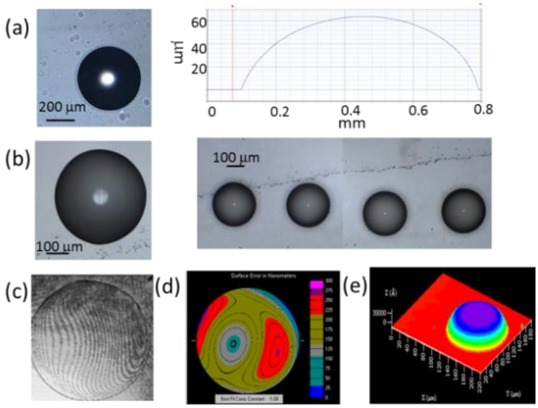

Figure 4.8: (a) Single PMMA microlens and corresponding profile, (b) PDMS microlens (left) and liner array of multiple lenses (right). Tilted interferometric fringe image (c), wavefront error (d) and 3-D image of the PMMA microlenses (e)

In **Figure 4.8(a)** we report the microscope image and the corresponding two dimensional profile (analyzed by DektakXT – Bruker system) of a single PMMA microlens obtained in static configuration. In Figure 8b we show examples of PDMS microstructures, specifically a single lens obtained in static configuration and an array of multiple lenses produced in dynamic mode. Controlling the experimental conditions and the starting droplet, we were able to produce PDMS lenses with different diameters ranging from 50 to 700 µm. By means of a collimated light beam passing through the lens, we made a scan along the optical axis (spatial resolution 8 microns) and reconstruct the three dimensional profile of the transmitted light intensity. Starting from the light propagation profile along the optical axis, we measured the focal length of the microstructures. As an example we report, in **Figure 4.9**, three samples of PDMS lenses with different dimensions (diameters: 260, 343, 615 mm).

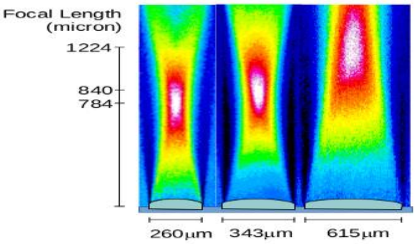

Figure 4.9: Focal lengths of PDMS microlenses with different diameters.

In this case, the focal length increases for larger lens diameters achieving the value of about 1200 μm for a diameter of 600 μm. The optical and geometrical characterizations were carried out through the interferometric technique. The resulting interference pattern contains quantitative informations derived from the shape of the fringes and the space between the fringes themselves. In case of the PMMA microlenses the complete optical and geometrical characterization was performed by means of a Mach-Zehnder system in confocal configuration. The single-path interferometer was preferred to the double-path one (e.g. Michelson and Twyman–Green interferometers) in order to minimize the measurement errors due to the used optical components [66]. A fringe analysis software was used to analyze the detected interference pattern (**Figure 4.8(c)**). The first step in the analysis was to plot data points along the fringes. The relative positions of each point provide the information about the microlens shape and the relative optical quality. The modelling process by means of the fringe analysis software uses Zernike polynomials to describe aberrations of lenses from an ideal spherical shape, which results in refraction errors [67,68]. The results obtained show that all the realized microlenses are aspheric and, in particular, they have a parabolic morphology. These geometrical features were confirmed by profilometric 3D analysis, as visible in **Figure 4.8(e)** where the geometrical properties of the lens are 128 μm diameter and height 12 μm, respectively. Due to the final aspheric shape of the lens, that consists in an ellipsoidal base (along xy- plane) and parabolic shape in the other direction (along z-axis), the evaluation of the focal length was very complex and it was possible to evaluate it in the range of 1.2 and 1.4 mm. In particular, according to the formula $Z^2 - 2RX + (K+1)X^2 = 0$, $K \sim -1$, where K is the conic constant in according with the parabolic shape and R is the radius of curvature.

4.2.3 Direct fabrication of ordered PLGA micro-beads via contemporary fibre deposition and breakup

As just mentioned, additional experiments have been performed to print ordered arrays of micro-beads directly from one polymer reservoir drop. We used the CB coating-based pyroelectric process described above to pattern PLGA polymer fibres onto specific functionalized substrates (FC).

When compared to PES (see Chapter 3) [55], the CB coating-based process shows high extraction force onto polymer drop, speeding up the direct writing and stretching the fiber diameter. Once deposited onto the FC, due to the interactions between viscoelastic thread and hydrophobic coated collector and favored by the heating stimulus mediated by the CB membrane, the fibre breakup takes place de-structuring the fibre [70,71]. **Figure 4.10** shows the schematic diagram of the procedure used.

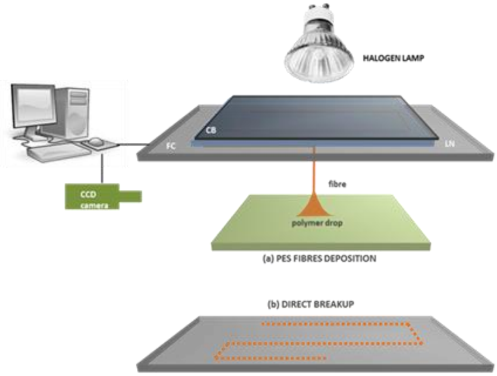

Figure 4.10: Schematic diagram of the process: the deposition by means of a carbon black membrane directly on the LN crystal, allows to contemporary deposit and fragment the polymer electro-spun fibre.

As revealed, for this preliminary study, Poly (lactic-co-glycolic acid) (PLGA-lactide:glycolide (75:25), Mw 40,000-75,000, Sigma-Aldrich) dissolved at a concentration of 25% wt/wt in dimethyl carbonate (DMC, Sigma Aldrich) was tested as reservoir ink with high responsivity. Different polymer coatings were tested: Polystyrene (PS, average Mw ~192,000, Sigma-Aldrich) at 60% wt/wt in Anisole (ReagentPlus®, 99%, Sigma-Aldrich), Poly(methyl methacrylate) (PMMA, average Mw ~996,000, Sigma Aldrich) at 30% wt/wt in Anisole, Poly(dimethylsiloxane) (PDMS, Sylgard 184 Silicone Elastomer Kit, 10:1 mix ratio, Dow Corning), Sigmacote® (siliconizing reagent for glass and other surfaces, Sigma-Aldrich) and Fluorolink® S10 - PFPE (perfluoropolyether alkoxy silane, Solvay Specialty Polymers). **Table 4.2** shows the typical surface free energy values for the aforementioned materials.

MATERIAL	**SURFACE FREE ENERGY (SFE) @ 20°C [mN/m]**
FLUOROSILANE	17.17
PDMS 1:1	19.8
SIGMACOTE	28.5
PMMA	41.1
PS	40.7

Table 4.2: Surface free energy values for the used coatings.

Their hydrophobic nature was first evaluated by contact angle measurements of a PLGA sessile droplet on a smooth homogeneous coated surface using static sessile drop method [69]. When a liquid droplet strikes a substrate, the edge of the drop can be characterized as hydrophilic (wetting) or hydrophobic (de-wetting) by the value of the angle θ formed between the tangent at the profile of the droplet and the surface where it has been deposited, angle measured at the point of contact of the droplet with the surface. The coating polymer solutions were prepared and spin coated on the glass slide according to the protocol proposed by the Producer. The PLGA contact angles were obtained by a mean of 3 measurements and the values reported in **Figure 4.11**.

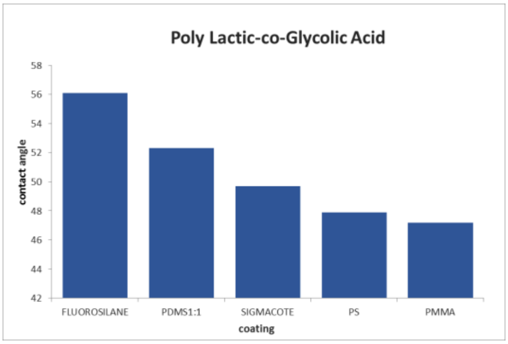

Figure 4.11: Contact angle values for PLGA onto different coatings

The measurements proved that the perfluoropolyether alkoxy silane (PFPE) layer gave the higher contact angle value for the PLGA droplet and so was chosen for the following investigations.

After fixing the experimental parameters (PLGA @25% in DMC onto PFPE coated glass), we observed the temporal evolution of a multi- geometry patterned fibre. To have a direct control/view on the dynamics of the breakup phenomenon, being the one described and highlighted in **Figure 4.10** a single step procedure, we had to deposit the initial polymer filament by classical PES method [55] and then follow the evolution from fibre towards dots, exploiting the heating provided by a conventional hot plate. In this way we were able to collect a time lapse describing the process evolution, whose representative frames are reported in **Figure 4.12**.

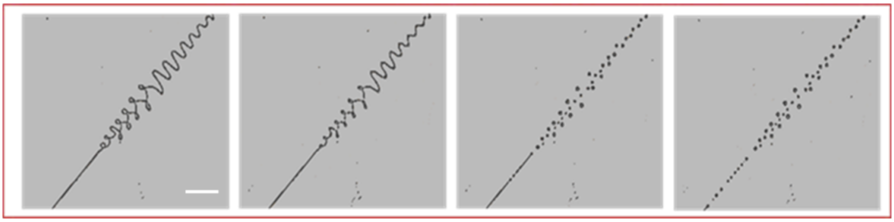

Figure 4.12: Extracted frames from the time lapse describing the temporal evolution from the original deposited PLGA fibre (on the left) to the one after the annealing process (on the right) (scale bar 100 μm)

Instability is caused by surface tension as it forces a liquid to assume a smaller surface area per unit mass which is the form of a sphere [72].

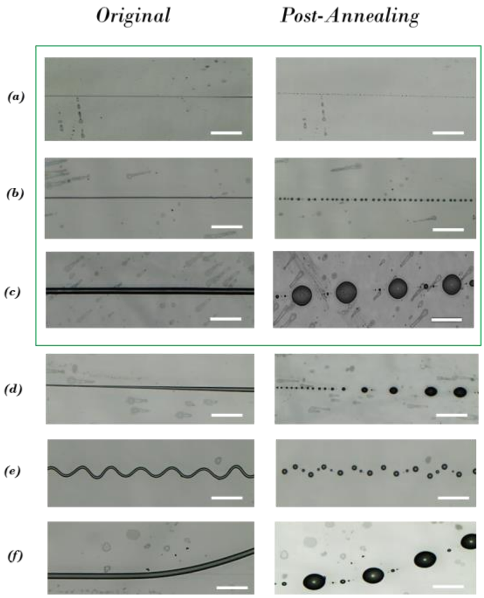

Figure 4.13: Thermal breakup for different geometries varying the thickness of the fibre (a-c) and the morphology (d-f). (scale bars 200 μm)

Figure 4.13 shows how the break-up effect works on different threads both in dimensions (**Figure 4.13(a-d)**) and shapes (**Figure 4.13(e-f)**). There are two principal things to point out: (1) the formation of bigger dots in the points corresponding to the 'corners' of the curved lines (see **Figure 4.13(e)**) and (2) the dots' dimensions and spacing linked to the original lines dimensions. The relation between initial filament diameter and both final spheres dimensions and dots' pitches were evaluated. As shown in **Figure 4.14(a),** the trend for the dots diameter with respect to the filaments dimension is linear: the bigger the thread the bigger the dots born from the beads-on-a-string evolution process thermally guided. Furthermore, it is interesting to note, in the graph in **Figure 4.14(b),** the *breakup wavelength* (dots pitch) as a function of the filament diameter. For the smaller wires, the tendency to re-aggregate of the filament-breakup derived dots, gives to the trend a decreasing path that ends as soon as the diameter grows (i.e. up to 7 microns for thread diameter: threshold limit), inhibiting the reassembly.

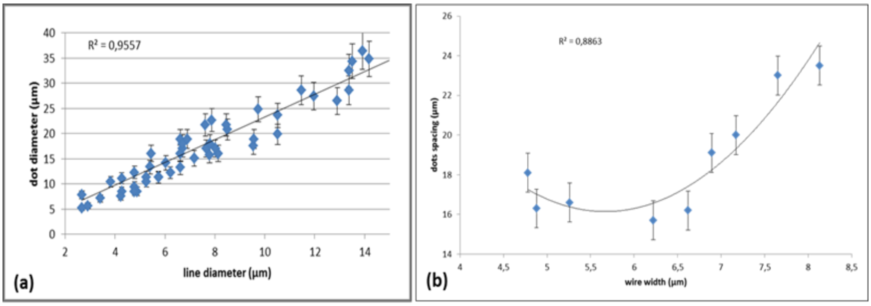

Figure 4.14: (a)Behavior of the dots diameters obtained after the break-up process as a function of the starting filament width. In (b) the break-up wavelength as a function of the filament diameter is shown.

The obtained 'dotted way', being the polymer tested biocompatible and biodegradable, can be used as alternative platform for cell patterning application, as demonstrated below.

For this purpose, we produced the dots pattern, originated from the electrospun fibre, directly during the deposition process (**Figure 4.10**). The cell adhesion on the dots patterned samples was evaluated *in vitro* using mouse embryonic fibroblast cells (NIH-3T3). Cells were grown in Petri dishes in Dulbecco's modified Eagle's medium (DMEM) containing 4.5 g/L D-glucose and supplemented with 10% FBS (fetal bovine serum), 100 units/mL penicillin, and 100 µg/mL streptomycin. Subsequently, they were harvested from the tissue culture flasks by incubation with a 0.05% trypsin–EDTA solution for 5 min. The cells were then centrifuged, re-suspended in a complete medium, and then seeded on eight LN crystal substrates at a density of 1×105 cells/mL, NIH 3T3 were then incubated in conventional 50 mm diameter Petri dishes at 37 °C and in humidified 5% CO2 atmosphere. The cell adhesion and spreading was observed over 24h under a standard inverted optical microscope(AxioVert, Carl Zeiss, Germany).

As shown in **Figure 4.15**, the hydrophobic nature of the substrate, leads to the positioning and attachment of the cells exclusively on the hydrophilic patterned dots. By the creation of these different-sized isolated islands, we are able to investigate cells behavior and morphology up to single cell studies as the microarchitecture of the surface has been found to play an important role in how cells respond to the surfaces.

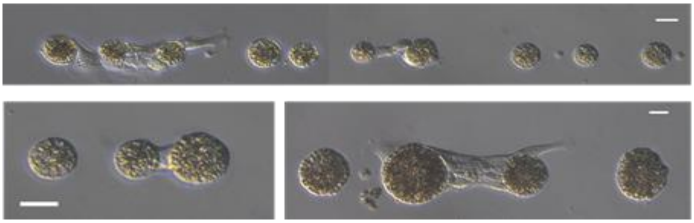

Figure 4.15: NIH 3T3 adhered on the biocompatible hydrophilic patterned polymer avoiding the PFPE layer (scale bars 20 μm)

4.2.4 Conclusions

In summary, the printing and the single-step patterning of separate polymer drops are achieved through a smart simplification of the nozzle-less pyro-EHD dispenser set-up, where a commercial halogen lamp illuminates the nanocomposite polymer CB layer onto the LN crystals surface in order to induce the pyro-electric effect. The improvement of properties and functionalities of the EHD printing process has been reported. Different experiments were conducted to prove the use of high viscous polymers (PDMS, PMMA, PLGA). It is shown that dispensed polymer drops can be adopted as microlenses. In fact, the presented results, supported by profilometric and interferometric analyses, demonstrate the feasibility to obtain optical microlenses through this innovative nozzle-free technique in the focal range of 1.2 and 1.4 mm and diameter from 70 to 700μm. On the other hand, the facile and single-step production of PLGA micro-arrays would be useful for micro-chemical reaction, DNA detection and bio-sensing as well as for cell patterning applications.

References

[1] S.R. Hunter, N.V. Lavrik, S. Mostafa, S. Rajic, P.G. Datskos, "Review of pyroelectric thermal energy harvesting and new MEMs based resonant energy conversion techniques.", *Proc. SPIE*; 83770D1-14, (2012)

[2] D. Lingam, A.R. Parikh, J. Huang, A. Jain, M. Minary-Jolandan, "Nano/microscale pyroelectric energy harvesting: challenges and opportunities." *Int. J. Smart Nano Mater.*; 10.1080/19475411.2013.872207, (2013)

[3] N. Tesla , " Pyromagneto-electric generator." *US Patent* 428,057, (1887)

[4] Y. Wang, B. Tang, S. Zhang. "Organic, cross-linking, and shape-stabilized solar thermal energy storage materials.", *Appl Energy*; **113**: 59-66, (2014)

[5] C.Y. Sue, N. Tsai."Human powered MEMS-based energy harvest devices." *Appl Energy*; **93**: 390-403, (2012)

[6] V. Srivastava, Y. Song, K. Bhatti, R.D. James. "The Direct Conversion of Heat to Electricity Using Multiferroic Alloys.", *Adv. En. Mat.*; **1**,97-104 (2011)

[7] C.X. Guo, G.H.Guai, C.M. Li. "Graphene Based Materials: Enhancing Solar Energy Harvesting", *Adv. En. Mat*,; **1**, 448-52, (2011)

[8] A. Cuadras, M. Gasulla, V. Ferrari. "Thermal energy harvesting through pyroelectricity", *Sens. Actuators, A*, **158**: 132-9,(2010)

[9] G. Sebald , E. Lefeuvre, D. Guyornar "Pyroelectric energy conversion: optimization principles", *IEEE Trans. Sonics Ultrason*, **55**, 538-51, (2008)

[10] R.B. Olsen, D.A. Bruno, J.M. Briscoe, E.W. Jacobs , "Pyroelectric conversion cycle of vinylidene fluoridetrifluoroethylene.", *J. Appl. Phys.,* **57**, 5036-42, (1985)

[11] M. Ikura , "Conversion of low-grade heat to electricity using pyroelectric copolymer", *Ferroelectrics,* ; **267**,403-8, (2002)

[12] Y. Yang , W. Guo, K.C. Pradel, G.Zhu, Y.Zhou, Y.Zhang, Y.Hu, L.Lin, Z.L.Wang," Pyroelectric Nanogenerators for Harvesting Thermoelectric Energy", *Nano Lett.*, **12**, 2833-8, (2012)

[13] C.R.Bowen, H.A.Kim, P.M.Weaver, S. Dunn. "Piezoelectric and ferroelectric materials and structures for energy harvesting applications", *Energy Environ. Sci.*,**7**, 25-44, (2014)

[14] F.Y. Lee, A. Navid, L. Pilon, "Pyroelectric waste heat energy harvesting using heat conduction", *Appl. Therm. Eng,* **37**, 30-37,(2012)

[15] J. Xie, X.P. Mane, C.W. Green, K.M. Mossi, K.K. Leang, "Performance of Thin Piezoelectric Materials for Pyroelectric Energy Harvesting", *J. Intell. Mater. Syst. Struct.* (2010); DOI: 10.1177/1045389X09352818.

[16] S.K.T. Ravindran, T. Huesgen, M. Kroener, P. Woias. "A self-sustaining micro thermomechanic-pyroelectric generator", *Appl. Phys. Lett.,* **99**, 104102, (2011)

[17] J. Lim (Samsung Electronics, CO.,LTD.), *US Patent* 2011/0169372, (2010)

[18] S. Kumar (UltraSolar Technology ,Inc.), *US Patent* 2011/0232734 A1, (2011)

[19] Q. Zhang, A. Agbossou, Z. Feng, M. Cosnier, "Solar micro energy harvesting with pyroelectric effect and wind flow", *Sens. Actuators, A* , **168**, 335-42, (2011)

[20] S. Grilli, S. Coppola, V. Vespini, F. Merola, A. Finizio, P. Ferraro, "3D lithography by rapid curing of the liquid instabilities at nanoscale", *Proc. Natl. Acad. Sci.*, **108**, 15106-11, (2011)

[21] P. Ferraro, S. Coppola, S. Grilli, M. Paturzo, V. Vespini, "Dispensing nano-pico droplets and liquid patterning by pyroelectrodynamic shooting", *Nat. Nanotechnol.*, **5,** 429-35,(2010)

[22] S. Coppola, V. Vespini, S. Grilli,P. Ferraro, "Self-assembling of multi-jets by pyro-electrohydrodynamic effect for high throughput liquid nanodrops transfer", *Lab Chip* , **11**, 3294-8, (2011)

[23] V. Vespini, S. Coppola, S. Grilli, M. Paturzo, P. Ferraro, "Pyroelectric Adaptive Nanodispenser (PYRANA) microrobot for liquid delivery on a target", *Lab Chip,* **11**, 3148-52, (2011)

[24] F. Merola,S. Grilli,S. Coppola, V. Vespini, S.De Nicola, P. Maddalena, M. Carfagna, P.Ferraro, "Reversible Fragmentation and Self-Assembling of Nematic Liquid Crystal Droplets on Functionalized Pyroelectric Substrates", *Adv. Funct. Mater,* **22**, 3267-72, (2012)

[25] E. Theocharous, R. Deshpande, A.C. Dillon, J. Lehman, "Evaluation of a pyroelectric detector with a carbon multiwalled nanotube black coating in the infrared", *Appl. Opt.*; **45,** 1093-7, (2006)

[26] J.H. Lehman, C. Engtrakul, T. Gennett, A.C. Dillon, "Single-wall carbon nanotube coating on a pyroelectric detector", *Appl.Opt.*,**44**, 483-8, (2005)

[27] Z. Lu, K. Zhao, X. Li, Ferroelectrics - Physical Effects, (Edts. M. Lallart), InTech, Rijeka, Croatia, Ch. 28, (2011)

[28] H. Xia, X. Zeng, J. Wang, J. Zhang, J. Xu, Y. Zhang, Q. Nie, "Optical absorption spectra of LiNbO3, Fe:LiNbO3, and Zn:Fe:LiNbO3 single crystals grown by Bridgman method", *Cryst. Res. Technol.*, **39**, 337-42, (2004)

[29] C.C. Ting, W.S. Chao, "Efficiency improvement of the DSSCs by building the carbon black as bridge in photoelectrode", *Appl Energy,* **87**,2500-5, (2010)

[30] R.W. Bergstrom, P.B. Russell, P. Hignett. "Wavelength dependence of the absorption of black carbon particles", *J.Atmos. Sci.*, **59**, 567-77, (2002)

[31] Z. Yin, J. Zhu,Q. He, X. Cao, C. Tan, H. Chen, Q.Yan, H. Zhang, "Graphene-Based Materials for Solar Cell Applications", *Adv. Energy Mater.,***4**, 1300574, (2014), DOI: 10.1002/aenm.201300574.

[32] X. Li, Y. Chen, Z. Cheng, L. Jiad, S. Mo, Z. Liu, "Ultrahigh specific surface area of graphene for eliminating subcooling of water", *Appl Energy*, **130**, 824-829, (2014)
http://dx.doi.org/10.1016/j.apenergy.2014.02.032

[33] M.I. BudykoI, "The effect of solar radiation variations on the climate of the Earth", *Tellus,* **21**,611-9, (1969)

[34] A. Mavropoulos , M. Cattani-Lorente, I. Krejci, C.B. Staudt, "Kinetics of light-cure bracket bonding", *Am. J. Orthod.*, **134**, 543-7, (2008)

[35] V. Taly, B.T. Kelly, A.D. Griffiths, "Droplets as Microreactors for High-Throughput Biology", *ChemBioChem*, **8**, 263-272,(2007).

[36] T.M. Squires, S.R. Quake, "Microfluidics: Fluid physics at the nanoliter scale", *Rev. Mod.Phys*. **77,** 977 (2005).

[37] B. Y. Ahn, E. B. Duoss, M. J. Motala, X. Y. Guo, S. I. Park, Y. J. Xiong, J. Yoon, R. G. Nuzzo, J. A. Rogers, J. A. Lewis, "Omnidirectional Printing of Flexible, Stretchable, and Spanning Silver Microelectrodes ", *Science* , **323**, 1590, (2009).

[38] J.-U. Park, M. Hardy, S. J. Kang, K. Barton, K. Adair, D. K. Mukhopadhyay, C. Y. Lee, M. S. Strano, A. G. Alleyne, J. G. Georgiadis, P. M. Ferreira, and J. A. Rogers, "High-resolution electrohydrodynamic jet printing.", *Nature Mater.*, **6**, 782-9, (2007).

[39] J.-U Park, S.Lee, S. Unarunotai , Y. Sun, S. Dunham, T. Song, P. M. Ferreira, A.G. Alleyene, U. Paik, J. A. Rogers, "Liquid Jets for High-Resolution Printing of Charge", *Nano Lett.*, **10**, 584-591, (2010).

[40] F. D. Prasetyo, H.T. Yudistira, V. D. Nguyen, D. Byun, "Ag dot morphologies printed using electrohydrodynamic (EHD) jet printing based on a drop-on-demand (DOD) operation", *J. Micromech. Microeng.* **23**, 095028 (2013).

[41] B. de Heij, M. Daub, O. Gutmann, R. Niekrawietz, H. Sandmaier, R. Zengerle, "Highly parallel dispensing of chemical and biological reagent", *Anal. Bioanal. Chem.* 378, 119-22 (2004).

[42] T. Ondarçuhu, J. Arcamone, A. Fang, H. Durou, E. Dujardin, G. Rius, F. Pérez-Murano, "Controlled deposition of nanodroplets on a surface by liquid nanodispensing: Application to the study of the evaporation of femtoliter sessile droplets" *Eur. Phys. J. Special Topics* **166**, 15-20, (2009).

[43] L.T. Cherney, "Structure of Taylor cone-jets: limit of low flow rates", *J. Fluid Mech.*, **378**, 167, (1999)

[44] R. T. Collins, J. J. Jones, M. T. Harris, O. A. Basaran, “Electrohydrodynamic tip streaming and emission of charged drops from liquid cones”, *Nature Phys*. **4**, 149-154, (2008).

[45] M. A. Burns, C. H. Mastrangelo, T. S. Sammarco, F. P. Man, J. R. Webster, B. N. Johnsons, B. Foerster, D. Jones, Y. Fields, A. R. Kaiser, and D. T. Burke, “Microfabricated structures for integrated DNA analysis.”, *Proc. Natl. Acad. Sci.*, **93**, 5556-5561,(1996)

[46] B. S. Gallardo, V. K. Gupta, F. D. Eagerton, L. I. Jong, V. S. Craig, R. R. Shah, N. L. Abbott, “Electrochemical principles for active control of liquids on submillimeter scales”, *Science* , **283**, 57-60, (1999).

[47] K. Ichimura, S.-K. Oh, and M. Nakagawa, “Light-driven motion of liquids on a photoresponsive surface”, *Science* ,**288**, 1624-1626 (2000).

[48] P. Y. Chiou, A. T. Ohta, M. C. Wu, “Massively parallel manipulation of single cells and microparticles using optical images”,*Nature* ,**436**, 370-372, (2005).

[49] F.F. Wang, F. Fei, L.Q. Liu, LQ, H.B. Yu, P. Yu, Y.C. Wang, G.B. Lee, W. Jung, “Exploring pulse-voltage-triggered optically induced electrohydrodynamic instability for femtolitre droplet generation “, *Appl. Phys. Lett*. **104**, 264103, (2014).

[50] C.H. Ru, J. Luo, S.R. Xie, Y. Sun, “A review of non-contact micro- and nano-printing technologies”, *J. Micromech. Microeng.*, **24**, 053001 (2014).

[51] Y. Kim, S. Jang and J.H. Oh., “High-resolution electrohydrodynamic printing of silver nanoparticle ink via commercial hypodermic needles “*Appl. Phys. Lett.*, **106**, 014103 (2015).

[52] I.A. Grimaldi, S. Coppola, F. Loffredo, F. Villani, C. Minarini, V. Vespini, L. Miccio, S. Grilli, P. Ferraro, “Printing of polymer microlenses by a pyroelectrohydrodynamic dispensing approach”,*Opt. Lett.* , **37**, 2460 (2012).

[53] I. A Grimaldi, S. Coppola, F. Loffredo, F. Villani, G. Nenna, C. Minarini, V. Vespini, L. Miccio, S. Grilli, P. Ferraro,” Graded-size microlens array by the pyro-electrohydrodynamic continuous printing method”, *Applied Optics* , **52**, 7699 (2013).

[54] D.G. Yu, C. Branford-White, K. White, N. P. Chatterton, L. M. Zhu, L. Y. Huang, B. Wang, “A modified coaxial electrospinning for preparing fibers from a high concentration polymer solution”,*eXPRESS Polymer Letters*, **5**, 732 -741(2011).

[55] S. Coppola, V. Vespini, G. Nasti , O. Gennari, S. Grilli, M. Ventre, M. Iannone, P.A. Netti, P. Ferraro, ”Tethered Pyro-Electrohydrodynamic Spinning for Patterning Well-Ordered Structures at Micro- and Nanoscale”, *Chem. Mater.,* **26**, 3357-3360, (2014).

[56] R. Vecchione, S. Coppola, E. Esposito, C. Casale, V. Vespini, S. Grilli, P. Ferraro, P.A. Netti, “Electro-Drawn Drug-Loaded Biodegradable Polymer Microneedles as a Viable Route to Hypodermic Injection”,*Adv. Funct. Mater*., **24**, 3515-3523 (2014).

[57] E. Theocharous, R. Deshpande, A. C. Dillon, J. Lehman, “Evaluation of a pyroelectric detector with a carbon multiwalled nanotube black coating in the infrared”,*Appl. Opt*., **45**, 1093-1097 (2006).

[58] J.H. Lehman, C. Engtrakul, T. Gennett, A. C. Dillon, “Single-wall carbon nanotube coating on a pyroelectric detector”, *Appl.Opt*., **44**, 483-488, (2005).

[59] E. Theocharous, C. Engtrakul, A. C. Dillon, and J. Lehman, “Infrared responsivity of a pyroelectric detector with a single-wall carbon nanotube coating”, *Appl.Opt*, **47**, 3999-4003 (2008).

[60] Z. Lu, K. Zhao and X. Li, “Ferroelectrics - Physical Effects”, (Edts. M. Lallart), InTech, Rijeka, Croatia, Ch. 28, (2011)

[61] H. Xia, X. Zeng, J. Wang, J. Zhang, J. Xu, Y. Zhang, Q. Nie, “Optical absorption spectra of LiNbO3, Fe:LiNbO3, and Zn:Fe:LiNbO3 single crystals grown by Bridgman method”, *Cryst. Res. Technol*., **39**, 337 (2004).

[62] L. Battista, L. Mecozzi, S. Coppola, V. Vespini, S. Grilli, P. Ferraro, “Graphene and carbon black nano-composite polymer absorbers for a pyro-electric solar energy harvesting device based on LiNbO3 crystals”, *Appl. Energy* , **136**, 357, (2014).

[63] R. Ahmed, T.B. Jones, “Optimized liquid DEP droplet dispensing”, *J.Micromech. Microeng*., **17**,1052, (2007).

[64] A. Casner, J.-P. Delville, “Laser-induced hydrodynamic instability of fluid interfaces”, *Phys. Rev. Lett.*, **90**,144503, (2003).

[65] L.T. Cherney, “Structure of Taylor cone-jets: limit of low flow rates”, *J.Fluid Mech.*, **378**,167 (1999).

[66] H.M. Tian, J. Y. Shao, Y.C. Ding, X.M. Li, H.Z. Liu,” Numerical characterization of electrohydrodynamic micro- or nanopatterning processes based on a phase-field formulation of liquid dielectrophoresis”,*Langmuir*, **29**, 4703-4714, (2014).

[67] I.A. Grimaldi, A. De Girolamo Del Mauro, F. Loffredo, G. Nenna, F. Villani, C. Minarini, “Microlens array manufactured by inkjet printing: study of the effects of the solvent and the polymer concentration on the microstructure shape”, *Proceedings of SPIE*, no. 808244 (2011).

[68] M. S. Kim, T. Scharf, H. P. Herzig,” Small-size microlens characterization by multiwavelength high-resolution interference microscopy”, *Opt. Express* , **18**, 14319-14329, (2010).

[69] R. Förch, H. Schönherr, and A. T. A. Jenkins (Ed.), “Surface Design: Applications in Bioscience and Nanotechnology, Appendix C - Contact Angle Goniometry”, Wiley-VCH Verlag GmbH & Co. KGaA, Weinheim, 2009

[70] Y.Huang , Y. Duan , Y. Ding , N.Bu , Y.Pan, N.Lu , Z.Yin, “Versatile, kinetically controlled, high precision electrohydrodynamic writing of micro/nanofibers, *Sci.Rep.*, **4**, 5949 (2014).

[71] L. Kondic, J.A. Diez, P.D. Rack, Y.Guan, J.D. Fowlkes, “Nanoparticle assembly via the dewetting of patterned thin metal lines: understanding the instability mechanisms.”, Phys Rev E Stat Nonlin Soft Matter Phys. , 79, 026302 (2009)

[72] H. Fong, I. Chun, D.H. Reneker, “Beaded nanofibers formed during electrospinning.”, *Polymer*, **40**, 4585, (1999)

Chapter 5

LiNbO$_3$ as biocompatible platform for cellular proliferation

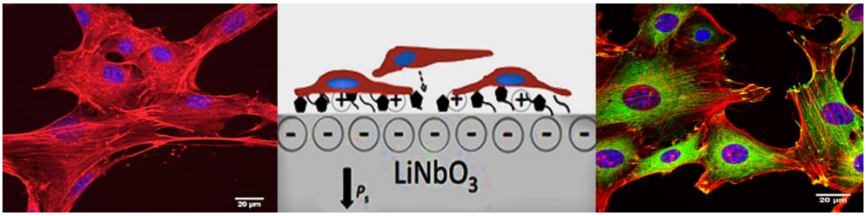

In this chapter the polar nature of Lithium Niobate crystals was exploited to investigate cellular behavior. The influence of the face-polarity of the ‘naked’ crystal on cells adhesion and proliferation was analyzed demonstrating the finding of a new biocompatible platform.

The interaction of cells with non-biological materials is crucial to control cell function, growth, and movement, both *in vitro* and *in vivo* environments, thus providing the criteria for designing those biocompatible materials used for engineering bio-hybrid organs [1-6]. Recently, a wide variety of materials have been studied demonstrating how the physicochemical properties of the material influence the protein adsorption and therefore the cell response. Some of these works focus their attention on the interaction of cells with nanoparticles [9-11], while others investigate the effect of super hydrophobicity [12,13] or the surface potential in specific substrates[14], just to cite some. In particular, in the last decades, there have been many developments in the field of the so-called ‘bioceramics’, and Baxter and co-workers published an excellent review on this topic[15]. The electric potentials, which occur in bones under mechanical loading, are explained partially in terms of the piezoelectric properties of the collagen [16]. These potentials have been linked to the mechanical adaptation of bones in response to loading [17,18], thus suggesting that the addition of an electrically active component to an implant material may improve healing and adaptation of the surrounding tissue. Consequently, great interest has grown for the bio-inspired research to understand if and how polarization of piezoelectric ceramics can improve the response of cells that synthesize bones (osteoblasts) to artificial implants and grafts [19-22]. However, new biocompatible platforms are always being desired in order to understand how materials with different surface properties may influence and control the cellular response, thus leading to the development of principles that can be used for engineering useful implantable devices and tissue-engineered constructs. In this framework, ferroelectric crystals may have a great potential, thanks to their unique polarization effect, with a relatively high spontaneous polarization that can be switched by an external electric field, and thanks to the inherent ability to sustain a charged surface under a variety of environments [23]. In particular, LN, with a value of ~71 $\mu C/cm^2$, has one of the largest polarization magnitudes known at room temperature, and easily reversible for modulating the surface charge polarity (see Chapter 2). LN, as just explained in the previous chapters, is well known in the field of electro-optics but its influence on living cells has been neglected. Some works have been published in literature dealing with the interaction and assembling of molecules and particles with the modified surface of ferroelectric thin films or crystals [24- 27]. However, to the best of our knowledge, only very recently, the biocompatibility of LN and lithium tantalate (LT) has been investigated for the first time [28]. and a couple of works has been presented on the response of cells cultured onto the surface of ferroelectric bulk crystals. Cristophis et al. studied the interaction of osteoblast cells with the surface of LN crystals, concluding that the surface charge promotes the cell attachment, proliferation and function, but regardless of the polarization sign [29]. Moreover, they present controversial results on cell proliferation, compared to previous studies performed onto bio-ceramics [15]. Carville et al. investigated the adhesion of fibroblast cells onto periodically poled LT crystals functionalized by a protein-based coating.[30] They concluded that cells tend to orient their nucleus avoiding the positions of high field gradients, but without any evident influence of the polarization sign onto the cell adhesion. In this poor framework, it is clear that the matter is at a very preliminary and controversial stage. In this chapter, we investigate how the spontaneous polarization of ferroelectric lithium niobate influences the adhesion properties of fibroblast cells (NIH-3T3 mouse embryonic fibroblast cells). In particular, the interaction of such cells with the surface of *c*-cut polished crystals of LN[3] is studied not only by observing the proliferation of the cells, but by focusing the attention, for the first time, on the effects of the polarization sign on the cytoskeleton and focal adhesions organization which, in turn, regulate a wide variety of cell functions such as cell migration and fate.

---

[3] In this work we used c-cut LN crystal samples 500μm thick and (2 ×2) cm^2 large, cut out from single domain wafers 3-inch in diameter and polished optically on both faces (purchased from Crystal TechnologY, Inc)

5.1 Assay procedures and results

The cell adhesion on the LN crystal samples was evaluated *in vitro* using mouse embryonic fibroblast cells (NIH-3T3). Cells were grown in Petri dishes in Dulbecco's modified Eagle's medium (DMEM) containing 4.5 g/L D-glucose and supplemented with 10% FBS (fetal bovine serum), 100 units/mL penicillin, and 100 μg/mL streptomycin. Subsequently, they were harvested from the tissue culture flasks by incubation with a 0.05% trypsin–EDTA solution for 5 min. The cells were then centrifuged, re-suspended in a complete medium, and then seeded on eight LN crystal substrates at a density of 1×10^5 cells/mL, NIH 3T3 were then incubated in conventional 50 mm diameter Petri dishes at 37 °C and in humidified 5% CO_2 atmosphere. Half of the substrates exposed the *c*- face while the other exposed the *c*+ face. The cell adhesion and spreading was observed over 24h under a standard inverted optical microscope (AxioVert, Carl Zeiss, Germany). To study the interaction of these cells with the surface of the c-cut polished crystals of LN, we performed the experiments described below. The number of replicates for each experiment was adjusted according to the variance obtained. In graphs, all data were presented as means ± standard deviation and evaluated for difference by Student's *t*-Test. Differences were considered significant when $p < 0.05$.

5.1.1 Biocompatibility assay to study cell viability and proliferation

The biocompatibility of LN was tested quantitatively by using a conventional live/dead viability/cytotoxicity assay kit (Molecular Probes Invitrogen). The cells were seeded on three kinds of substrates, LN (*c*-), LN (*c*+), and sterile glass, which was used as a control (Delchimica Scientific Glassware)[32] and were incubated into Petri dishes for 24h and for 48h. After incubation, 1 mL of the combined live/dead cell staining solution (2 μM calcein AM and 4 μM EthD-1 in D-PBS) was added to the dish and incubated for 45 min at room temperature. The kit contains calcein-AM, that stains live cells as green, and the ethidium homodimer that stains the dead cells as red. Samples were then observed under a conventional fluorescence upright microscope (Axio Imager, Carl Zeiss, Germany) at different time intervals , in order to have a first view of their adhesion and proliferation onto the surface of LN crystals free of functionalization. **Figure 5.1** reports the typical bright field images recorded over the 24h.

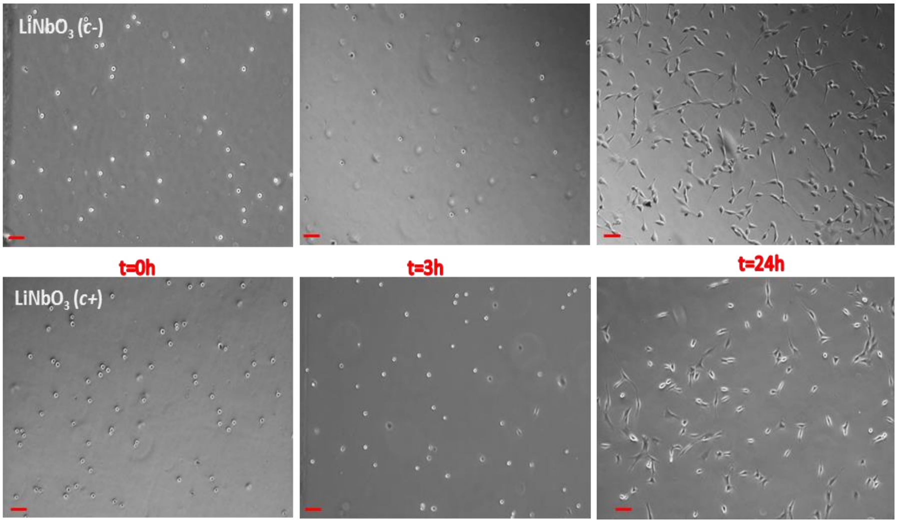

Figure 5.1: Typical bright field images of the cells seeded on *c*+ and *c*- free of functionalization and at the same time intervals (scale bar 100µm).

Cell spreading and adhesion appear similar on the two kinds of substrates, demonstrating the biocompatibility of the LN crystals in first approximation. A more accurate evaluation of this biocompatibility was performed by the live/dead assay described previously, and **Figure 5.2** shows the resulting fluorescence images.

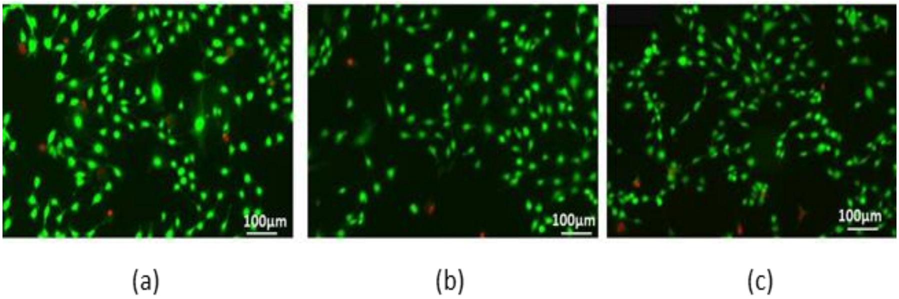

Figure 5.2: Typical fluorescence images of the cells seeded on (a) c-, (b) c+ and (c) glass, treated by the live/dead assay kit after 24h incubation.

The microscope observations showed a slightly, although not statistically significant, higher mortality for the cells seeded onto c+, compared with c- and glass. The cells were then harvested by incubation with a 0.05% trypsin–EDTA solution for 5 min and were counted by a conventional Burker's chamber and **Figure 5.3** shows the proliferation rates.

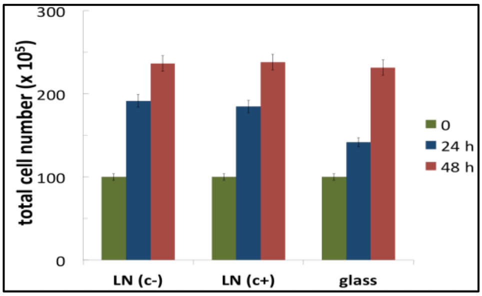

Figure 5.3: Cell growth onto the three different substrates. Data are not statistically significant (*t*-test, $p > 0.1$).

Figure 5.4 shows the distributions of the live/dead cells over the different substrates after 24h and 48h incubation. The mean values for each substrate were evaluated over three biological replicates.

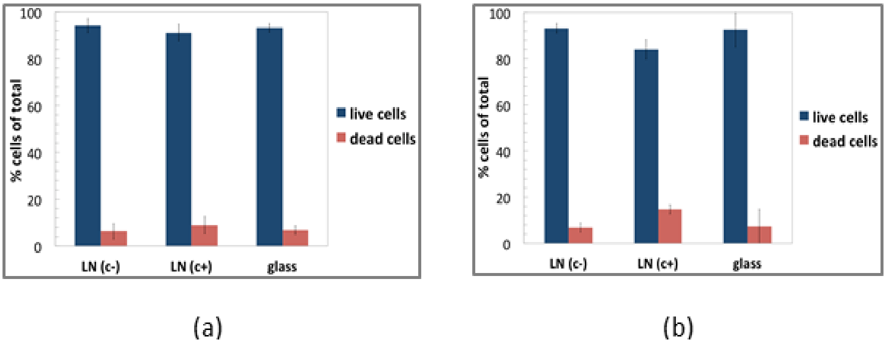

(a) (b)

Figure 5.4: Distribution of the number of live/dead cells over the three substrates (glass, c-, c+) after (a) 24h and (b) 48h incubation. The mean values were evaluated over three replicates of the experiment. Data are not statistically significant (t- test, $p > 0.1$).

These results demonstrate that the surface of the LN crystals can be considered definitely biocompatible with negligible differences in cell mortality between c- and c+.

5.1.2 Immunofluorescence analysis to study the morphology of actin filaments and focal adhesions

The cells were seeded on *c-*, *c+* and glass as control and incubated for 48h. After incubation, the medium was aspirated and the samples were rinsed with phosphate buffered saline (PBS) solution and fixed in 4% paraformaldehyde in PBS (pH 7.4) for 10 minutes at room temperature. The samples were then washed in PBS and permeabilized with 0.1% Triton X-100 in PBS for 5 min and blocking solution (1% BSA in PBS) for 30 min. The nuclei were stained with blue fluorescent Hoechst 33342 dye, trihydrochloride, trihydrate (Molecular Probes Invitrogen) in order to obtain a final concentration of 5 µg/mL, and the actin was stained with the tetramethylrhodamine (TRITC)-conjugated phalloidin for revealing the cytoskeleton network. Fluorescent phalloidin is widely used in the study of actin networks in biology. Supplementary immunostaining with antivinculin antibody was carried out in order to visualize further the actin-based cytoskeleton in the cell-cell and cell-substrate junctions.[32,33] The cells were incubated first in a primary antivinculin antibody (Biorbyt Limited, UK) diluted in blocking solution for 1 h, and then in a secondary donkey antirabbit DyLight 488 (Thermo Scientific, USA) at 1:200 dilution in blocking buffer solution for 45 min. For double labelling, the TRITC-conjugated phalloidin was incubated simultaneously with the secondary antibody. The crystals were washed three times in PBS between each antibody treatment. After permeabilization and staining, the samples were rinsed for 5 min three times in PBS. Fluorescence micrographs were acquired by an inverted laser scanning confocal microscope (Zeiss LSM 700), equipped with a 63× (1.4 NA) oil immersion objective. **Figure 5.5** shows the typical fluorescence images. The open source image processing program ImageJ, developed at the National Institute of Health (NIH), was used to analyze the images.

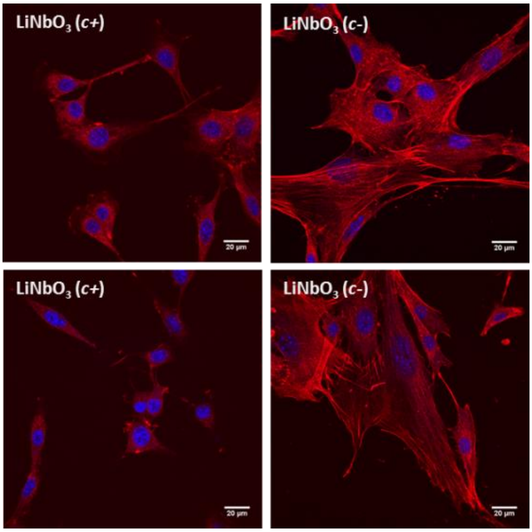

Figure 5.5: Confocal microscope images of cells seeded on c+ and c- after 1 day of culture, with nuclei and actin stained by DAPI (blue) and TRITC (red)-conjugated phalloidin, respectively.

The fluorescence images showed a non-negligible difference in the morphology of the actin filaments between the cells adhered on *c*- and on *c*+, evidencing two classes of cells. The cells adhered on *c*+ showed a round-like morphology with a few irregular protrusions and marked decrease in actin stress fibres. Conversely, the cells grown on *c*- exhibited a more elongated shape, with large spreading and more prominent stress fibres. The fibroblasts grown on *c*+ had poorly aligned stress fibres visible by fluorescence microscopy. In case of negative polarity (*c*-), such actin fibres were a nearly universal feature of these cells. The less developed stress fibres observed on *c*+ was not an indication of toxicity, considering the results of the viability test reported previously. Moreover, the poor alignment of the stress fibres on *c*+ was more evident on more isolated cells. **Figure 5.6** shows the typical case of confluent cells on *c*+, where the cells that made cell-cell contact frequently became elongated and developed stress fibres.

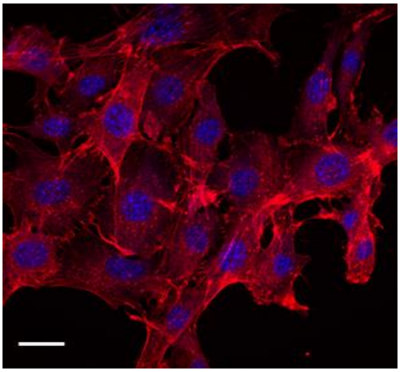

Figure 5.6: Confocal microscope image of confluent cells seeded on c+ after incubation for 24h, with nuclei and actin stained with DAPI and TRITC-conjugated phalloidin. (scale bar 20μm).

The more isolated cells in **Figure 5.5** show amorphous actin distribution with few stress fibres. Comparable cells on the same surface polarity that had made intercellular contact (see **Figure 5.6**)show the development of more stress fibres. Multiple observations were carried out on different regions of the samples and the ImageJ software was used for counting the cells belonging to the two classes of cell shape. **Figure 5.7** shows quantitatively the dependence of the cell shape on the polarity of the LN surface.

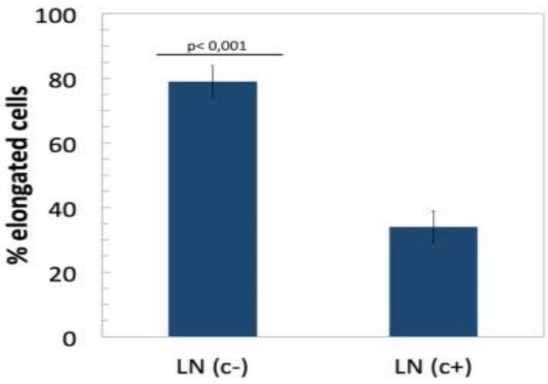

Figure 5.7: Distribution of the number of cells with more elongated shape and aligned stress fibres. Statistical significance was evaluated by Student's t-test, $p < 0.001$

Around 80% of the cells grown on *c-* showed more elongated shape with well aligned stress fibres. The examination of the focal adhesion formation on *c+* and *c-* showed a significant different morphology. After 24h plating, the focal adhesions formed on *c-* were much larger than those formed on *c+*, as shown clearly in **Figure 5.8**.

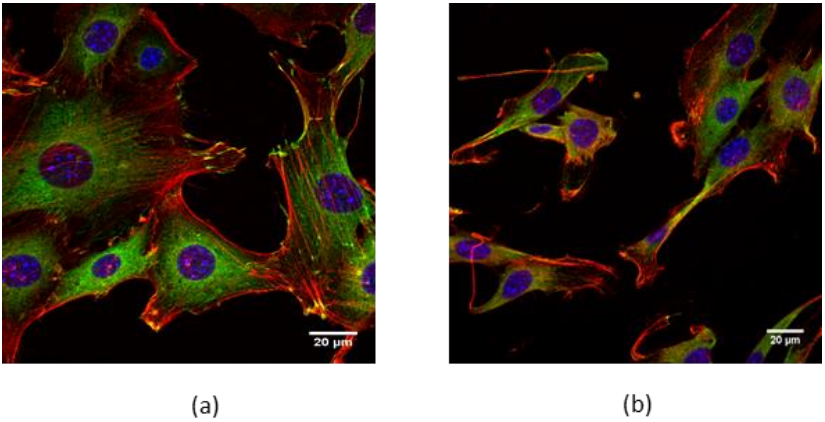

(a)

(b)

Figure 5.8: Confocal microscope images of cells plated (a) on c- and (b) on c+ face after 24h plating, with nuclei, actin and vinculin stained with DAPI, TRITC-conjugated phalloidin and DyLight488 vinculin, respectively.

The focal adhesions in cells plated on *c-* appeared elongated and oriented along the major cell axis, co-aligned with the stress fibres. Conversely, in case of *c+*, the cells formed smaller and radially oriented focal adhesions with low aspect ratios.

5.1.3 Cell migration assay

A well-established *in vitro* scratch assay, proposed by Liang et al. **[34]**, was used here for evaluating cell migration. This test is based on the observation that, upon creation of an artificial gap into a confluent cell monolayer, the cells on the edges of the gap move toward the open region to close the scratch until new cell–cell contacts are established again. It is reported that the cells initiate protrusion, migrate and finally close the wound. Therefore, this assay evaluates the cell migration by estimating the speed of scratch healing, depending on the substrate.**[35]** The cells were seeded on *c*-, *c*+ and glass slide as control, with a density of 1×10^5 cells and incubated at 37°C in 5% CO_2 atmosphere for 24h, allowing the cells to adhere and grow till reaching ~70-80% confluence as a monolayer. The cell monolayer was scraped after 24h along a straight line, by using the plastic tip of a P200 pipet, to reduce as much as possible the damage to cells and substrate. Care has been taken in creating scratches of approximately similar size for each substrate to minimize any possible variation caused by the difference in the width of the scratches. The samples were washed twice in 1 mL growth medium to remove debris and to smooth the scratch edges. The growth medium was replaced and the dishes were placed back into the culture incubator. The samples were taken out of the incubator every two hours for observing the scratch under an inverted microscope. The width of the scratch was measured as a function of time to determine the migration speed. **Figure 5.9** shows the typical bright field images of the scratch created onto *c*-, *c*+ and glass slide as control, at equal time intervals.

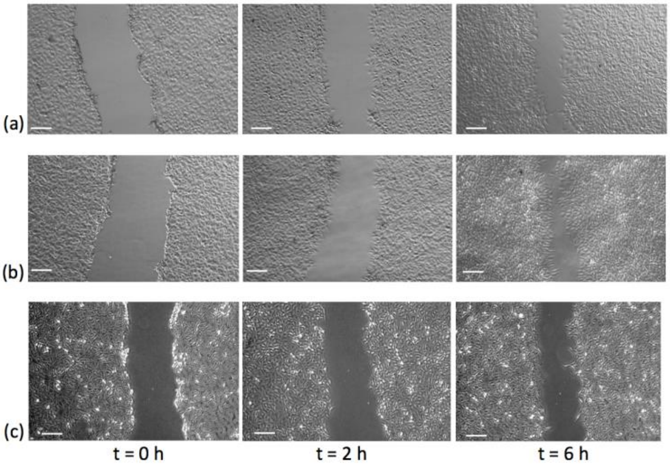

Figure 5.9: Typical optical microscope images of the scratch evolution over 6h for (a) c-, (b) c+ and (c) glass slide as control (scale bar 100µm)

About 10 readings of the scratch width were considered for each sample at each observation time, and the mean values were calculated over three replicates of the experiments. **Figure 5.10** shows the evolution of the scratch healing for the three substrates.

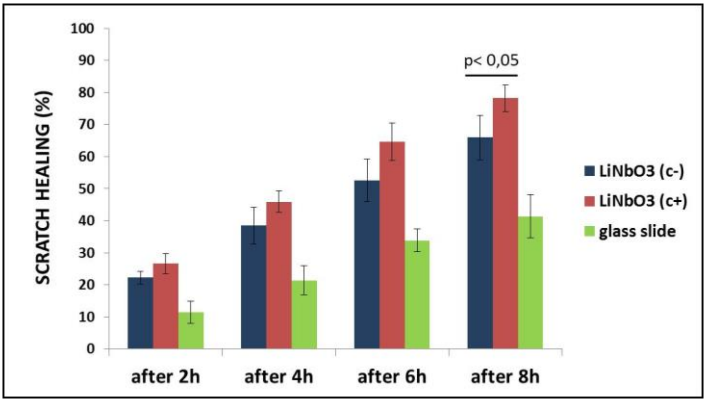

Figure 5.10: Percentage of scratch healing for each substrate. The mean values were calculated over three replicates of the experiments. Statistical significance was evaluated by Student's t-test, $p < 0.01$.

The cell migration appeared clearly different for each substrate with a faster scratch healing in case of the *c*+ face. The cell layer advanced basically by spreading and translocation of existing cells. This is further indicated by the decrease in cell density as the layer advanced toward the wound and the increase in mean cell area at the wound edge. The increase in cell area appeared significantly (only at 8h) faster on *c*+, with about 80% healing, compared to the 65% reached on *c*-. Lamellipodial protrusions are also known to guide cell migration.**[36]** During collective migration, cells at the wound edge and within the cell layer all actively migrate with lamellipodial protrusions extending mostly beneath adjacent cells, in case of the inner cells, and toward the wound closure in case of the edge cells. The cell protrusions in the closure region are prominent in case of *c*+ (see **Figure 5.9**), in agreement with the faster wound healing exhibited by the measurements. The slowest scratch-healing rate was obtained in case of the glass slide, with about 40% healing at the last point. These results demonstrate that the positive polarity of the substrate increases significantly the migration speed of the cells.

5.2 Discussion and conclusion

An early review of Davies [37] studied the importance of surface charges on cell behaviour at the biomaterial interface and demonstrated that surface charges have a profound effect on biological responses. It was concluded that the surface charges affect the adsorption of proteins onto the material surface and subsequently influence the cell morphology and migration. Those conclusions were based on studies of cells cultured on charged polymer surfaces. This work, instead, studies the *in vitro* response of fibroblast cells to the highest polarization magnitude of *c*-cut LN crystals (*Ps*=78 µC/cm2), thus paving the way to an innovative platform for bioengineering applications. First of all, the biocompatibility of these crystals was assessed by standard viability assays. IUPAC (International Union of Pure and Applied Chemistry) defines biocompatibility as the “ability to be in contact with a living system without producing an adverse effect”.[38] The results of the viability assays show that the LN crystals exhibit a biocompatible surface for the fibroblast cells. To the best of our knowledge, the cell interaction with the surface of these ferroelectric crystals has been explored poorly with only a couple of works presented in literature very recently.[39,40] Christophis et al.,[39] studied the adhesion of fibroblast cells onto polarized ferroelectric samples functionalized by a layer of fibronectin. They observed that the cells reoriented the position of their nuclei avoiding the positions of high field gradients, without any additional observation about the morphology of the cells. Carville et al.[40] investigated the promotion of osteoblast adhesion and mineralization onto the surface of LN crystals, concluding that only the presence of charge had a role but not the sign of the polarization. Other works deal with the bioactivity of LN and LT powders, but without any attention on the adhesion and morphology of the cells onto the crystal surface[28]. Conversely, different papers have been published in the last years about the adhesion of osteoblastic cells onto polarized ceramic substrates.[41,15] Therefore, nowadays the literature lacks publications concerning the influence of the ferroelectric polarization onto cell adhesion and morphology.

The results reported here demonstrate clearly that the surface polarity of the LN crystals has no significant effect on the proliferation rate of the adhered cells, but instead, has a substantial influence on the cell behavior in terms of morphology and migration. In fact, the immunofluorescence analysis showed that the surface polarity induced remarkable differences in the arrangement of both cytoskeleton actin filaments and focal adhesions, and the migration assay demonstrated a significant difference in wound healing rate. The cells grown on *c*- presented a more pronounced spreading morphology, with well-aligned stress fibres and focal adhesions. This behavior could be explained by the differential adsorption of the chemical species floating into the culture medium. **Figure 5.11** shows the schematic view of the mechanism proposed here for explaining how the exchange of environmental ions and proteins on *c*+ and *c*- may affect the cell attachment.

The culture medium included different chemicals that had the same opportunity to interact and to be adsorbed on the surface of the crystal. However, the charged groups in the medium can be repulsed or attracted by the polarization charge on the crystal surface. Ca2+ ions are adsorbed predominantly on the negative polarity surface (*c*-) because of their superior binding affinity relative to the other cations in the medium, such as Na+, K+, and Mg2+. The cell membrane comprises a negatively charged phospholipid bilayer with embedded proteins and sugars[42]. These groups show divalent cation-dependent ligand binding and form the well-known ECM, responsible for the cell adhesion behavior. Therefore, the abundant Ca^{2+}, ions adsorbed onto the *c*- face, tend to attract those cell adhesion proteins, thus promoting a relatively strong cell adhesion. Conversely, the positive polarity of *c*+ tends to attract anionic groups, such as HPO$_4^{2-}$ and/or HCO$_3^{2-}$, which have anti-adhesive properties. This implies a weak link between the cell and the substrate since there are few points of interaction and attachment.

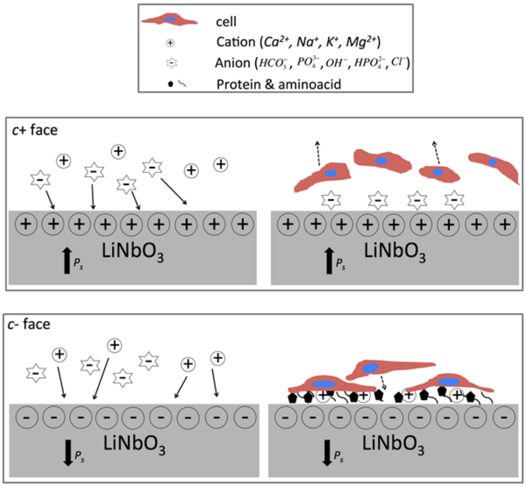

Figure 5.11: Schematic view of the interaction between the polarized surface of LN and the environmental species that contribute to cell adhesion. Organic and inorganic ions, aminoacids, and proteins float around the crystal. Cations and positively charged ionic groups are actively adsorbed on the negatively charged surface (c-), thus contributing to the strong adhesion and spreading of the NIH-3T3 cells on this surface. Anions and negatively charged species are actively adsorbed on the positively charged surface (c+), thus reducing significantly the cell spreading. The scheme is not to scale.

Since the cell morphology is related closely to the cell adhesion force, the most important physiological result of this different interaction between ions, cell adhesion proteins and polarized surface, is the different morphology and assembly of the stress fibres and focal adhesions. The cells assume a flat morphology and the adhesion plaque is extensive when a strong adhesion force is exerted on the ECM. This is the case of *c*-, where a major concentration of cations makes a stable and heavy link between the cell and the substrate, thus producing a significant formation and maintenance of well-aligned stress fibres and mainly peripheral focal adhesions. This implies that cells possessed better cell-substrate interaction to promote growth. Conversely, the cells primarily have a spherical shape and do not exert great adhesion force on the matrix when poor attachment force exists. This is the case of *c*+, where the cells have smaller focal adhesions and poorly oriented actin networks. The vinculin expression had a relatively sparse distribution around the nuclei, meaning that fibroblasts spread less and had less traction force for anchoring onto the substrate [43]. This weaker adhesion explains the prominent concrete and solid shape of the cells grown on *c*+[44-46].

The predominant well-organized stress fibres and peripheral focal adhesions on *c*-, observed in this research, is in agreement with the results concerning the cell migration rate. In fact, recent studies have reported that stress fibres are abundant and well-structured when cell adhesion is promoted and, conversely, they are absent or not well structured in case of many highly motile cells, such as leukocytes [47]. This may explain the higher wound healing rate observed in case of cells grown on *c*+, where the predominant adsorption of anionic groups tend to weaken the cell adhesion in favour of increased motility. The availability of an innovative functional material able to control the cell migration through surface charge is of great interest in different fields of application, in order to understand better the role of polarity in cell functions related to migration behavior. In fact, the cell migration plays a central role in diverse biological phenomena, including the cell ability to answer to particular chemical or mechanical stimuli. For example, the cell migration is crucial during development and wound healing [48,49]. In fact, a well-controlled cell migration is associated with normal development and function, while a misregulated motility potentiates a multitude of pathologies, including inflammation and cancer metastasis. The cell migration is also essential for technological processes that concern the tissue engineering applications, where it is of crucial importance for colonizing the biomaterial scaffold. Not surprisingly a variety of cell migration assays have been designed in order to investigate the critical components that control the cell movement.[50] It is noteworthy that, differently from the conclusions drawn in,[40] the findings presented here about the stronger adhesion of fibroblasts on *c*- are in agreement with previous studies from Kizuki et al.[51], who reported how the higher cell affinity of the negative face of polarized ceramics was due to its ability to recruit the Ca2+ ions present in the culture medium, thus confirming such interpretation.

In conclusion, significant differences in cell behavior were observed on the faces of LN crystals with opposite polarities. In particular, stronger cell adhesion with well alignment of stress fibres and focal adhesions were found in case of the negative face (*c*-). Moreover, the consequent influence on cell migration was revealed by standard assays that showed higher wound healing rate on *c*+, in full agreement with well-established studies that show how stronger cell adhesion is always associated with low motility cells. The overall results demonstrate that, contrary to a couple of works published recently on this topic, the LN crystals can be definitely used as an innovative platform for manipulating cells thorough the effects of its high magnitude spontaneous polarization, thus opening the way to the development of new principles that can be used for tissue-engineering applications. In fact, compared to standard biomaterials, this kind of platform could provide revolutionary integrated functionalities able to modulate the cell response through the surface charge patterning in combination with key properties that include pyro-electricity, photo-refractivity, and optical nonlinearity.

References

[1] J.M. Anderson, “Biological responses to materials”, *Annu. Rev. Mater.* Res., **31**,81–110, (2001)

[2] S.E. Sakiyama-Elbert, J.A. Hubbell, “Functional biomaterials: design of novel biomaterials”, *Annu. Rev. Mater. Res*,**31**,183–201, (2001)

[3] B.L. Seal, TC Otero, A. Panitch. “Polymeric biomaterials for tissue and organ regeneration”, *Mater. Sci. Eng. R,* ,**34**,147–230, (2001)

[4] S. Levenberg, R. Langer, “Advances in tissue engineering”, *Curr. Top. Dev.Biol.,* **61**,113–34, (2004)

[5] D.G. Anderson, J.A. Burdick, R. Langer, “Materials science—smart biomaterials”, *Science*, **305**, 1923–4, (2004)

[6] J.S. Temenoff, A.G. Mikos. “Reviews: tissue engineering for regeneration of articular cartilage”, *Biomaterials*, **21**, 431–40, (2000)

[7] H. Chena, L. Yuana, W. Song, Z. Wu, D. Li, “Biocompatible polymer materials: Role of protein–surface interactions “, *Progress in Polymer Science*, **33**, 1059–1087, (2008)

[8] R. Pankov, K. M.Yamada, “Fibronectin at a glance”, *Journal of Cell Science*,**115**, 3861-3863, (2002), DOI:10.1242/jcs.00059

[9] M. S. Ehrenberg, A. E. Friedman, J. N. Finkelstein, G. Oberdorster, J. L. McGrath, “The influence of protein adsorption on nanoparticle association with cultured endothelial cells”, *Biomaterials*, 30 , 603−610, (2009)

[10] M. P. Calatayuda, B.Sanza, V.Raffa, C.Riggio, M. R.Ibarra, G. F. Goya, “The effect of surface charge of functionalized Fe_3O_4 nanoparticles on protein adsorption and cell uptake”, *Biomaterials*, **35,** 6389–6399, (2014), doi:10.1016/j.biomaterials.2014.04.009

[11] S. Lin, S. Huang, S. Chen, L.U. Vinzons,J. Ciou, P. Wong, “Investigation of the Interfacial Effects of Small Chemical-Modified TiO_2 Nanotubes on 3T3 Fibroblast Responses”, *ACS Appl. Mater. Interfaces,* **6**, 12071−12082, (2014), dx.doi.org/10.1021/am503323y

[12] B.B. Manshian , D.F. Moyano , N. Corthout, S.Munck, U. Himmelreich, V.M. Rotello , S.J. Soenen, “High-content imaging and gene expression analysis to study cell - nanomaterial interactions: The effect of surface hydrophobicity”, *Biomaterials*, **35**, 9941-9950, (2014)

[13] J.Shiu, C.Kuo, W.Whang, P.Chen, “Observation of enhanced cell adhesion and transfection efficiency on superhydrophobic surfaces”, *Lab Chip*, **10**, 556-558; (2010), DOI: 10.1039/c000798f

[14] J. Lin, H. Chang, W. Kao, K. Lin, H. Liao, Y.You, Y.Kuo, D.Kuo, K.Chu, Y.Chu, J.Shyue, “Effect of Surface Potential on Extracellular Matrix Protein Adsorption”, *Langmuir,* **30,**10328−10335, (2014), dx.doi.org/10.1021/la5020362

[15] F. R. Baxter, C. R. Bowen, I. G. Turner, A. C. E. Dent, “Electrically Active Bioceramics: A Review of Interfacial Responses”, *Annals of Biomedical Engineering*, 38, 2079–2092, (2010), DOI: 10.1007/s10439-010-9977-6

[16] E. Fukada, I. Yasuda, “On the piezoelectric effect of bone”, *J. Phys. Soc. Jpn.*, 12,1158–1162, (1957)

[17] G. W. Hastings, F. A. Mahmud, “The electromechanical properties of fluid-filled bone: a new dimension”, J. *Mater. Sci. Mater. Med.,* 2,118–124, (1991)

[18] J. H. McElhaney, “The charge distribution on the human femur due to load”*J. Bone. Jt. Surg*, **49A**,1561–1571, (1967)

[19] J.Feng,H. P. Yuan, X. D. Zhang, “Promotion of osteogenesis by a piezoelectric biological ceramic“, *Biomaterials,* **18**, 1531–1534, (1997)

[20] T.Kobayashi, S. Nakamura, K. Yamashita, Enhanced osteobonding by negative surface charges of electrically polarized hydroxyapatite. J. Biomed. Mater.Res. , **57,** 477–484, (2001)

[21] M Nakamura, A. Nagai, Y. Tanaka, Y. Sekijima, K. Yamashita, “Polarized hydroxyapatite promotes spread and motility of osteoblastic cells”, *J. Biomed. Mater. Res.,*(2009), DOI:10.1002/jbm.a.32404

[22] M.Ohgaki, T. Kizuki, M. Katsura, K. Yamashita, “Manipulation of selective cell adhesion and growth by surface charges of electrically polarized hydroxyapatite”, *J. Biomed. Mater. Res.,* **57**, 366–373, (2001)

[23] J. Israelachvili, Intermolecular and Surface Forces, 2nd ed. (2000), p. 217

[24] Z.Zhang, P. Sharma, C. N. Borca, P. A. Dowben, A. Gruverman, “Polarization-specific adsorption of organic molecules on ferroelectric LiNbO 3 surfaces”, *Appl. Phys. Lett.*, **97**,243702; DOI: 10.1063/1.3525373

[25] S. Dunn, D. Cullen, E. Abad-Garcia, C. Bertoni, R. Carter, D. Howorth, R. W. Whatmore, “Using the surface spontaneous depolarization field of ferroelectrics to direct the assembly of virus particles”, *Appl. Phys. Lett*, **85**, 3537, (2004), DOI: 10.1063/1.1797535

[26] J. Garra, J.M. Vohs , D.A. Bonnell , “The effect of ferroelectric polarization on the interaction of water and methanol with the surface of $LiNbO_3$(0001)”, *Surface Science*, **603**, 1106–1114, (2009)

[27] X. Sun, Y. J. Su, X. Li, K. W. Gao, and L. J. Qiao, “Stability of nano-scale ferroelectric domains in a LiNbO3 single crystal: The role of surface energy and polar molecule adsorption”, *Journal of Applied Physics*, **111**,094110, (2012), DOI: 10.1063/1.4711098

[28] P.M.Vilarinho, N.Barroca, S.Zlotnik, P.Félix, M.H.Fernandes, “Are lithium niobate ($LiNbO_3$) and lithium tantalate ($LiTaO_3$) ferroelectrics bioactive?”, *Materials Science and Engineering C*, **39,** 395–402, (2014)

[29] M. Nakamura, Y.Sekijima, S.Nakamura, T.Kobayashi, K.Niwa, K.Yamashita, “Role of blood coagulation components as intermediators of high osteoconductivity of electrically polarized hydroxyapatite”, J Biomed Mater Res A, **79**,627–634, (2006), DOI: 10.1002/jbm.a.30827

[30] C. Christophis, E. A. Cavalcanti-Adam, M. Hanke, K. Kitamura, A. Gruverman, M. Grunze, P.A Dowben , A. Rosenhahn, “Adherent cells avoid polarization gradients on periodically poled $LiTaO_3$ ferroelectrics”, *Biointerphases* **8**,27, (2013)

[31] R. S. Weis ,T. K. Gaylord, Lithium Niobate: “Summary of Physical Properties and Crystal Structure”, *Appl. Phys. A*, **37,** 191-203, (1985)

[32] S. R. Ryoo, Y. K. Kim, M. H. Kim, D. H. Min, "Behaviors of NIH-3T3 Fibroblasts on Graphene/Carbon Nanotubes: Proliferation,Focal Adhesion, and Gene Transfection Studies", *ACS Nano* , **4**, 6587−6598, (2010)

[33] A. Dolatshahi-Pirouz, T. Jensen, D. C.Kraft, M.Foss, P. Kingshott, J. L. Hansen,; A. N. Larsen, J. Chevallier, F. Besenbacher, "Fibronectin Adsorption, Cell Adhesion, and Proliferation on Nanostructured Tantalum Surfaces", *ACS Nano* , **4**, 2874−2882, (2010)

[34] C.Liang, A. Y Park, J.Guan, "In vitro scratch assay: a convenient and inexpensive method for analysis of cell migration in vitro", *Nature Protocols*, **2**,329, (2007), DOI:10.1038/nprot.2007.30

[35] J.C. Yarrow, Z.E Perlman, N.J Westwood, T.J. Mitchison, "A high-throughput cell migration assay using scratch wound healing, a comparison of image-based readout methods", *BMC Biotechnology,* **4**, 21, (2004), DOI:10.1186/1472-6750-4-21

[36] A.J. Ridley , M.A. Schwartz , K. Burridge , R.A. Firtel , M.H. Ginsberg , G. Borisy , J.T. Parsons, A.R. Horwitz, "Cell migration: integrating signals from front to back", **302**, 1704-9, (2003)

[37] J. E. Davies, "The importance and measurement of surface charge species in cell behaviour at the biomaterial interface", *Surface Characterisation of Biomaterials*, (1988)

[38] M. Vert, Y. Doi, K. Hellwich, M. Hess, P. Hodge, P. Kubisa, M. Rinaudo, F. Schué, "Terminology for biorelated polymers and applications (IUPAC Recommendations 2012)", *Pure Appl. Chem.,* **84**, 377-410, (2012)

[39] C. Christophis, E.A. Cavalcanti-Adam, M. Hanke,, K. Kitamura, A. Gruverman, M. Grunze, P.A. Dowben, A. Rosenhahn, "Adherent cells avoid polarization gradients on periodically poled $LiTaO_3$ ferroelectrics", *Biointerphases* **8**, 27, (2013)

[40] N.C. Carville, L. Collins, M. Manzo, K. Gallo, B.I. Lukasz, K.K. McKayed, J.C. Simpson, B.J. Rodriguez, "Biocompatibility of ferroelectric lithium niobate and the influence of polarization charge on osteoblast proliferation and function", *J Biomed Mater Res Part A* , 2014; DOI: 10.1002/jbm.a.35390

[41] M.Nakamura, A.Nagai, Y.Tanaka, Y.Sekijima, K.Yamashita, “Polarized hydroxyapatite promotes spread and motility of osteoblastic cells”, *Journal of Biomedical Materials Research Part A*, (2012) DOI: 10.1002/jbm.a.32404

[42] K. E.Healy, B.Lom, P. E. Hockberger, “Spatial Distribution of Mammalian Cells Dictated by Material Surface Chemistry”, *Biotechnol.Bioeng.*, **43**, 792−800, (1994)

[43] D. W. Dumbauld, T. T.;Lee, A.Singh, J. Scrimgeour, C. A. Gersbach, E. A. Zamir, J. Fu, C. S.Chen, J. E.Curtis, S.W. Craig, A. J. García, “How Vinculin Regulates Force Transmission”, *Proc. Natl. Acad. Sci. U.S.A.* , **110**, 9788−9793, (2013)

[44] P. K.Mattila, P. Lappalainen, “Filopodia: Molecular Architecture and Cellular Functions”, *Nat. Rev. Mol. Cell Biol.*, **9**, 446−454, (2008)

[45] T. Yeung, P. C. Georges, L. A. Flanagan, B. Marg, M. Ortiz, M. Funaki, N. Zahir, W. Ming, V. Weaver, P. A. Janmey, “Effects of Substrate Stiffness on Cell Morphology, Cytoskeletal Structure, and Adhesion”, *Cell Motil. Cytoskeleton ,* **60**, 24−34, (2005)

[46] S. Pellegrin, H. Mellor, “Actin Stress Fibres.”, *J. Cell Sci.* , **120,** 3491−3499, (2007)

[47] N. H.Valerius, O. Stendahl, O. X. Hartwig, T. P. Stossel, “Distribution of actin-binding protein and myosin in polymorphonuclear leukocytes during locomotion and phagocytosis”, *Cell*, **24**, 195-202., (1981)

[48] S. F. Gilbert, (2003). “Developmental Biology”, 7th edn.Sunderland, MA: Sinauer

[49] A. J. Ridley, M. A. Schwartz, K. Burridge, R. A. Firtel, M. H. Ginsberg, G. Borisy, J. T. Parsons, A. R. Horwitz, “Cell Migration: Integrating Signals from Front to Back”, *Science*, **302**, 1704-1709, (2003)

[50] N. Kramer, A. Walzl , C. Unger , M. Rosner , G. Krupitza ,M. Hengstschlager , H. Dolznig , “In vitro cell migration and invasion assays”, *Mutation Research*, **752**, 10–24, (2013)

[51] T. Kizuki, M. Ohgaki, M. Katsura, S. Nakamura, K. Hashimoto, Y. Toda, S. Udagawa , K. Yamashita, "Effect of bone-like layer growth from culture medium on adherence of osteoblast-like cells", *Biomaterials*, **24**, 941–947, (2003)

Chapter 6

Bipolar patterning of free-standing polymer membranes

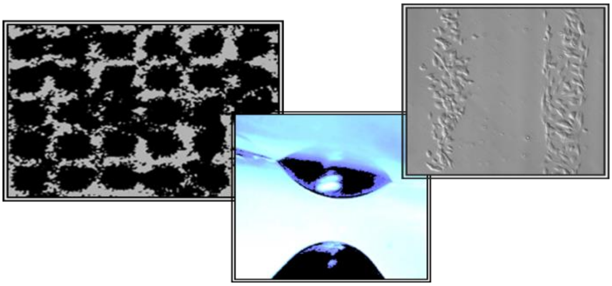

In this chapter, the pyroelectric field induced by a standard thermal stimulus (i.e. hot plate) is used to produce an electrified membrane characterized by the presence of quasi-permanent dipoles able to influence cell growth. In this contest, exception made for the initial phase of production, we can disentangle from the physical presence of the crystal opening a new route in different application fields.

The availability of localized electrostatic fields is of great interest for a huge amount of applications including positioning of micro-particles as building blocks for electrical, optical and magnetic devices [1-4]. In particular, much attention has been devoted in the recent years to the possibility of charging polymer-based materials, due to their perspective in developing large-scale and inexpensive flexible thin-film technology. Different approaches have been reported in literature for realizing charged polymer surfaces, such as thermo-electrical [5], liquid-contact [6], corona discharge [7,8], electron-beam [9].

In particular, the thermo-electrical method involves the application of electric fields at elevated temperatures followed by appropriate cooling-down of the dielectric polymer. At equilibrium, the dielectric polymer has dipole molecules (dipoles) arranged randomly, while at elevated temperatures (above the glass transition temperature T_g) the material becomes very amorphous, homogeneous, and elastic, and the dipoles can orient easily in the direction of the applied field. The material is allowed to cool-down to room temperature gradually and, finally, after removing the external electric field, the material consists of mainly aligned dipoles and exhibits a nonzero surface charge [10,11]. Different techniques have been presented in literature for patterning these surface charges and the more relevant make use of conductive stamps [12] or atomic force microscopy tips [13]. More recently, electrical nano-imprint lithography has been proposed for simultaneous charge writing and topography structuring [14]. However, to the best of our knowledge, all of the techniques presented in literature for charging polymeric materials have in common the use of external electrodes and voltages. Recently, we have developed a series of applications making use of the electrostatic fields generated spontaneously onto the surface of pyroelectric lithium niobate (LN). Thanks to the largest known magnitude of spontaneous polarization at room temperature ($\sim 71\ \mu C/cm^2$) [15], LN has been demonstrated to be useful for a wide variety of applications with the key advantage of being electrode-free, and thus opening the route to more versatile configurations. These include, for example, dielectrophoresis-based patterning of fluids and particles [16-18], nozzle-free nano-dispensing [19], re-shaping [20] and even biosensing [21].

Here we report a voltage-free pyro-electrification (PE) process able to induce permanent and 2D patterned dipoles into polymer films, thus producing freestanding bipolar membranes. A single thermal stimulus triggers simultaneously the glass transition and the dipole orientation in the polymer. The technique is surprisingly easy to accomplish since the polymer solution is simply spin-coated onto a pyroelectric LN crystal that, during the thermal stimulus, generates spontaneously a surface charge density strong enough to orient the polymer dipoles. The LN crystal is the key component that plays the multi-purpose role of sustaining, heating and poling the polymer layer that is then peeled-off easily in order to have a freestanding charged membrane. Compared to the previous mentioned electrification techniques, the PE is electrode-free, thus simplifying the process significantly, and it provides an additional advantage. The dipoles can be oriented according to a homogeneous as well as to a periodic distribution of domains with opposite polarities. This is achieved simply by using a single domain or a periodically poled LN (PPLN), respectively as template. In fact, unlike the techniques reported in literature, where the patterns consist of domains with oriented and non-oriented dipoles, here the domains are all oriented with opposite polarities, thus providing additional functionalities due to the bipolar feature of such patterned membranes. To the best of our knowledge, only recently Lim et al. [22] proposed the above-mentioned electric microcontact printing [12] in combination with a pre-coating of positive ions, in order to get bipolar charge patterns. However, still external electrodes and multiple process steps are required there. Recently, Huang et al. have exploited the pyroelectric effect for poling polymer films [23,24], but without bipolar charge patterning and only in case of a doped polymer. We demonstrate here the reliability of the PE technique for different polymers and in case of periodic bipolar charge patterns. The reported results show the possibility of using the resulting charged membranes for multi-purpose applications, ranging from nozzle- and heat-free dispensing, up to live cell patterning.

6.1 Experimental section and principle of operations

Figure 6.1 shows the schematic view of the PE procedure. The key element is the pyroelectric LN slide that can be used as a single domain or as a PPLN crystal [25].The LN crystals were bought from Crystal Technology Inc. in the form of both sides polished 500μm thick *c*-cut 3-inch wafers and were cut into square samples (2×2) cm^2 sized by a standard diamond saw. As better described in Chapter 2, *t*he PPLN were obtained by standard electric field poling onto photoresist patterned samples [24]. Two geometries were considered: linear (period 400 μm); square array of hexagons (period 200 μm).

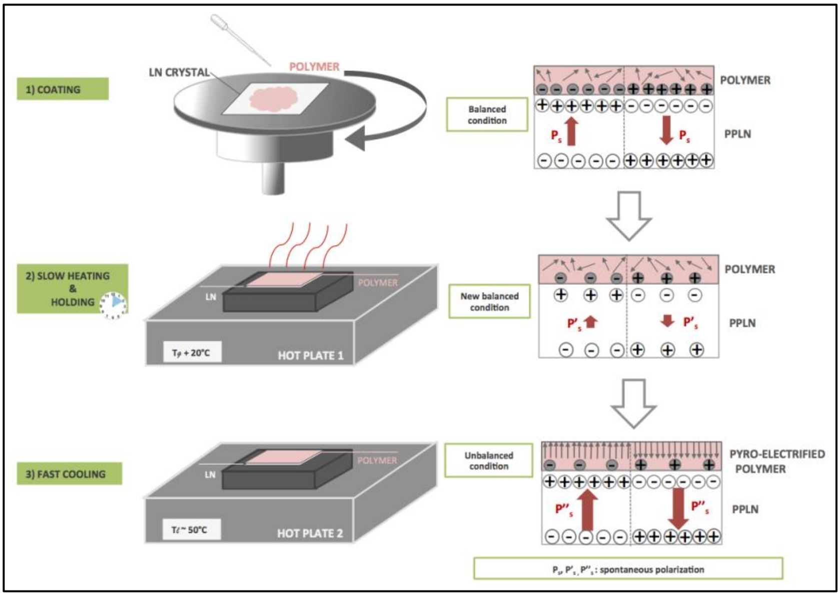

Figure 6.1. Schematic view of the PE process steps (left column) and of the corresponding distributions of charges (right column).

It is well known that, at equilibrium, the spontaneous polarization P_s of the *c*-cut LN crystal is fully compensated by the external screening charges, and no electric field exists. According to the pyroelectric effect, a temperature change ΔT causes a variation $\Delta P_s \propto \Delta T$, which, neglecting the losses, builds up uncompensated surface charges corresponding to a charge density $\sigma = P_c\ \Delta T$, where P_c is the pyroelectric coefficient (see details in [18,26]). In other words, the temperature variation weakens the polarization alignment into the crystal and a transient state establishes, characterized by a charge failure between the crystal polarization and the external environment.

The crystal sample was spin-coated with a polymer solution at RPM values ranging from 2.000 up to 4.000, depending on the solution viscosity, and was stimulated by an appropriate three stage thermal treatment by conventional digital hotplates: 1) slow heating, the temperature is risen gently from the room value T_i up to $T_f = T_g$+20°C at about 1°C/min; 2) holding, where T_f is maintained for about 10 minutes; 3) fast cooling, the polymer-coated crystal is moved to a second hotplate set at a lower temperature T_l (~50°C). The slow temperature variation in the first stage allows one to avoid the pyroelectric effect and therefore to have a charge balance when the polymer goes through its glass transition and its molecules are not able to re-orient. The 10 min holding stage allows the screening charges and the spontaneous polarization P_s of the crystal to reach a new balance state at elevated temperatures. Conversely, surface uncompensated charges are induced purposely in correspondence of the dramatic temperature change due to the fast cooling stage, so that first of all, the intensity of the resulting electric field is high enough for aligning the polymer dipoles during their amorphous and more mobile state and then, the dipoles orientation is frozen, since T_l ($< T_g$ of polymers) is reached. In fact, the voltage intensities corresponding to the pyroelectric field are around dozens of *kV* [27], in agreement with the voltage values reported for poling polymers [28]. The monotonic cooling protocol is necessary to provide large temperature variation ΔT and generate a steady and strong static electric field for poling. Therefore, the electrified polymer consists of frozen-in aligned dipolar charges exposing the same polarity of the crystal polarization (see **Figure 6.1**). The polymer layer may be used attached to the crystal as well as a freestanding flexible membrane, after simple peeling-off.

The reliability and the multi-purpose capability of the PE technique was demonstrated for different polymers and for two different configurations: the single domain PE (SD-PE) used a single domain crystal support, while the multi-domain PE (MD-PE) employed a PPLN crystal with different geometries, as specified above. The supporting crystal was re-used after cleaning. In case of SD-PE configuration, the polymer layer exhibits a surface charge with single sign that depends onto the adhering *c*-face of the crystal: negative when laying onto *c*+ and viceversa (see **Figure 6.1**). In case of the MD-PE configuration the polymer show the pattern of polarized domains with opposite signs, in accordance with the ferroelectric domains imposed by the PPLN support. **Table 6.1** shows the list of polymer solutions used for the PE process.

All of the polymers presented here were used as received without further purification. Poly(methyl methacrylate) (PMMA) (Sigma Aldrich 182265 Mw 996K) was dissolved at 30 %w/w in anisole and stirred at 70°C for 3 hours. Polystyrene (PS) (Sigma Aldrich 430102 Mw 192 K) was dissolved at 60 %w/w in anisole stirred at 70°C for 6 hours. Poly(vinyl alcohol) (PVA)(Sigma Aldrich P1763 fully hydrolyze) was dissolved at 15 %w/w in distilled water stirred at 50°C for 4 hours. Polyethylene glycol (PEG) (Sigma Aldrich 1546569 Mw 4,000) was dissolved at 40 %w/w in distilled water. All of the polymer solutions were deposited by standard spin coating on the LN crystals.

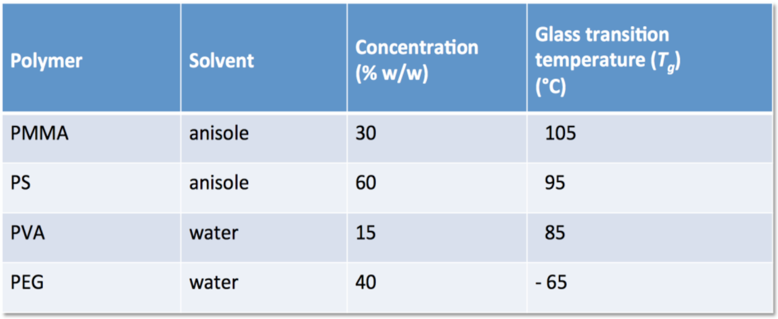

Polymer	Solvent	Concentration (% w/w)	Glass transition temperature (T_g) (°C)
PMMA	anisole	30	105
PS	anisole	60	95
PVA	water	15	85
PEG	water	40	- 65

Table 6.1: List of polymer solutions used for fabricating the pyro-electrified membranes **[29]**.

6.2 Liquid dispensing applications

The SD-PE was applied to each polymer solution and the resulting charged membranes were used for the purpose of liquid dispensing, as a heat-free variation of the pyro-dispenser [19] in order to extend the fields of applications. In fact, this PE provides electric fields strong enough to induce electro-hydro-dynamic (EHD) dispensing that, in addition to the electrode- and nozzle-free advantages of the pyro-dispenser, is heat-free. This opens the route to a new nano-dispensing technology that is completely free from in-situ functionalization and stimuli, with significant improvements in all of those fields where small amounts of liquids need to be manipulated but external stimuli such as electrical and/or thermal can be detrimental, as in case of biological applications. **Figure 6.2(a,b)** shows the typical side view of the liquid dispensing through the PE membrane flat or curved, respectively, and **Figure 6.2(c)** shows the typical dispensed droplets of liquid PMMA. More details about the dispensing set-up can be found in [19].

The flexibility of the charged membrane would enable novel dispensing configurations. The key differences here are the use of the PE slide in place of the pyroelectric crystal and the absence of the external stimulus. A 0.2µL drop of a test liquid (PMMA in anisole at 9% w/w) was dispensed manually onto the base support. The distance between the base-drop and the PE slide was regulated precisely by a standard translation stage. In analogy with the pyro-dispenser, when approaching the PE slide, liquid molecules of the base drop, are polarized in the electric field produced by the PE membrane. An electric charge is induced at the surface of the liquid meniscus, creating an electric stress that stretches the meniscus into a conical shape, called Taylor cone, in the direction of the field, and a droplet or jet of liquid is formed when the electrostatic force is stronger than the surface tension [30]. There is, therefore, a critical value of the electric field, depending on the electrification strength of the PE slide, in which the electrostatic force exceeds the force of surface tension and induces the liquid jet.

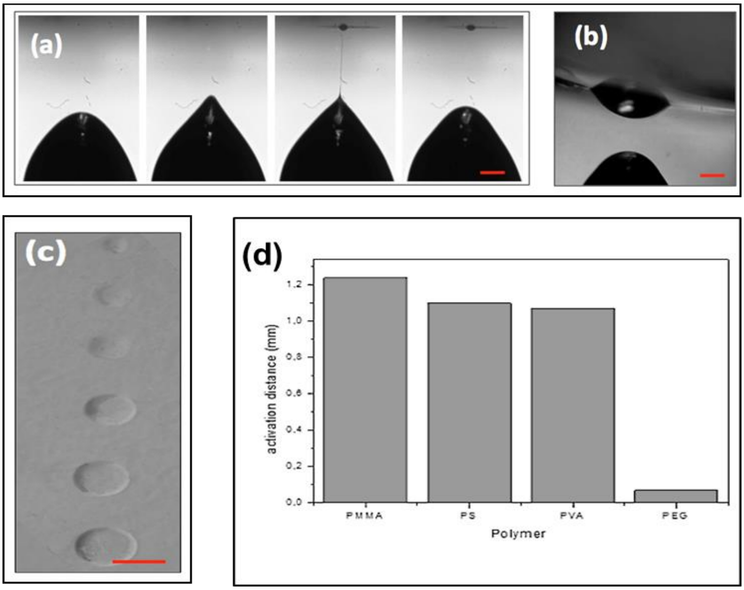

Figure 6.2. (a,b) Camera side view of the liquid dispensing onto a flat or a curved PE membrane, respectively; (c) microscope images of typical dispensed droplets; (d) distribution of the activation distance values for PE membranes made of different polymer solutions. Scale bars 200 µm.

Figure 6.2(d) shows the distribution of the activation distances for the PE slides investigated here. The results show clearly that the highest electrostatic effect is provided by PMMA, PS and PVA polymers, while a poor effect was observed in case of PEG. The polymers PMMA, PVA, and PEG are polar dielectrics thanks to the ester (PMMA) and hydroxyl (PVA, PEG) groups [31], where the ester exhibits stronger polarity. Conversely, a non-polar phenyl group characterizes the PS structure [31]. However, besides the polarity of the substituent, the molecule bonds also have a role. In fact, the non-polar phenyl of PS guarantees a strong polarizability, thanks to the aromatic ring that is π electron-rich. In general, the electrons in a π bond lie outside of the internuclear axis and, consequently, are farer away from the nucleus, are less tightly held by the nucleus, and are therefore more polarizable than in a sigma bond where the electrons are tightly held in the space between the two nuclei involved in a bond [32]. Due to the application of the electric field, a dipole moment is induced, resulting in orienting them in the field direction [33, 34]. A π bond is present also in the structure of PMMA and the combination of high polarity and high polarizability makes this PE membrane to exhibit the highest electrostatic efficiency, followed by the PS which under the electric field is more polarizable then PVA and PEG. The weaker electrostatic force of the PEG membrane is due basically to its negative glass transition temperature that is lower than the melting point T_m (for PEG T_g = -65°C; T_m = 56°C). The PE process was performed by using T_f = 70°C (>T_m), namely a value that enabled a significant pyroelectric field intensity. However, since the temperature is well above T_g during the whole process, the dipole molecules are constantly free to re-orient till to the depletion of the pyroelectric field, thus preventing the stabilization of the dipole orientation achieved in correspondence of the fast cooling step. The slight dispensing reactivity of the base drop measured for the PEG membrane (see **Figure 6.2(d)**) is due to the weak polarization effect achieved by exceeding the melting point of PEG. The vibrational energy achieved by the polymer molecules @ T_f exceeds their bonding energy, leading to chain scissions [35,36]. The resulting shorter mono- and oligomer units tend to re-orient under the action of the pyroelectric field. However, due to the higher degree of proximity of the unit edges, they interact each other stronger than in case of long chains, thus weakening the resulting polarization effect. Consequently, the fast cooling of the molten PEG induces the solid phase transition with in-frozen polarization much lower than that exhibited by the dipole orientation of the whole chains in case of PMMA, PS and PVA.

6.3 Cell patterning applications

The MD-PE was achieved by using a PPLN support in place of the single domain crystal sample (see **Figure 6.1**). PPLN supports with two different geometries were used for demonstrating the reliability of the technique: periodic square array of hexagonal domains (period 200 μm); periodic linear domains (period 400 μm). The PE process was performed analogously to SD-PE and the resulting PE slide was detached gently from the PPLN support. In this case the polymer membrane had a pattern of polarized domains with opposite signs, according to the ferroelectric domain pattern of the driving PPLN support. It is important to note that the PE domains extend into the whole volume of the membrane, regardless of the polymer, thus providing membranes with charge patterns with opposite signs on the two faces. The opposite sign polarization pattern was evidenced by a decoration technique, where a conventional negatively charged toner powder was dispersed gently onto the surface of the PE membrane. **Figure 6.3(a,b)** show the corresponding optical microscope images after decoration onto PPLN crystal, where the hexagonal domains exhibit positive or negative polarity, respectively, by using simply the opposite faces of the same PE membrane. The toner particles are attracted clearly by the areas with positive polarity. It is important to note that, even though finer patterns can be obtained for example by electron μ-Contact Printing or by conductive atomic force tips [12,13], the features presented here are free-standing membranes that, for the first time, exhibit bipolarity. The finer period structures are simply related to the mask used for poling the crystal that is then re-used several times for producing different PE membranes. All of the PE membranes appear to exhibit a relatively good stability over several months.

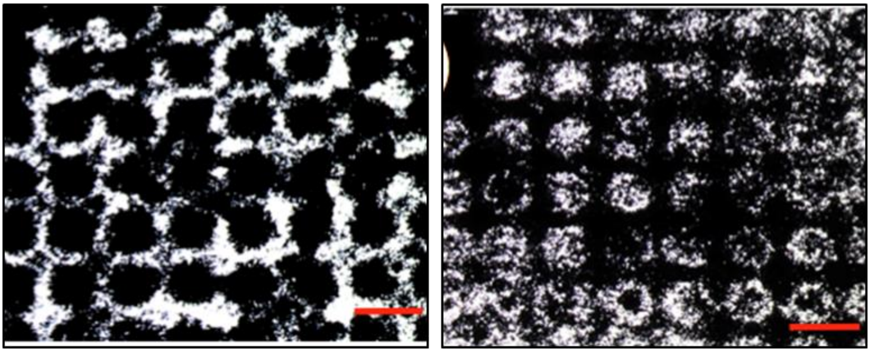

Figure 6.3 (a,b): Optical microscope images of two patterned PS membranes decorated by toner powder, where the hexagonal domains exhibit positive and negative polarity, respectively (scale bar 200μm)

The multi-purpose capability of the PE membranes was demonstrated also in case of a typical wet ambient application: live cell patterning. Human neuroblastoma cells (SH-SY5Y) were cultured *in vitro* on two different PE polymers: PS in anisole at 60% (w/w) and PMMA in anisole at 30% (w/w), electrified onto the *c*- face for linear PPLN and on the c+ face for hexagonal PPLN.

The SH-SY5Y cell line was purchased from ECACC (Sigma-Aldrich, Milan, Italy). They were routinely grown in Dulbecco's modified Eagle's medium (DMEM) containing 4.5 g/L D-glucose and supplemented with 2mM L-glutamine, penicillin (100 units/ml), streptomycin (100 μg/ml), and containing 20% (v/v) fetal bovine serum (FBS) (GIBCO, Gaithersburg, MD, USA). For the cell culture experiments, the SH-SY5Y were detached by means of Trypsin/EDTA solution (Sigma, Milan, Italy), re-suspended in DMEM-20% FBS and seeded at a concentration of 1.0×10^5 cells/mL on the MD-PE membranes (immersed in DMEM medium at 37 °C for 1 h prior to use) and, then, incubated into conventional 30 mm diameter Petri dishes at 37 °C and in a saturated humidity atmosphere containing 95% air and 5% CO_2. Cells were allowed to grow in DMEM-20% FBS on different substrates for 24 h.

Linear (period 400 μm) and square hexagonal (period 200 μm) geometries were tested for PS and PMMA membranes, where the hexagonal regions exhibiting a negative polarity. The adhesion and spreading were observed over 24h under a standard inverted optical microscope (AxioVert, Carl Zeiss, Germany). **Figure 6.4** shows the optical microscope images of the cells after 24h incubation. In particular, **Figure 6.4(a)** refers to the cells cultured onto a pyro-electrified PS membrane under magnified and large view (inset), while **Figure 6.4(b)** shows a larger view of the same flexible membrane after removal from the Petri dish. **Figure 6.4(c,d)** show the cell patterning onto a PMMA and a PS membrane, respectively, pyro-electrified by a square array of hexagons.

It is well known that polymers such as PS and PMMA are naturally cytophobic and require specific functionalization treatments in order to promote cell adhesion [37-39]. Here, instead, the MD-PE membrane clearly appears to favor the cell adhesion and spreading onto the regions with positive polarity, in agreement with recent findings [40 and Refs therein], thus opening the route to a novel generation of platforms for cell patterning applications, with the additional advantage of being supported by a flexible membrane.

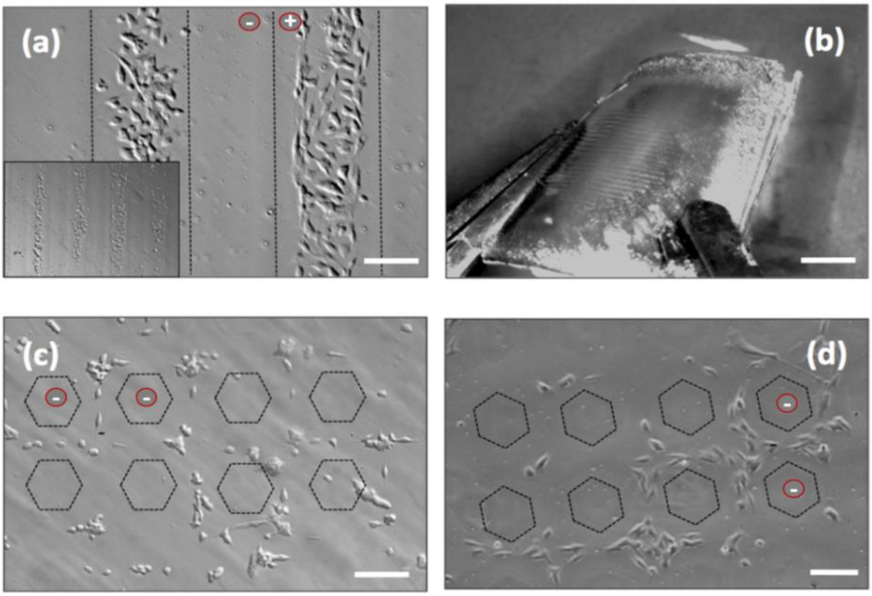

Figure 6.4. Optical microscope images of SH-SY5Y cells after 24h incubation on (a,b) PS membrane pyro-electrified linearly at 400 µm period while incubating into the Petri dish and soon after removal, respectively (scale bars 100 µm and 2 mm, the inset shows a large view of the cell patterning); (c,d) cell patterning on PMMA and PS membranes pyro-electrified by an array of hexagons at 200 µm period, respectively (scale bars 100 µm). The dashed lines correspond to the boundaries between regions with opposite polarities.

In conclusion, in this chapter, we have described a novel PE technique able to fabricate multi-purpose polymer membranes with permanent bipolar patterns.

The technique is surprisingly simple thanks to the use of spontaneous pyroelectric charges arising onto the ferroelectric crystal surface during the thermal treatment. In particular, for PPLN supports, one single thermal stimulus enables simultaneously the glass transition and the periodic electric poling of the polymer. This approach represents a simple and valid alternative to conventional methods where external voltages and electrodes are used for polymer poling. The reliability of the PE membranes has been demonstrated for multi-purpose applications ranging from liquid dispensing up to micro-object patterning under dry (toner powder) and wet ambient (live cells).

References

[1] D.L. Klein, R. Roth, A.K. Lim, A.P. Alivisatos, P.L. McEuen, “A single-electron transistor made from a cadmium selenide nanocrystal”, *Nature,* **389**, 699 - 701, (1997)

[2] F.E. Kruis, H. Fissan, A. Peled, “Synthesis of nanoparticles in the gas phase for electronic, optical and magnetic applications—a review” *J. Aerosol Sci.*, **29**, 511-535, (1998)

[3] H. Kim, J. Kim, H. Yang, J. Suth, T. Kim, B. Han, S. Kim, D.S. Kim, P.V. Pikhitsa, M. Choi,” Parallel patterning of nanoparticles via electrodynamic focusing of charged aerosols”, *Nat. Nanotechnol.*, **1**, 117-121, (2006)

[4] O. Gennari, S. Grilli, S. Coppola, V. Pagliarulo, V. Vespini, G. Coppola, S. Bhowmick, M.A. Gioffré, G. Gentile, V. Ambrogi, P. Cerruti, C. Carfagna, P. Ferraro., “Spontaneous assembly of carbon-based chains in polymer matrixes through surface charge templates.”, *Langmuir*, *29*, 15503-15510, (2013)

[5] G.M. Sessler, J.E. West,” Self-Biased Condenser Microphone with High Capacitance”, *J. Acoust. Soc. Am.*, **34**, 1787, (1962)

[6] P. W. Chudleigh, ” Mechanism of charge transfer to a polymer surface by a conducting liquid contact, *J. Appl. Phys.*, **47**.4475-4483, (1976).

[7] R.A. Creswell, M.M. Perlman, “hermal Currents from Corona- Charged Mylar,” *J. Appl. Phys.*, **41**, 2365-2375, (1970)

[8] D.A. Rychkov, A.E. Kuznetsov, A.A. Rychkov, V.A. Goldade, *14th International Symposium on Electrets (ISE)*, , 111, (*2011)*

[9] T. Matsukawa, R. Shimizu, K. Harada, T. Kato, “Investigation of kilovolt electron energy dissipation in solids”, *J. Appl. Phys.,* **45**, 733, (1974)

[10] Perlman, M. Martin, J. L. Meunier, “Charge Decay of Carnauba Wax Electrets”, *J. Appl. Phys.*, **36**, 420, (1965)

[11] M.Eguchi, "On the permanent electret.", *Philos. Mag.*, **49**,178-181, (1925)
[12] H. O. Jacobs, G. M. Whitesides, "Submicrometer patterning of charge in thin-film electrets.", *Science*, **291**, 1763-1766, (2001)

[13] P. Mesquida, A. Stemmer, "Attaching Silica Nanoparticles from Suspension onto Surface Charge Patterns Generated by a Conductive Atomic Force Microscope Tip", *Adv. Mater*. **13**, 1395, (2001)

[14] L. Ressier, E. Palleau, S. Behar, "Electrical nano-imprint lithography.", *Nanotechnol.*, **23***,255302*, (2012)

[15] G. Rosenman, D. Shur, Y. E. Krasik, A. Dunaevsky, "Electron emission from ferroelectrics", *J. Appl. Phys.*, **88**, 6109, (2000)

[16] S. Grilli, P. Ferraro, "Dielectrophoretic trapping of suspended particles by selective pyroelectric effect in lithium niobate crystals", *Appl. Phys. Lett.*, **92**, 232902, (2008)

[17] P. Ferraro, S. Grilli, L. Miccio, V. Vespini, " Wettability patterning of lithium niobate substrates by modulating pyroelectric effect to form microarray of sessile droplets", *Appl. Phys. Lett.*, **92**, 213107, (2008)

[18] S. Grilli, V. Vespini, P. Ferraro, "Surface-Charge Lithography for Direct PDMS Micro-Patterning", *Langmuir*, **24**, 13262-13265, (2008).

[19] P. Ferraro, S. Coppola, S. Grilli, M. Paturzo, V. Vespini, "Dispensing nano–pico droplets and liquid patterning by pyroelectrodynamic shooting", *Nat. Nanotechnol.*, **5***,* 429, (2010)

[20] S. Grilli, S. Coppola, V. Vespini, F. Merola, A. Finizio, P. Ferraro, "3D lithography by rapid curing of the liquid instabilities at nanoscale", *P Natl Acad Sci USA*, **108**, 15106, (2011)

[21] S. Grilli, L. Miccio, O. Gennari, S. Coppola, V. Vespini, L. Battista, P. Ferraro, "Active accumulation of very diluted biomolecules by nano-dispensing for easy detection below the femtomolar range.", *Nat. Com.* ,**5**, 5314, (2014)

[22] K. Lim, J. R. Lee, H. Lee, P. V. Pikhitsa, S. You, C. G. Woo, M. Choi, “Nanoxerography utilizing bipolar charge patterns”, *Appl. Phys. Lett.*, **101**, 203106, (2012).

[23] S. Huang, J. Luo, Z. Jin, M. Li, T. D. Kim, A. Chen, A. K. Y Jen, “Spontaneously Poling of Electro-Optic Polymer Thin Films across a 1.1-mm Thick Glass Substrate by Pyroelectric Crystals”,*Appl. Phys. Lett.*, **105,** 183305, (2014)

[24] S.Huang, J. Luo, H. L.Yip, A. Ayazi, X. H. Zhou, M.Gould, A. K. Y Jen, “"Electro‐optical Materials: Efficient Poling of Electro‐Optic Polymers in Thin Films and Silicon Slot Waveguides by Detachable Pyroelectric Crystals”, *Adv Mater*, , **24**, 42, (2012)

[25] S. Grilli, M. Paturzo, L. Miccio, P. Ferraro, “In situ investigation of periodic poling in congruent LiNbO3 by quantitative interference microscopy”, *Meas. Sci. Technol.*, **19**, 074008, (2008)

[26] B. Rosenblum, , P. Bräunlich, J. P. Carrico, “Thermally stimulated field emission from pyroelectric LiNbO3”, *Appl. Phys. Lett*, **25**, 17, (1974)

[27] L. Battista, L. Mecozzi, S. Coppola, V. Vespini, S. Grilli, P. Ferraro, “Graphene and carbon black nano-composite polymer absorbers for a pyro-electric solar energy harvesting device based on $LiNbO_3$ crystals”, *Appl. Energ.*, **136***,* 357, (2014)

[28] J. Matallana, J. Bigarre, P. Hourquebie, R. Coelho, H. Janah, P. Mirebeau, A. Toureille, *Electrical Insulation and Dielectric Phenomena, Annual Report. Conference* 2001 488.

[29] C. E. Wilkes, J. W. Summers. *PVC handbook*. Munich, Hanser, 2005.

[30] L. T. Cherney,” Structure of Taylor cone-jets: limit of low flow rates", *J. Fluid. Mech.,* **378**, 167-196, (1999)

[31] R. T. Morrison, R. N. Boyd, P. Grünanger, P. Vita-Finzi, *Chimica organica* 1976 Casa editrice ambrosiana.

[32] K.Jug, A.M. Koester, "Influence of .sigma. and .pi. electrons on aromaticity", *J. Am. Chem. Soc.*, **112**, 6772, (1990)

[33] K. C. Kao, *Dielectric phenomena in solids*, Academic press 2004.

[34] M. Monti, M. Natali, L. Torre, J. M. Kenny, "The alignment of single walled in an epoxy resin by applying a DC electric field ", *Carbon*, **50**, 2453, (2012)

[35] D.V. van Krevelen, K. TE Nijenhuis, Properties of Polymers, *Elsevier* 2009.

[36] C.L. Beyler, M.M. Hirschler, "Thermal Decomposition of Polymers", in De Nenno PJ (Ed), "SEPE Handbook of Fire Protection Engineering", NFPA, Quincy, Ma, 3rd Ed, 2002, Chap.7.

[37] E. Detrait, J. B. Lhoest, B. Knoops, P. Bertrand, P. V. D. B. de Aguilar, "Orientation of cell adhesion and growth on patterned heterogeneous polystyrene surface.", *J. Neurosci. Meth.*, **84** , 193, (1998).

[38] J. H. Lee, H. W. Jung, I. K. Kang,H. B. Lee, "Cell behaviour on polymer surfaces with different functional groups", *Biomaterials*, **15,** 705, (1994)

[39] M. Buttiglione, F. Vitiello, E. Sardella, L. Petrone, M. Nardulli, P. Favia, R. d'Agostino, R. Gristina, "Behaviour of SH-SY5Y neuroblastoma cell line grown in different media and on different chemically modified substrates", *Biomaterials*, **28**, 2932, (2007)

[40] V. Marchesano, O. Gennari, L. Mecozzi, S. Grilli, P. Ferraro, "Effects of Lithium Niobate Polarization on Cell Adhesion and Morphology", *ACS Applied Materials &Interfaces* ,**7**, 18113, (2015)

Chapter 7

Conclusions

This thesis has focused on the Lithium Niobate (LN) ferroelectric crystal and on its wide variety of skills, as starting point for an alternative manipulation of soft matter guided by the pyroelectric effect, with particular attention to biodegradable and biocompatible polymeric materials. The efforts made to develop highly efficient pyro-EHD processes led to control the pyroelectric effect at microscale extending the outlook towards innovative techniques and forefront application fields.

Original approaches for the replacement of the classical thermal stimuli used to activate the pyroelectric effect, have been discussed. The result has been the introduction of original *top-down* polymers manipulation techniques, that are also compact-less and nozzle-less. The implementation of integrated micro-heaters in the ferroelectric crystal allowed to experience a 'controlled' electrospinning free from whipping instabilities due to a 'uniform' pyroelectric field. Furthermore, the use of nanocomposite polymer membranes together with the crystal, allows to produce a more efficient pyroelectric field in terms of radiation absorption and this technique was implied for alternative ink-jet printing and patterning as well as for energy harvesting, by means of a dedicated circuit.

In a further part of the work, in a kind of *bottom-up* like approach, alternative platforms for cells proliferation were tested, exploiting the versatility of the LN crystal. Biocompatibility studies onto different substrates were reported. The influence of the face polarity of the 'naked' crystal on cells adhesion, proliferation and behavior was analyzed demonstrating the finding of a new biocompatible platform. Moreover, biocompatible pyro-electrified polymer membranes were showed to be flexible and free-standing platforms useful to study cellular processes in vitro.

All the results presented in this thesis suggest new routes in soft matter manipulation, offering original strategies for high resolution printing and patterning, opening interesting perspectives for the realization of functionalized scaffolds able to guide cells fate and suggesting powerful platforms for clinical diagnostic and bio-sensing.

Appendix A

A.1 Basic principles of operation for pyro-ES

A standard electrospinning setup consists in a simple apparatus. The basic equipment requirements are a high voltage power supply, a syringe needle (electrode) connected to the voltage generator and a counter electrode collector (Figure A.1(a)) [1]. Even if we are working with an elementary structure, the physics of the process is extremely complex [2]. We have to take into account the material factors (molecular weight, viscosity, conductivity, permittivity, surface tension), the process factors (needle-to-collector distance, nozzle layout, applied voltage [3], flow rate, auxiliary electrodes, velocity of collector), but also the circumstance factors such as humidity and temperature air. The new configuration proposed, enables the elimination of some of the aforementioned parameters, but, to the best of our knowledge, the process follows a similar path.

Since the first electrospinning patent was issued in 1934 [4], the behavior of electrified jets were investigated deeply. Referring to the pioneering works of Reneker et al. [5,6] and Yarin et al. [7], there are two classes of models describing the process which differ in terms of interpretation of the 'jet nature'. One considers the polymer jet following the continuum mechanics equations, the other instead divides the thread in a discrete collection of charged particles (beads) obeying to Maxwell fluid mechanics and experiencing four types of interaction: Columbian repulsion, viscoelastic drug, curvature-driven surface tension and external electric field. Embracing the discrete theory, we consider a jet originating from a reservoir directly put on a tip, in an upward configuration (Figure A.1(d)). The driving pyroelectric force, due to the integrated microheater, allows the drop to deform due to the accumulation of charges, with the consequent formation of the Taylor cone on the surface of the polymer/liquid solution. The mechanism responsible of this deformation/polarization is well described in a recent work of Gennari et al. [8] depending on the starting ink. In particular, if we are working with a dielectric solution, we can say that the accumulation of the charges on the apex of the drop in a slow polarization process, is driven by the convection current (instead of the conductive one). Therefore, the convection charges accelerate the surrounding liquid towards the cone apex, causing the stretching of the meniscus along the interface.

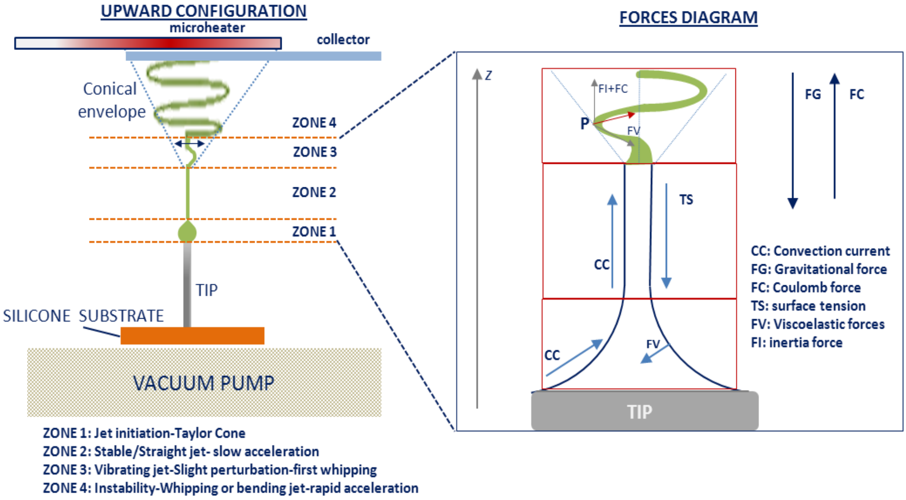

Figure A.1: Schematic diagram of the different regions of jet's development in the 'upward' configuration and representation of the forces involved during the process

As highlighted in Figure A.1, when the electric potential exceeds a critical limit, the jetting from the tip starts and its evolution can be thought as passing through four different regions. The first, as described above, is the one related to the formation of the Taylor cone whose geometry depends on how surface tension and electrostatic repulsion 'play'. The second region of jet elongation is governed by Coulomb forces and characterized by a straight segment, the so called steady jet [6]. In this regime we have pure extensional deformations that generate elastic stresses which can suppress Rayleigh instability [9]. Due to the presence of the solvent (not completely evaporated before the jet reaches the collector), electrostatic forces accelerate the polymer against gravity and surface tension [10] and the diameter of the fiber decreases monotonically with distance from the tip [6]. The third region instead, represents the beginning of jet instabilities after the initiation from the cone. As shown in Reneker et al. [5], begins a self-similar, fractal-like process of development of these bending instabilities driven by the electric field. After a slight perturbation (zone 3) the competition between the free charges in the polarized jet and the external electric field generates different kinds of instability that we can divide in axysimmetric and non-axysimmetric. The first one, also known as Rayleigh instability, happens with dilute polymer solutions with no elasticity. In this case, on the z axis direction, the jet breaks up into droplets or, sometimes, a beads-on-string structure takes place (i.e. for long chains molecules). In the upward configuration we propose, instead, the gravitational force and the electrostatic one are antagonists during the travel of the jet to the collector, leading to the disappearance of this instability, according to Yu and Rutledge [9]. The non-axysimmetric instability or whipping instability is instead responsible of the ‘chaotic’ behavior of the jet. In this situation a series of small oscillations grows in diameter as the fiber approaches the collector (zone 4). In terms of forces, the off-axis is due to the repulsion of consecutive segments of the straight jet (discrete model), causing the jet to whip [11], thus giving rise to a ‘pendulum-like’ motion. As shown in Figure 1 (right panel), the path, limited to the conical envelope, arises from the co-existence of the inertia force, the torque exerted by electrostatic force and the internal elastic and viscous forces that, interacting, incentive bending deformations and buckling instabilities. It can be also demonstrated that the helicoidal path is the most energetically favorable to follow for the charged jet [12]. The bending instability shouldn’t take place in a near-field configuration [11], but, referring to our device, the jet whips and rotates around the center of deposition and the presence of the x-y translation stage in the pyro-ES setup, puts the fiber in a tension state thus helping the controllability of the deposition.

References

[1] D.H Reneker, I. Chun, “Nanometre diameter fibres of polymer, produced by electrospinning”, *Nanotechnology*, **7,** (1996), DOI:10.1088/0957-4484/7/3/009

[2] D.Li, Y.Xia, “Electrospinning of nanofibers:reinventing the wheel?”, *Adv.Mater.*,**16**,(2004)

[3] G. Chang, X. Zhu, R. Warren, “Electrospinning of microspiral fibers”, (2014)

[4] Formahls, *U.S.Patent* No1.975.504(filed 1934)

[5] D.H. Reneker, A.L. Yarin, “Bending instability of electrically charged liquid jets of polymer solutions in electrospinning”, *Journal of Applied Physics*, **87**,(2000)

[6] D.H. Reneker, A.L.Yarin, “Electrospinning jets and polymer nanofibers”, *Polymer* , **49**, 2387-2425, (2008)

[7] A.L.Yarin, S.Koombhongse, D.H.Reneker, “Taylor cone and jetting from liquid droplets in electrospinning of nanofibers”, *Journal of applied physics*, **90**,4836 (2001)

[8] O. Gennari, L. Battista, B. Silva, S. Grilli, L. Miccio, V. Vespini, S. Coppola, P. Orlando, L. Aprin, P. Slangen, P. Ferraro, “Investigation on cone jetting regimes of liquid droplets subjected to pyroelectric fields induced by laser blasts”, *Appl. Phys. Lett.*,**106**, 054103 (2015)

[9] J.H. Yu, S.V. Fridrikh, G.C. Rutledge, “The role of elasticity in the formation of electrospun fibers”, *Polymer*, **47**, 4789-4797, (2006)

[10] F. Abdel-Hady, A. Alzahrany, M. Hamed, “Experimental validation of Upward Electrospinning process”, *ISRN nanotechnology*, ID851317, 2011

[11] G. Zheng, Z. Yu, M. Zhuang, W. Wei, Y. Zhao, J. Zheng, D. Sun,”EHD direct writing of three dimensional multi-loop nanofibrous coils”, *Appl.Phys.A,***116**, 171-177, (2014)

[12] A.G. Marin, G. Riboux, I.G. Loscertales, A. Barrero, “Whipping instabilities in electrified liquid jets”, (2008)